博士論文

Evolution Mechanisms of Non-metallic Inclusions in Fe-Al-Ti-N Alloy

(Fe-Al-Ti-N 合金中非金属介在物の生成機構)

崔 元晋

Contents

Chapter 1. Introduction

1.1 Introduction

Generally, steelmaking process is classified into three steps, mainly pretreatment process, basic oxygen furnace process (BOF) and secondary refining process. Pig iron composed of iron and carbon, which is provided by ironmaking process, has been used as a main raw material for steelmaking process. Pig iron contains various impurities such as Mn, Si, S and P. At the BOF process, such kinds of all impurities are simultaneously removed through reaction with oxygen (oxygen blowing). On the contrary, oxygen content in the melt is increased. Therefore, deoxidation process is required after the BOF process to remove oxygen.

Titanium-alloyed steels have been widely used for various products such as automobile sheets, or heavy plates for ship construction in order to improve steel properties.

Since titanium also has a strong affinity with oxygen, it is normally added for alloying after deoxidation process. Aluminum is one of the common, strong and less expensive deoxidizer. Comparing to the cost of aluminum, titanium is relatively expensive and thus the combined process of deoxidation by aluminum and alloying by titanium is popular. Therefore, Al-Ti deoxidation process is one of the common processes for secondary refining in steelmaking process.

The added Al and Ti form various types of non-metallic inclusions which are usually perceived as negative impurity for steel, since non-metallic inclusions cause submerged entry nozzle (SEN) clogging, surface defect and so on.

On the other hand, the positive effects of titanium-based inclusion have reported by several researchers such as prevention of austenite grain growth by pinning effect and assistance of finer ferrite microstructure formation. These effects are extremely useful for the control of fine microstructure during solidification or heat treatment, consequently which leads to the improved mechanical properties of steel. Therefore, in order to utilize the inclusion, the study of the clarification of the effect of the inclusions during solidification and in solid state of steel is quite

important.

In current research, formation and change behaviors of inclusions in solid state of Fe-Al-Ti-O-N alloy system which is very fundamental system for Ti bearing Al-killed steel have been investigated. In addition, positive effect of non-metallic inclusions which formed by Al-Ti complex deoxidation on the microstructure has been estimated.

1.2 Literature review

1.2.1 Formation of inclusions by Al-Ti complex deoxidation in the liquid steel

Titanium bearing steels have been widely used for various products such as automobile sheets, or heavy plates for ship construction, since titanium has a great advantage not only in its cost effectiveness but also in improvements of steel properties, e.g. formability, non-ageing property, prevention of austenite grain growth, and promotion of finer ferrite microstructure formation.

The added Ti forms the several types of non-metallic inclusions in the steels such as oxide, nitride, sulfide, carbide and so on. Furthermore, titanium forms the several types of oxide phase in the liquid melt such as Ti_3O_5, Ti_2O_3 and TiO, depending on the steel compositions as shown in **Fig. 1-1**.[1)]

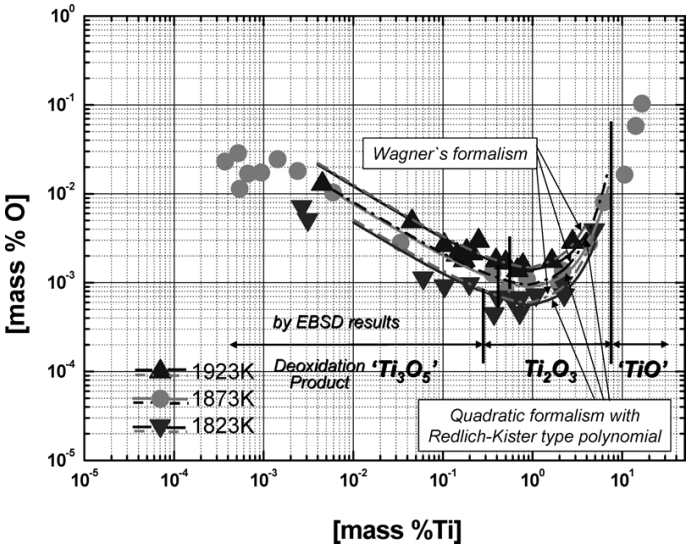

Figure 1-1. Equilibrium relation between [%Ti] and [%O] in liquid Fe at 1823, 1873 and 1923 K.[1)]

In the producing process of Ti bearing steels, generally Al is added before Ti addition to prevent the loss of Ti which has strong reactivity with oxygen. Therefore, Al-Ti complex deoxidation is one of general process for the producing of Ti bearing steels.

1.2.1.1 Equilibrium oxides

Various equilibrium oxides are formed by Al-Ti complex deoxidation. Many investigators have studied the equilibrium oxide phase diagram in the liquid melt. Ruby-Meyer *et al.*[2] have estimated the equilibrium phase diagram for the system Fe-Al-Ti-O at 1793 K by employing the CEQCSI multiphase equilibrium software based on the IRSID slag model. The calculated stable phase diagram indicates the formation of Al_2O_3, Ti_2O_3, Al_2O_3-TiO_2 and TiO_x-Al_2O_3 liquid oxide. On the contrary, Jung *et al.*[3] have employed FACT databases and FactSage software, and calculated the phase diagram of oxides for the Fe-Al-Ti-O system at 1873 K. They reported the existence of Ti_3O_5 solid phase which did not exist in the diagram reported by Ruby-Meyer *et al.*[2]. Kim *et al.*[4] have also reported the phase stability diagram of oxides equilibrating with Fe-Al-Ti-O melt at 1873 K. The stable regions for Al_2O_3, Ti_2O_3 and Ti_3O_5 were shown, while those for other oxides and liquid oxides were not observed. All the previously mentioned equilibrium phase diagrams for the Fe-Al-Ti-O system are shown in **Fig. 1-2**. Although there are some differences between diagrams, especially in low concentrations of Al and Ti, since these diagrams are calculated by using different thermodynamic data, various kinds of equilibrium oxides form depending on the metal composition.

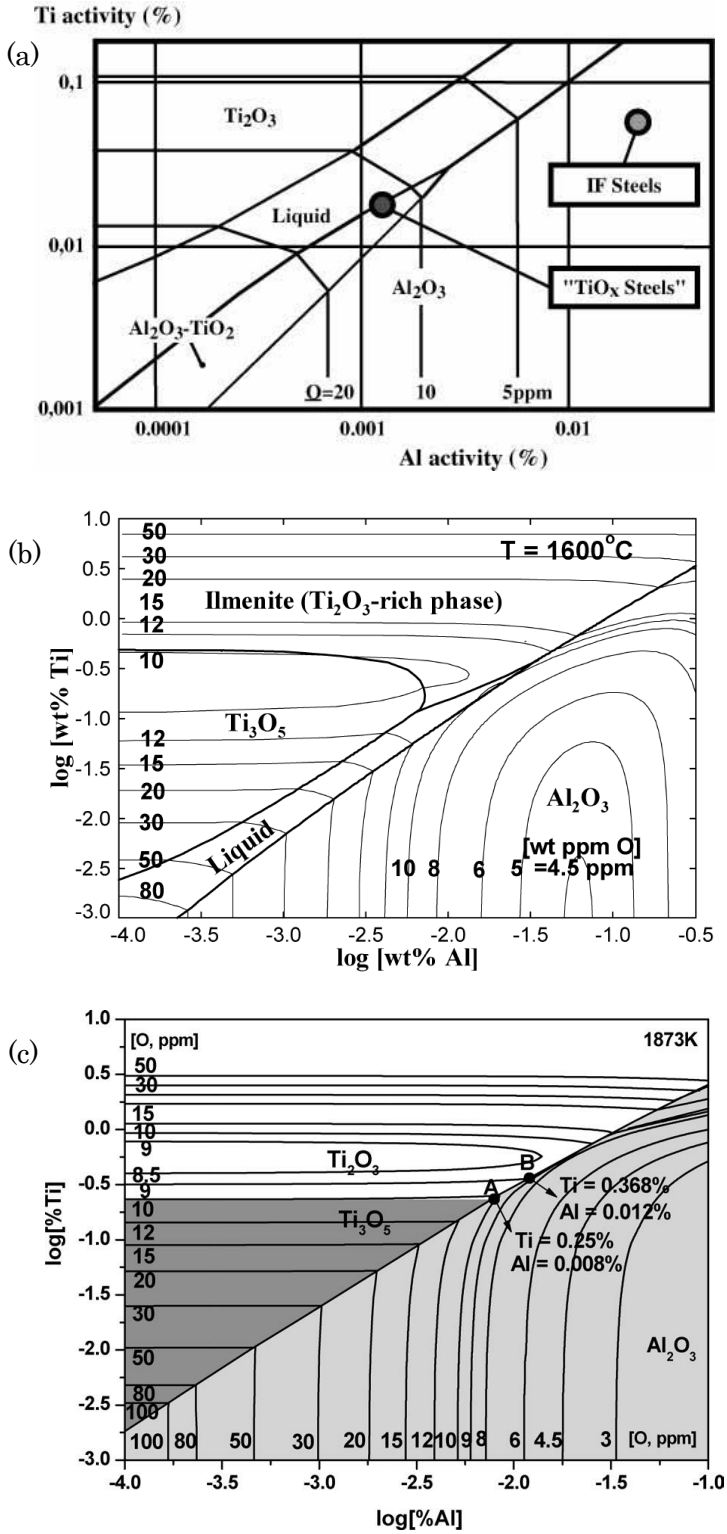

Figure 1-2. Equilibrium diagram for the system Fe-Ti-Al-O at (a) 1793 K[2], (b) 1873 K[3] and (c) 1873 K[4].

1.2.1.2 Transient inclusions

Size, morphology and chemistry of non-metallic inclusion in the liquid melt are affected by various parameters such as Ti/Al ratio, deoxidation time in a liquid state, addition sequence of deoxidants and reaction with slag.

Wang *et al.* [5), 6), 7)] have reported the sequential transition of inclusion characteristics with deoxidation time at various Ti/Al ratios by using sampling method. After Ti addition in the Al killed Fe-Al-O alloy, Al_2TiO_5, TiO and even Ti_2O could be instantaneously produced depending on Ti/Al ratio as shown in **Fig. 1-3**. However, **Fig. 1-3** is just expectation path and not calculation results.

In addition, morphological change of inclusions during Al-Ti complex deoxidation could be also affected by the Ti/Al ratio as shown in **Table 1-1.**

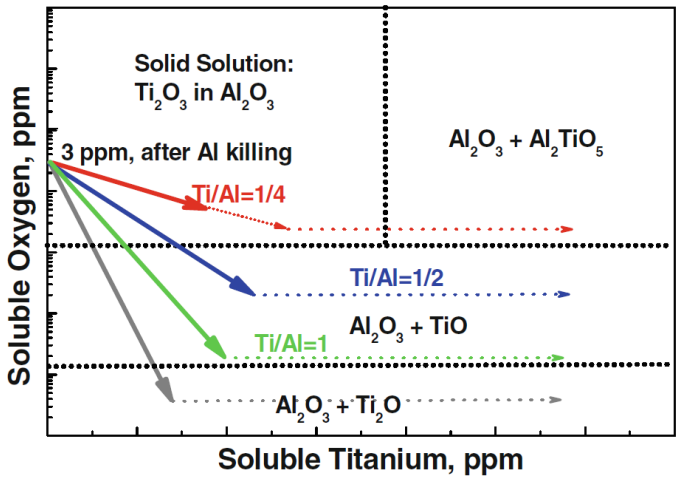

Figure 1-3. Schematic illustration of possible formation paths with respect to soluble oxygen and titanium contents.[7)]

Table 1-1. Connection of transient stage products with morphological change.[7)]

Ti/Al	Transient Stage Products	Morphological Change
0	Al_2O_3	No
1/4	Al_2O_3, TiO, solid solution of Ti_2O_3 into Al_2O_3	No
1/2	Al_2O_3, Al_2TiO_5	Yes
1 (Single and multiple additions)	Al_2O_3, Al_2TiO_5	Yes

Matsuura *et al.* [8] have investigated the evolution of oxide inclusions with several Al and Ti deoxidation patterns and various metal compositions by sampling technique at 1873 K. They reported that chemical compositions of transient inclusions were different with the Al and Ti deoxidation patterns such as simultaneously or separately, due to the dissimilar reaction paths as shown in **Fig. 1-4**. Also, evolution steps of size and morphology of inclusions were not similar in various Ti/Al ratios. However, finally inclusions in almost all cases approached the equilibrium state oxide which is Al_2O_3 as shown in **Fig. 1-4**.

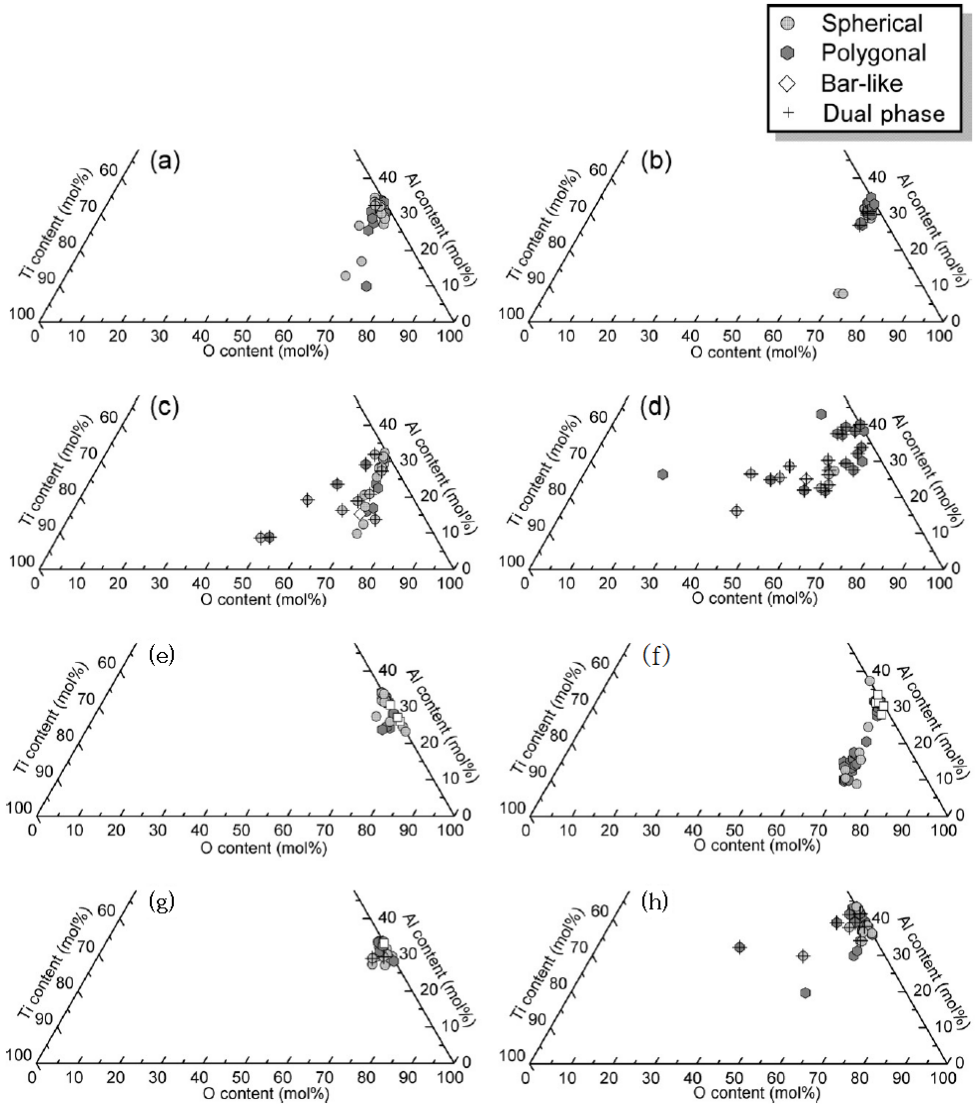

Figure 1-4. Chemical composition of inclusions for (a) 1 min, (b) 2 min, (c) 3 min (d) 4 min after separately additions and (e) 1 min, (f) 2 min, (g) 3 min, (h) 4 min after simultaneously additions.[8]

Sun *et al.* [9] have also investigated the morphology and chemistry change of oxide inclusions with several Al and Ti deoxidation patterns and various Ti/Al ratios at 1873 K. **Figure 1-5** shows the proposed evolution mechanism of hollow oxide inclusions in the case of the Ti-Al deoxidation which is the Al addition after Ti addition. This type inclusion also evolved to reach the equilibrium state oxide (Al_2O_3) with time.

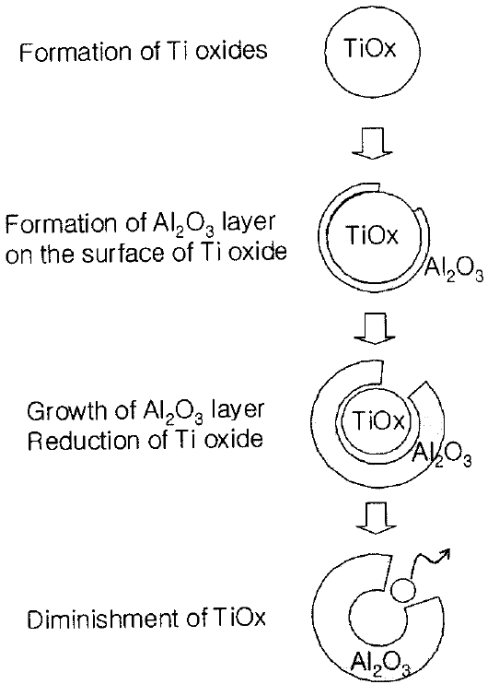

Figure 1-5. Proposed mechanism for the formation of hollow oxide inclusions after Ti/Al deoxidation.[9]

Park *et al.* [10] have reported the reoxidation of liquid steel containing Al and Ti by slag. Two-layer complex oxides which are Al-Ti-O phase with an Al_2O_3 core inside were formed by the oxygen provided from slag during reoxidation as shown in **Fig. 1-6**. They explained the formation of complex oxide inclusions as follows; Al_2O_3 forms first due to the disparity in the extent of supersaturation of Al and Ti and then Al_2O_3 grows until driving forces for Al and Ti deoxidation become the same by decreasing Al content in the vicinity of oxide. And then, Al-Ti-O phase forms on the Al_2O_3.

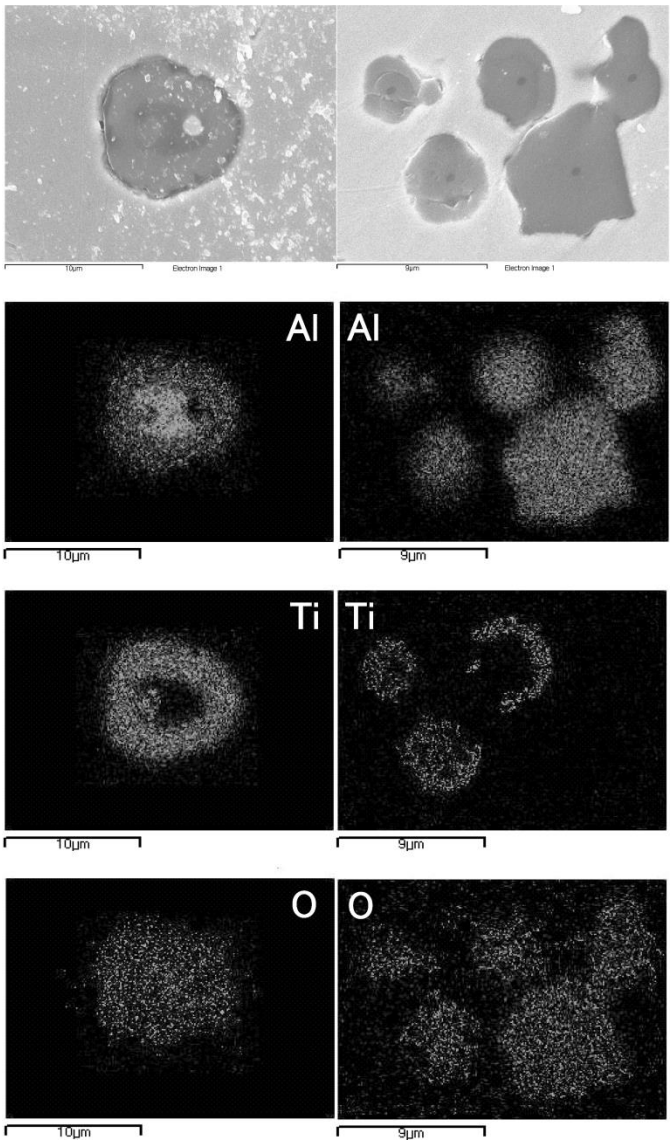

Figure 1-6. SEM images of typical complex oxide inclusions observed in the bulk metal.[10)]

Doo *et al.* [11)] have investigated the morphology change of complex oxide inclusion by Al-Ti complex deoxidation in the RH process. **Figure 1-7** shows the detected complex oxide. They suggested that the formation of Al-Ti-O complex oxides occurs because of the locally high titanium content in the vicinity of the added Ti sponge before dissolving in the melt. However, Sun *et al.*[9)] pointed out that the complex oxide would be formed by oxygen dissolved from RH top slag by reoxidation, since samples were collected from the liquid steel close to top slag.

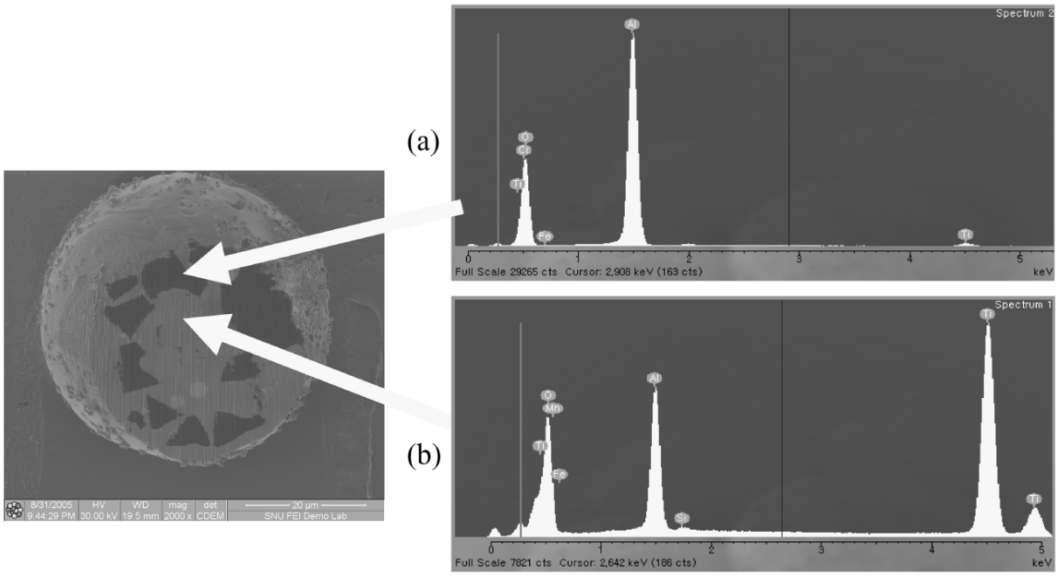

Figure 1-7. Quantitative composition analysis: (a) Alumina region and (b) Ti-Al complex oxide region.[11)]

Van Ende *et al.*[12)] have investigated the evolution of oxide inclusions by various Al-Ti deoxdation patterns at around 1873 to 1923 K. They expounded the evolution path of oxide inclusion by using the phase diagram of oxides for the Fe-Al-Ti-O system at 1893 K as shown in **Fig. 1-8**. As shown in **Fig. 1-8**, after Ti addition, metal composition entered the $Al_2O_3 \cdot TiO_2$ stable region (point D), hence Al-Ti-O complex oxides besides large Al_2O_3 cluster oxides observed in the samples. And then, metal composition moved to Al_2O_3 stable region (point E) by second Al addition. After 3 min, Al_2O_3 just observed due to the reduction of Ti oxide by Al.

From the previous all researches, various types of morphologies, sizes and chemistries of the transient oxide inclusions can be obtained by controlling several conditions of Al-Ti complex deoxidation.

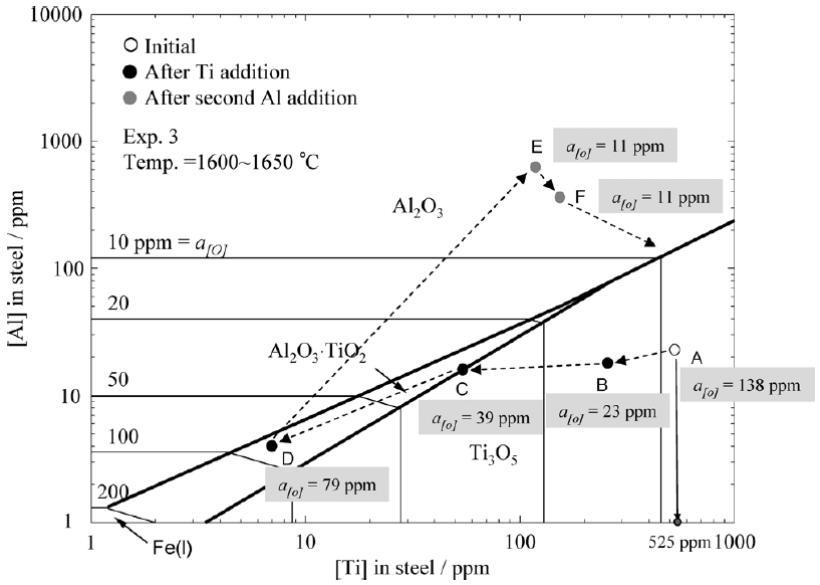

Figure 1-8. Evolution of [Ti] and [Al] plotted on the computed equilibrium diagram of the Fe-Al-Ti-O system at 1620℃. $a_{[O]}$ is given next to each point.[12)]

1.2.2 Formation of inclusions in the solid state steel

Not only various oxide inclusions during deoxidation but also non-metallic inclusions (nitride, sulfide, oxide and carbide and so on) during solidification and heat-treatment can be formed. By decreasing temperature, solubility of each element in the steel decreased and then variety of inclusions can be precipitated. Especially, formation of titanium nitride has substantially reported for Ti bearing steels.

The solubility product of TIN in the liquid, δ, γ and α phases of iron can be described and expressed as shown in **Fig. 1-9** and **Eqs. (1-1), (1-2)** and **(1-3)**.[13)] It had measured by using a diffusion couple technique.

$$\log[\text{mass\%Ti}]\,[\text{mass\%N}]_{\alpha(\delta)} = 4.65 - \frac{16310}{T} \quad \text{13)} \tag{1-1}$$

$$\log[\text{mass\%Ti}]\,[\text{mass\%N}]_{\gamma} = 4.35 - \frac{14890}{T} \quad \text{13)} \tag{1-2}$$

$$\log[\text{mass\%Ti}][\text{mass\%N}]_{liq} = 4.46 - \frac{13500}{T} \quad \text{13)} \tag{1-3}$$

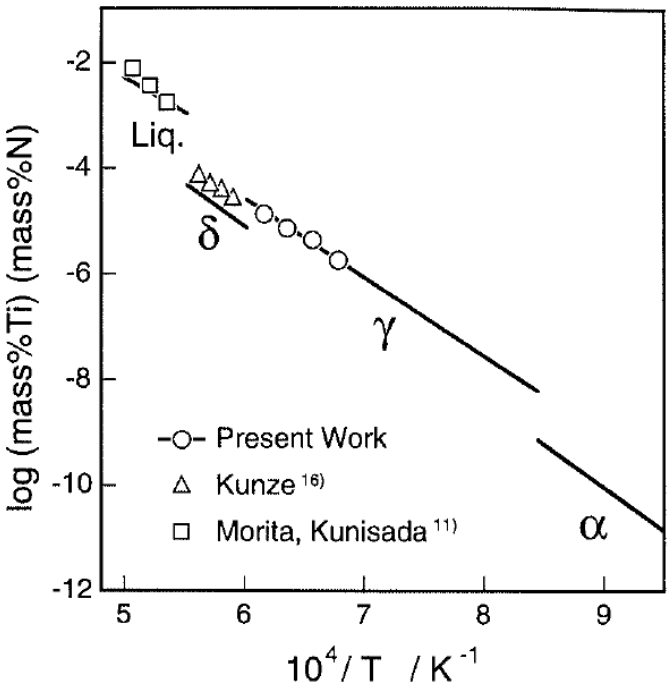

Figure 1-9. Solubility products of TiN.[13)]

As shown in **Fig. 1-9**, solubility product of Ti and N in the liquid and solid state iron was decreased with decreasing temperature. According to these results, TiN can be precipitated by decreasing temperature in all states of iron.

In Al-Ti complex deoxidation, TiN phase on the Al-Ti-O oxide have been observed.[8)] As explains by them, the observed TiN phase was precipitated on the oxide inclusion during solidification and cooling. It can be elucidated as follows. Ti content in each sample is high enough to make the high value of solubility product of Ti and N, even though alloys have a low content of nitrogen from 9 to 14 ppm.

Not only titanium nitride but also other types of inclusions can be formed during solidification with metal compositions. Park *et al.* have performed the evolution of oxide and nitride in the ferritic stainless steel during solidification by using thermochemical computation program as shown in **Fig. 1-10**.[14)] As shown in **Fig. 1-10 (a)**, titanium nitride started to form in the mushy zone during solidification. From 1 673 K, solid spinel oxide ($MgAl_2O_3$) can be formed. Further, the mass fraction

of constituents in the liquid MgO-Al_2O_3-TiO_x oxide, existed until 1 523 K, were changed as shown in **Fig. 1-10 (b)**.

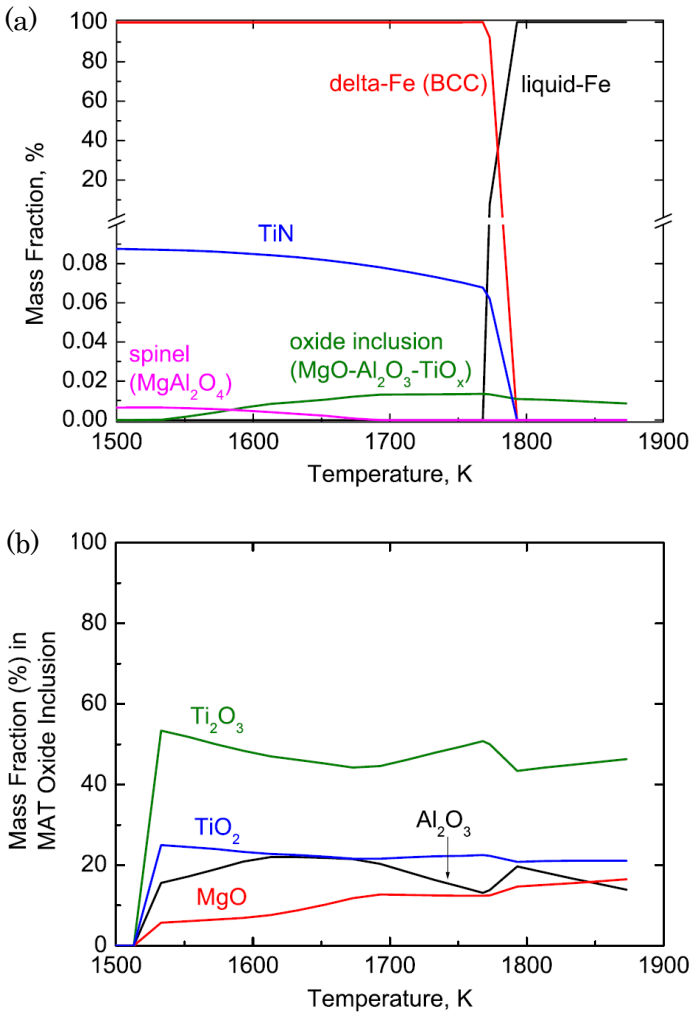

Figure 1-10. Mass fractions of metal, oxide and nitride phases with regard to temperature.[14)]

Park *et al.*[15)] have also computed the evolution of inclusions in several chemical compositions of (Mn-Si-Ti)-deoxidized steels during solidification. Various types of inclusions such as TiN, MnS, Mg-Ti-Al-O spinel and ilmenite have an opportunity to precipitate at several temperatures with regard to Al contents as shown in **Fig. 1-11**. MnS appears in first step of solidification. However, from around 1 623 K, TiN has been given a preference to formation in all of (Mn-Si-Ti)-deoxidized steels.

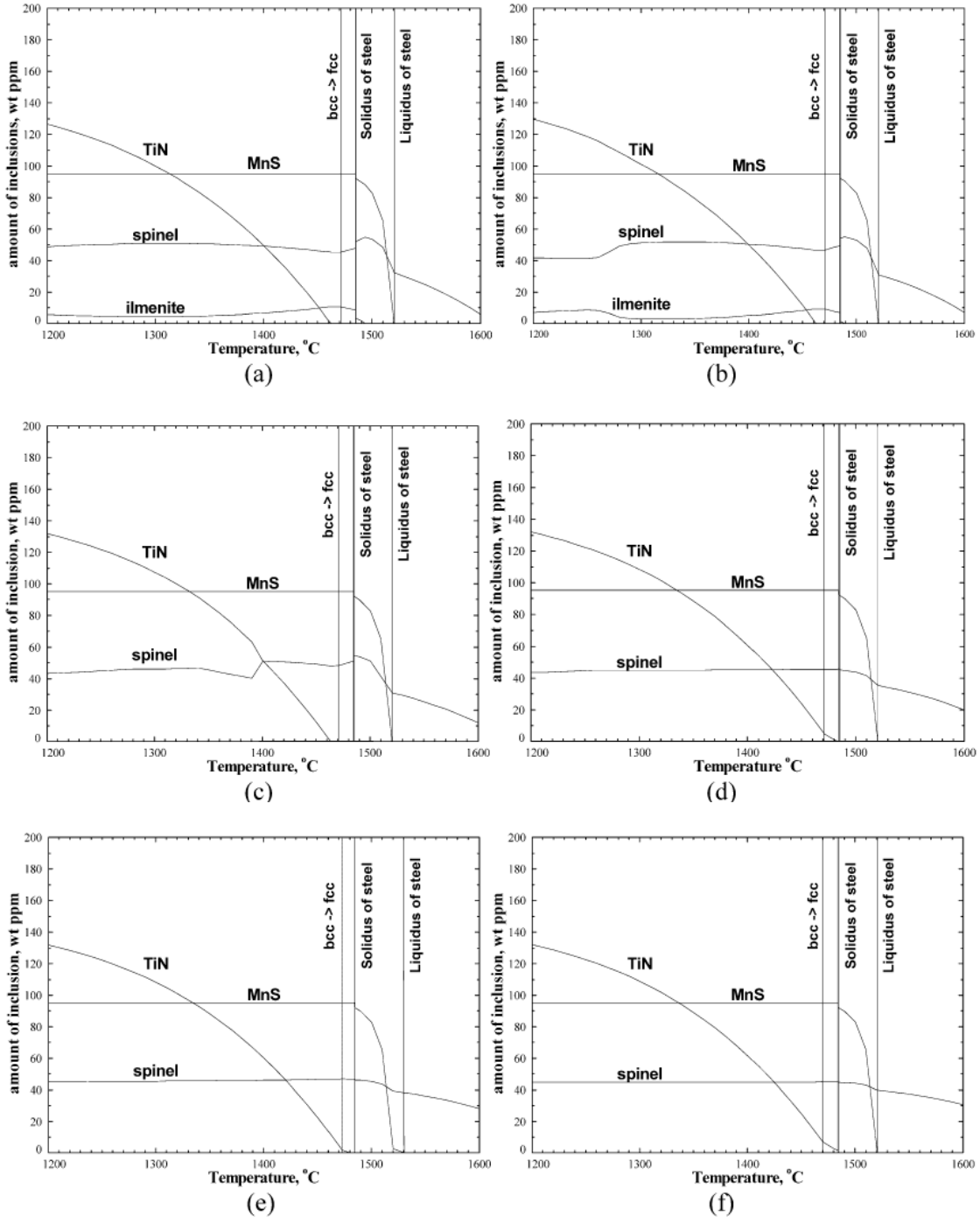

Figure 1-11. Evolution of inclusions during solidification with Al content of (a) 6 ppm, (b) 12 ppm, (c) 21 ppm, (d) 40 ppm, (e) 87 ppm and (f) 147 ppm.[15)]

1.2.3 Utilization of inclusions (Oxide metallurgy)

The basic concept of "Oxide metallurgy" can be described as shown in **Fig. 1-12**.[16] There are two objects of oxide metallurgy for utilizing of inclusions. One is control of melting point of inclusions for improving their deformability. The other is control of nucleation sites for precipitates, since, during solidification and heat treatment, inclusions usually precipitated not only at grain boundary and site of high dislocation density but also on pre-existing inclusions became nucleation sites. Therefore, control of the precipitated inclusions and pre-existing inclusions which formed during deoxidation both are key techniques to bring out advantage of inclusions for grain refining, e.g., prevention of austenite grain growth by pinning effect and assistance of grain refinement by the formation of intra-granular ferrite in the γ austenite grain. Several investigators have studied the effect of inclusions which formed during deoxidation on the precipitation and precipitates which formed during solidification and heat treatment on the microstructure.

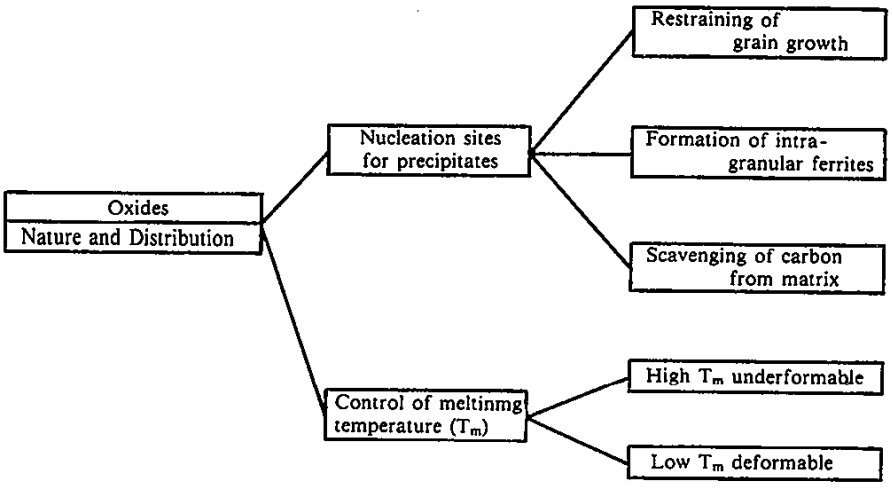

Figure 1-12. Basic concept of oxide metallurgy for steel.[16]

Morikage *et al.*[17] have proposed the ferrite nucleation model on the several positions of a rectangular TiN for grain refining. And, energy variation for various nucleation site models on the TiN at constant driving force of transformation expressed as shown in **Fig. 1-13**. The ferrite nucleation on facet has the smallest energy variation. Consequently, ferrite can be more easily formed on the facet of TiN.

Furthermore, the critical TiN size for ferrite formation by the observation of the maximum size of TiN particle in the non-transformation austenite grain and by the calculation results by using **Eq. (1-4)** have described as shown in **Fig. 1-14**.

$$l_{crit} = -4 \cdot \sigma_{\alpha\gamma} / \Delta G_V \quad [17] \tag{1-4}$$

where, l_{crit} is the critical size of TiN, $\sigma_{\alpha\gamma}$ is the interfacial energy between austenite and ferrite and ΔG_V is driving force of transformation. Experimentally, the ferrite formation has not been induced with the TiN size less than 80 nm in the case of conditions Aa and Ba. (Aa: $\Delta G_V = -61 \times 10^6$, Ba: $\Delta G_V = -65 \times 10^6\ \mathrm{J/m^3}$) According to the **Fig. 1-14**, the calculation results agreed relatively well with the experimental results. From these results, necessary critical size of TiN particle for ferrite formation on the TiN phase during heat treatment process can be predicted by applying the **Eq. (1-4)** in low carbon steel.

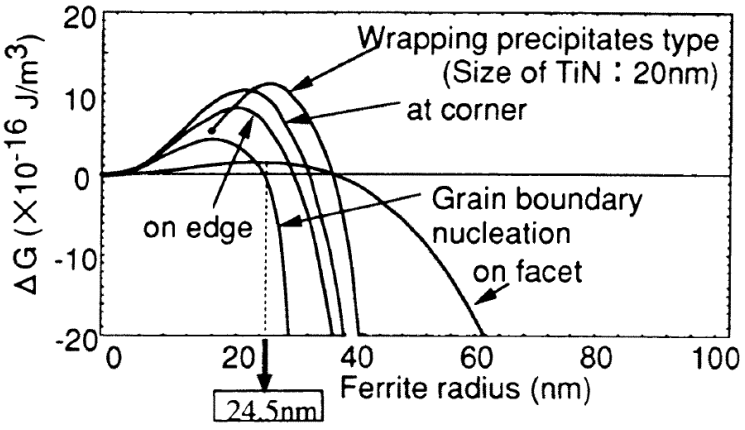

Figure 1-13. Energy variation with ferrite radius for various nucleation site models on rectangular TiN precipitates. ($\Delta G_V = -50 \times 10^6 \mathrm{J/m^3}$) [17]

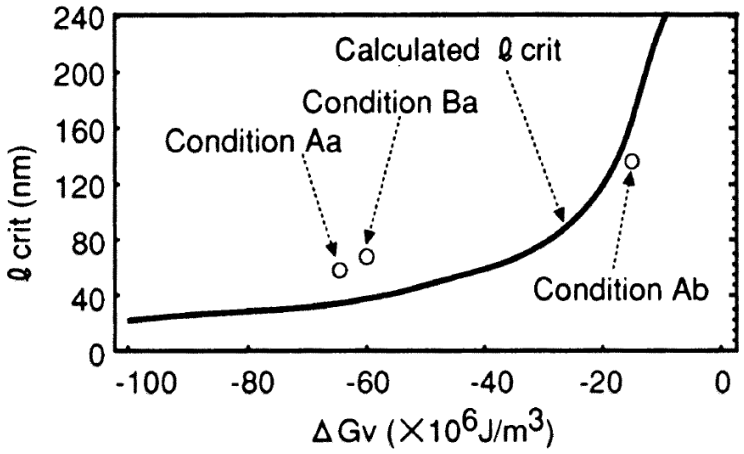

Figure 1-14. Comparison of the calculated l_{crit} with experimentally measured l_{crit}.[17)]

Matsuda *et al.*[18)] have also reported the effect of TiN particles on the austenite grain size in the low carbon low alloy steels. The relationship between austenite grain size and distribution of TiN particles can be described as shown in **Fig. 1-15** and **Eq. (1-5)**.

$$R = K \cdot (r/f) \quad [18)] \tag{1-5}$$

where, R is the radius of the austenite grain, r is the mean particle size of TiN, f is the volume fraction of TiN particles and K is the numerical factor which depends on the kind of precipitate particle, and is approximately 1.5 for TiN particles. As shown in **Fig. 1-15**, austenite grain size can be minimized by decreasing the mean distance between TiN particles which coalesced by Ostwald ripening phenomena during heat treatment, i.e., the control of TiN dispersion is quite important for minimizing of austenite grain size.

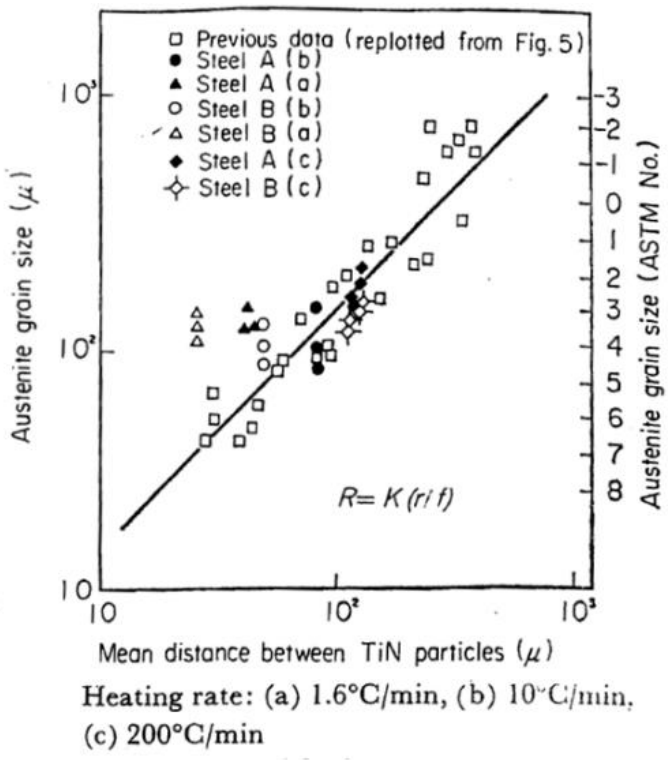

Figure 1-15. Relation between mean distance of TiN particles and austenite grain size.[18)]

Ohta *et al.*[19)] have estimated the effect of TiN bearing inclusions on the austenite grain size with or without Mg deoxidation. They understood the influence of TiN bearing inclusions on the γ grain size as regards Zener pinning force, Z_P, as shown in **Figs. 1-16, 1-17** and **Eq. (1-6)**.

$$Z_P = 3\sigma V f_V / d \quad [19)] \tag{1-6}$$

where, σ is the grain boundary energy, V is the molar volume of Fe, f_V is the volume fraction of particles and d is the mean particle diameter. **Figures 1-16** and **1-17** show the relationship between Zener pinning force and austenite grain size at 0.05% C and 0.15% C, respectively. In the case of 0.05% C alloy, the mean austenite grain size, $\overline{D}_A$, decreased as increasing of Z_P. However, $\overline{D}_A$ was constant at 0.15% C alloy. The different trends explained by uniformity of dispersion of TiN-based inclusions. The 0.05% C alloy which has the uniformly distributed TiN-based inclusions can reduce the size of γ grain by controlling Zener pinning force, e.g., several parameters (f_V and d).

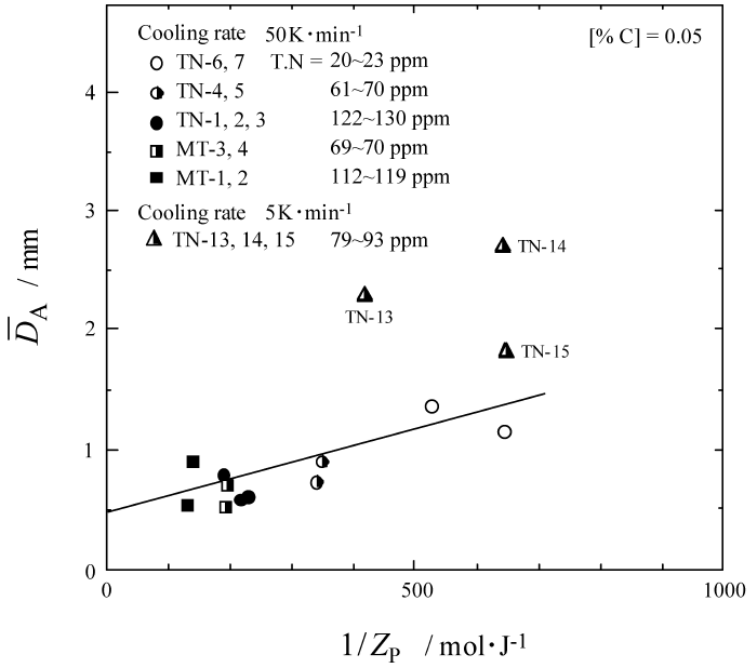

Figure 1-16. Effect of Zener pinning force on γ grain size at 0.05% C as functions of total nitrogen content and cooling rate.[19)]

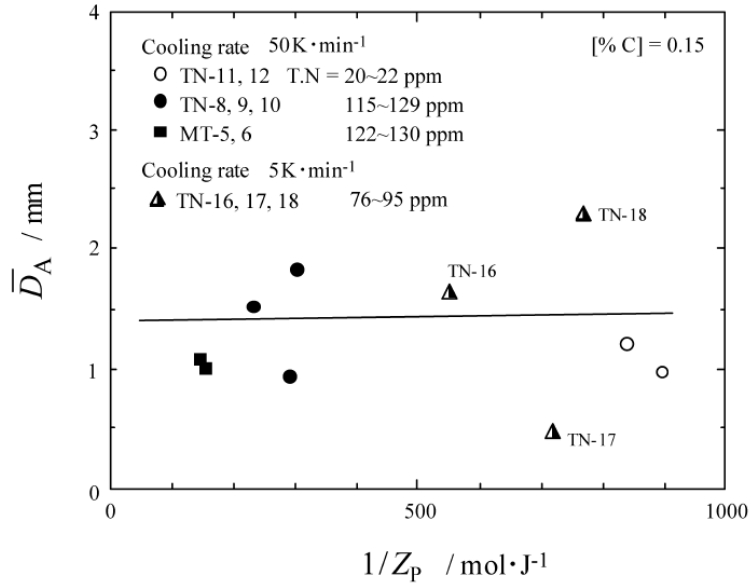

Figure 1-17. Effect of Zener pinning force on γ grain size at 0.15% C as functions of total nitrogen content and cooling rate.[19)]

Takano *et al.*[20] have reported the effect of oxide inclusion size on the microstructure by Al-Ca and Si-Mn complex deoxidations in the austenite stainless steel. **Figure 1-18** shows the effect of various inclusions which formed with different deoxidation conditions on the grain growth. As shown in **Fig. 1-18 (c)**, $MnO \cdot Cr_2O_3$ oxide particle with a radius of about 0.2 μm can affect the grain refining by pinning effect. On the contrary, oxide size more than 1 μm cannot be prevented grain growth.

In addition, they estimated the effect of oxide particle size on the grain size by using not only Zener theory (**Eq. (1-7)**) but also modification theory by Doherty [21] (**Eq. (1-8)**) as shown in **Fig. 1-19**.

$$D = 4d/3f \quad [20] \tag{1-7}$$

$$D = 2d/(\beta \emptyset f)^{0.5} \quad [21] \tag{1-8}$$

where D: grain size, d: dispersoid size, f: volume fraction of dispersoid, β: $\bar{R}_C/\bar{R}$, $\bar{R}_C$: the mean radius of curvature, $\bar{R}$: mean grain radius and $\emptyset$: actual fraction of particles on boundary. The calculated result by using **Eq. (1-8)** more agreed well with experimental results. From these results, grain size and whether the existence of pinning effect can be supposed by measuring volume fraction of oxide particles which formed by Al-Ca and Si-Mn complex deoxidation before thermo-mechanical treatment.

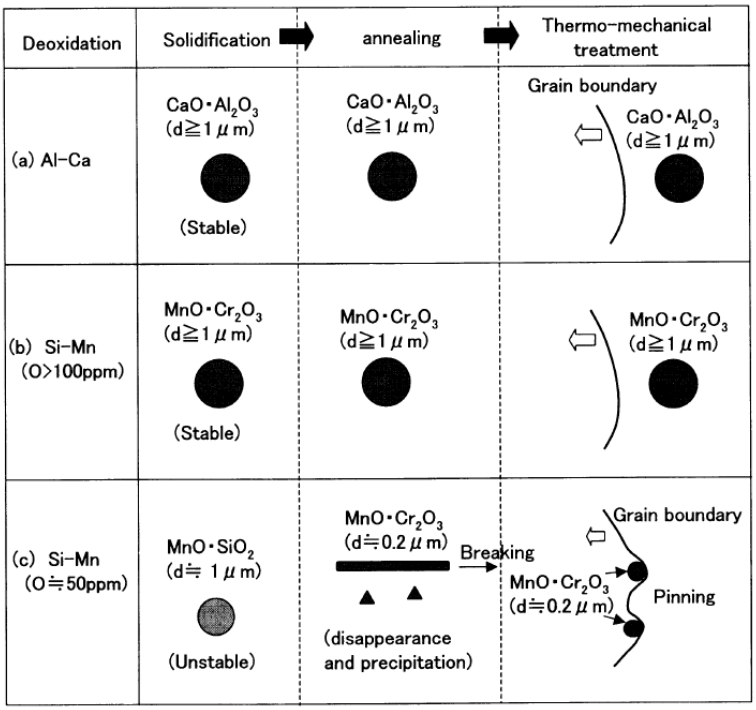

Figure 1-18. Schematic illustration showing the change in size and composition of oxides during thermo-mechanical treatment in (a) Al-Ca ,(b) Si-Mn (O ≥100ppm) ,(c) Si-Mn (O ≈50ppm) deoxidized austenite stainless steels.[20)]

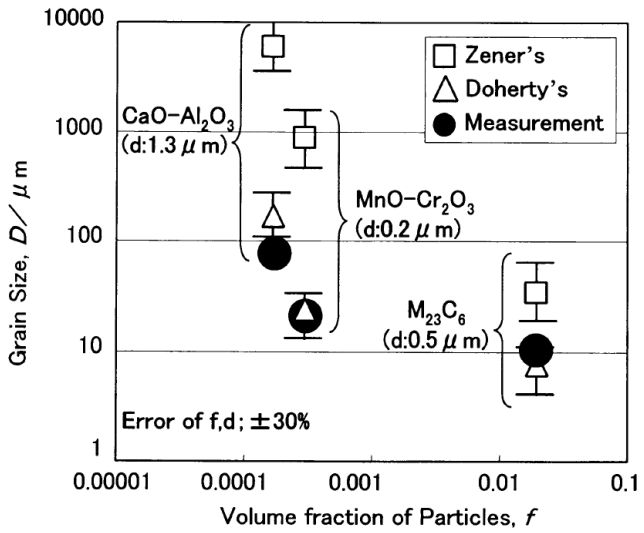

Figure 1-19. Relation between the volume fraction of particles and the theoretical and measured austenite grain sizes.[20)]

Kikuchi *et al.*[22] have also reported the relationship between inclusion size and grain size as shown in **Fig. 1-20**. They used the **Eq. (1-9)** which suggested by Nishizawa[23] for the calculating the relationship between grain size and inclusion size.

$$R = (2/9)d/f_0 \quad [22] \tag{1-9}$$

where, R: radius of a grain, d: diameter of particles and f_0: volume fraction of oxide. According to calculating results, TiO_2+TiN inclusion can be obtained the smallest grain at the same size of inclusions. The discrepancy between calculation results and experiment results had explained that the small inclusions below 0.1 μm which have a pinning effect had not detected in the experimental samples by SEM analysis.

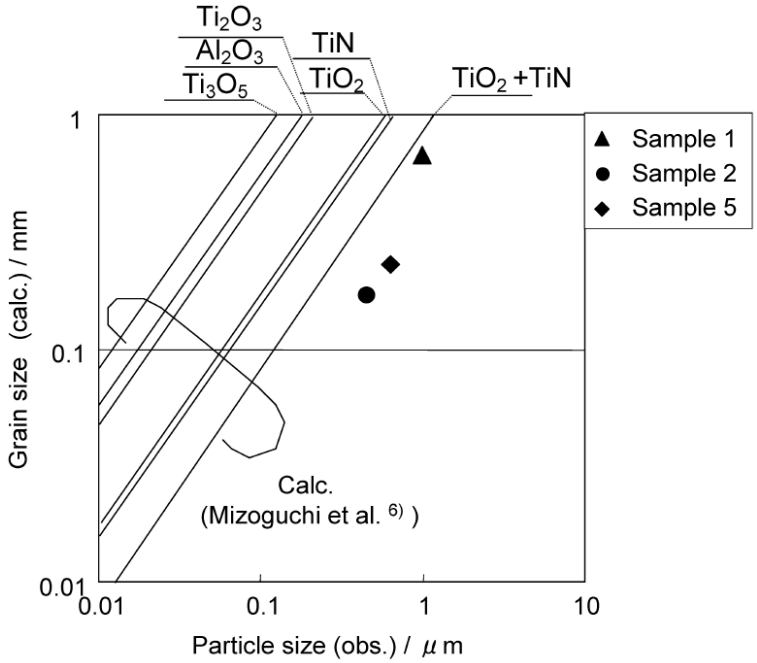

Figure 1-20. Relation between particle size and grain size.[22]

Oxide composition before solidification should be considered one of the key parameters to obtain fine structure. Fujimura *et al.*[24] studied the effect of oxide composition on formation of equiaxed fine-grain structure during solidification in the ferrite stainless steel. They found the Mg-Al-O based inclusion covered with TiN before solidification. Mg-Al-O based inclusions which have Mg/Al mass ratio range of 0.3 to 0.5 become the nucleation sites for formation of the equiaxed fine-grain

structure as shown in **Fig. 1-21**. **Figure 1-22** shows the mechanism of formation of equiaxed structure. Furthermore, they discussed that formation of TiN on the spinel inclusion which caused by planar disregistry between TiN and other oxides affected the formation of fine microstructure.

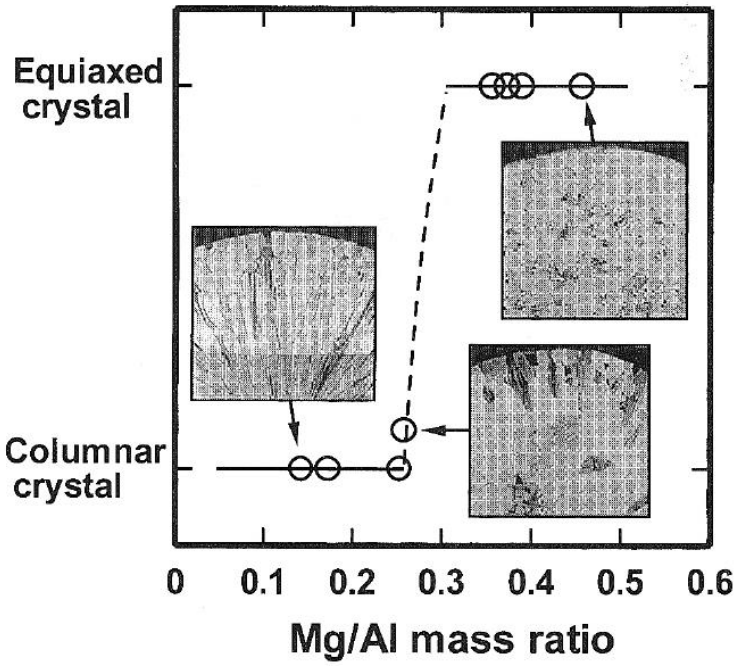

Figure 1-21. Effect of oxide composition, Mg/Al ratio, on solidification structure.[24)]

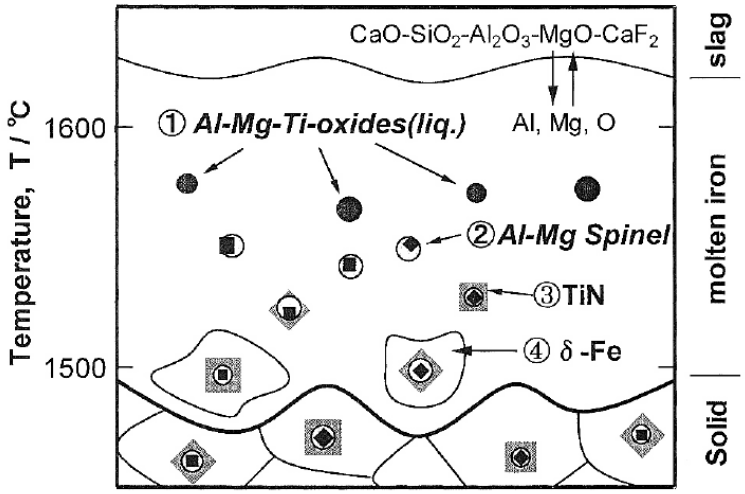

Figure 1-22. Schematic illustration of equiaxed crystals solidification in 16% Cr ferritic stainless steel assisted by inclusions.[24)]

Yu *et al.*[25] have investigated the change of grain size by re-heating from 1173 to 1573 K in the Al and Ti killed steels as shown in **Fig. 1-23**. They explained that the rapid increasing in some sections, i.e. from 1273 to 1373 K in Al-killed steel and from 1473 to 1573 K in Ti-killed steel, had been caused by the dissolution of fine precipitates which prevent the grain growth by pinning effect. Since, the fine particles have rather high surface energy hence the melting point of inclusions should be decreased than their own. Therefore, control of melting point of fine inclusions also can strongly affect the maximizing of pinning effect.

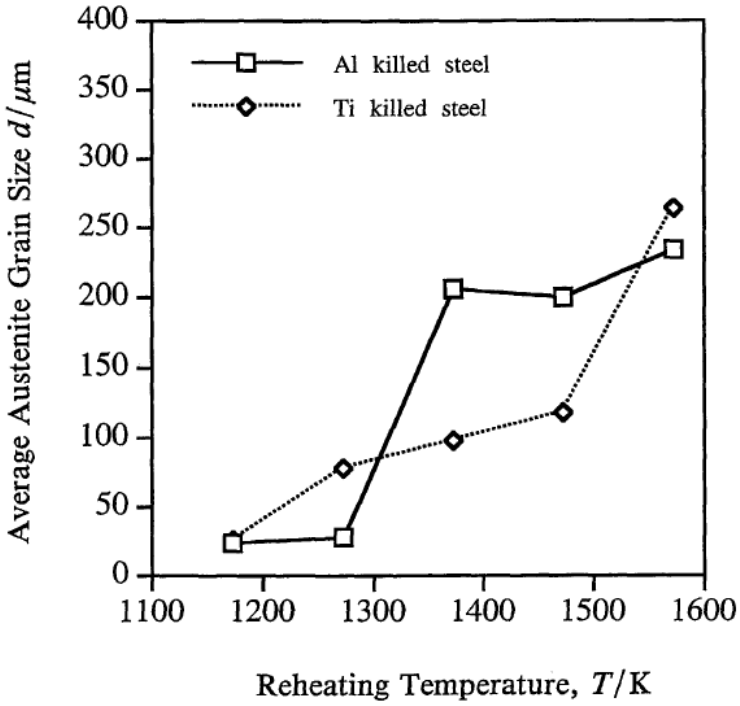

Figure 1-23. Mean austenite grain versus re-heating temperature for the Al and Ti steels, for 30 mins at the indicated temperature following a heating rate of about 9 K/s.[25]

Kikuchi *et al.*[26] have estimated the oxide particle radius during solidification with several cooling rates in low carbon high Mn steel as shown in **Fig. 1-24**. They concluded that the taken small oxide radius and high inclusion density by increasing cooling rate can give an advantage for formation of fine solidification structure.

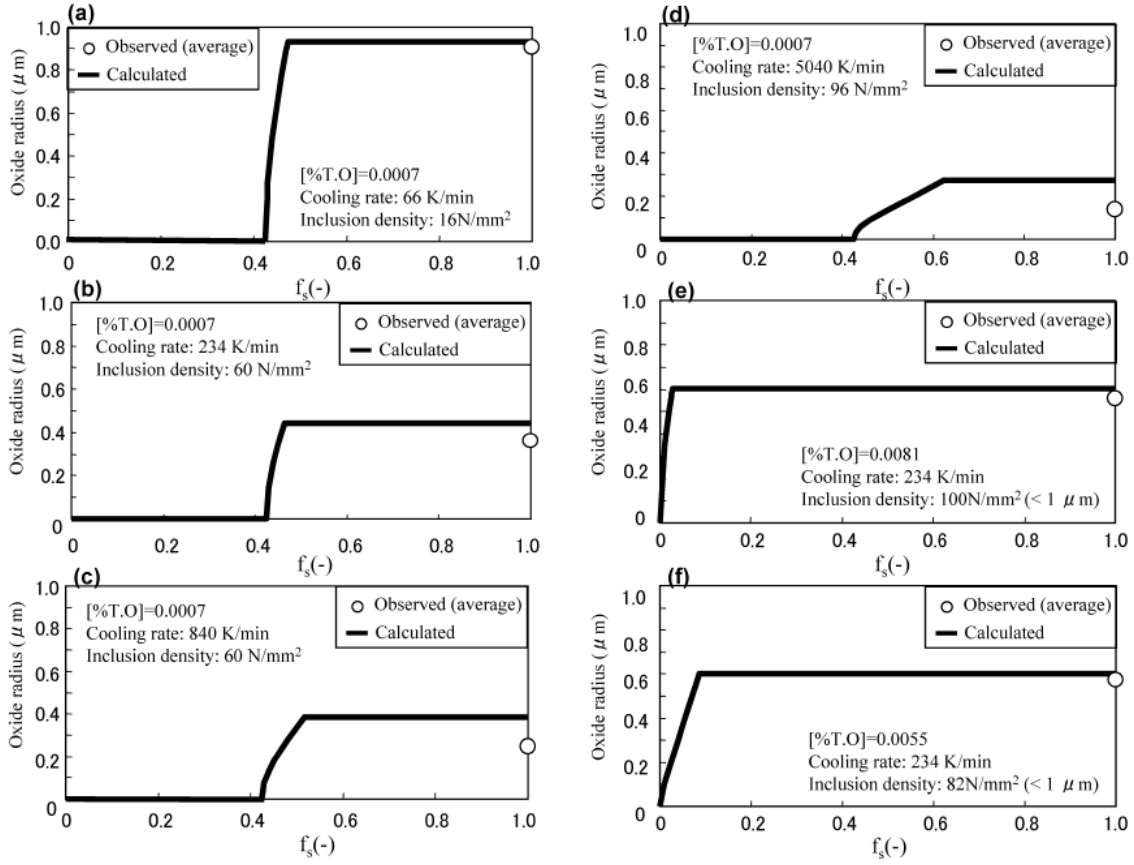

Figure 1-24. Changes of oxide particle radius during solidification.[26)]

Consequently, control of size of inclusions, uniformity of dispersion, oxide composition and melting point of precipitates all are quite important to obtain the fine microstructure during solidification and heat treatment. In order to handle such kinds of things, the morphology, size and chemical composition of primary inclusions at the deoxidation step are also obviously important since pre-existing particles can become the precipitation sites to be the beneficent inclusions for grain refining.

1.3 Objective and purpose of study

The main aim of present study is, for utilizing inclusions, clarification of effects of non-metallic inclusions in the fundamental alloy system as Fe-Al-Ti-O-N alloy which was produced by Al-Ti complex deoxidation on the microstructure by heating at 1473 K.

As previously mentioned in Sec. 1.2, the precipitated titanium nitride phases in various Ti bearing steels have strongly relevance to obtain fine grain structure. Many researchers have studied with several effects of inclusions, including titanium nitride, in the various grades of steel not fundamental alloy system, i.e. Fe-Al-Ti-O, on the solidification microstructure for utilizing inclusions. Therefore, in present study, effects of Al and Ti based inclusions provided by Al-Ti complex deoxidation on the microstructure in the fundamental alloy system as Fe-Al-Ti-O alloy have been studied.

First of all, clarification of evolutionary whole process of various inclusions, i.e. not only equilibrium and transient inclusions but also precipitates, should be basically required to understand formation and change behaviors of inclusions in the fundamental Fe-Al-Ti-O alloy system. Therefore, in Chapter 2, in order to observe the evolution of preferably diverse types of inclusions, various primary inclusions were produced at deoxidation step at 1873 K by controlling the addition amount of deoxidants aim at different stable oxide regions, e.g. Al_2O_3, Ti_3O_5, Ti_2O_3 and Al_2TiO_5 and holding time to obtain transient inclusions.

Nitrogen content is considerably correlated to the formation and growth of titanium nitride which can obviously affect grain refining as explained in Sec. 1.2.3. Therefore, in order to estimate the effect of nitrogen content on the formation and evolution behaviors of inclusions, nitrogen content was also regulated.

In Chapter 3, the formation and evolution of inclusions in solid state alloy have been observed. Finally, effect of the formed and evolved inclusions by heating on the microstructure was clarified by the analysis of microstructure of alloys in Chapter 4.

References

[1] W.Y. Cha, T. Miki, Y. Sasaki and M. Hino: *ISIJ Int.*, **48** (2008), pp.729-738.

[2] F. Ruby-Meyer, J. Lehmann and H. Gaye: *Scand. J. Metall.*, **29** (2000), pp. 206-212.

[3] I. Jung, G. Eriksson, P. Wu and A. D. Pelton: *ISIJ Int.*, **49** (2009), pp. 1290-1297.

[4] W.Y Kim, J.O. Jo, C.O. Lee, D.S. Kim and J.J. Pak: *ISIJ Int.*, **48** (2008), pp. 17-22.

[5] C. Wang, N.T. Nuhfer, and S. Sridhar: *Metall. Mater. Trans. B*, **40B** (2009), pp. 1022-1034.

[6] C. Wang, N.T. Nuhfer, and S. Sridhar: *Metall. Mater. Trans. B*, **48B** (2009), pp. 1005-1021.

[7] C. Wang, N.T. Nuhfer, and S. Sridhar: *Metall. Mater. Trans. B*, **41B** (2010), pp. 1084-1094.

[8] H. Matsuura, C. Wang, G. Wen and S. Sridhari: *ISIJ Int.*, **47** (2007), pp. 1265-1274.

[9] M.K. Sun, I.H. Jung and H.G. Lee: *Met. Mater. -Int.*, **14** (2008), pp. 791-798.

[10] D.C. Park, I.H. Jung, Peter C.H. Rhee and H.G. Lee: *ISIJ Int.*, **44** (2004), pp. 1669-1678.

[11] W.C. Doo, D.Y. Kim, S.C. Kang and K.W. Yi: *Met. Mater. -Int.*, **13** (2007), pp. 249-255.

[12] M.A. Van Ende, M. Guo, R. Dekkers, M. Burty, J. Van Dyck, P.T. Jones, B. Blanpain and P. Wollants: *ISIJ Int.*, **49** (2009), pp. 1133-1140.

[13] K. Inoue, I. Ohnuma, H. Ohtani, K. Ishida and T. Nishizawa: *ISIJ Int.*, **38** (1998), pp. 991-997.

[14] J.H. Park: *CALPHAD*, **35** (2011), pp. 455-462.

[15] S.C. Park, I.H. Jung, K.S. Oh and H.G. Lee: *ISIJ Int.*, **44** (2004), pp. 1016-1023.

[16] S. Ogibayashi: *Nippon Steel Technical Report*, **61** (1994), pp. 70-76.

[17] Y. Morikage, K. Oi, F. Kawabata and K. Amano: *Tetsu-to-Hagane*, **84** (1998), pp. 510-515.

[18] S. Matsuda and N. Okumura: *Transactions ISIJ*, **18** (1978), pp. 198-205.

[19] H. Ohta, R. Inoue and H. Suito: *ISIJ Int.*, **48** (2008), pp. 294-300.

[20] K. Takano, R. Nakao, S. Fukumoto, T. Tsuchiyama and S. Takaki: *Tetsu-to-Hagane*, **89** (2003), pp. 616-622.

[21] R.D. Doherty, D.J. Stolovitz, A.D. Roller and M.P. Anderson: *Scr. Metall.*, **21** (1987), pp. 675-679.

[22] N. Kikuchi, S. Nabeshima, Y. Kishimoto, T. Matsushita and S. Sridhar: *ISIJ Int.*, **47** (2007), pp.

1255-1264.

[23] T. Nishizawa: *Tetsu-to-Hagane*, **70** (1984), pp. 1984-1992.

[24] H. Fujimura, S. Tsuge, Y. Komizo and T. Nishizawa: *Tetsu-to-Hagane*, **87** (2001), pp. 707-712.

[25] D. Yu, D.P. Dunne, T. Chandra and F.J. Barbaro: *Materials Transactions, JIM*, **37** (1996), pp. 1554-1560.

[26] N. Kikuchi, S. Nabeshima, Y. Kishimoto and S. Sridhar: *ISIJ Int.*, **48** (2008), pp. 934-943.

Chapter 2. Formation of inclusions in Fe-Al-Ti-O-N alloy at deoxidation process

2.1 Introduction

In order to observe the evolution of various types of inclusions by heating for respective aims, several primary inclusions were produced at Al-Ti complex deoxidation step by controlling several conditions, e.g. addition amount of deoxidants, deoxidation time and crucible. The purposes of each parameter were elucidated as follows.

Basically, by adjustment of addition amount of deoxidants to aim at different stable oxide regions as shown in the phase diagram of oxides for the Fe-Al-Ti-O system at 1873 K[1] (**Fig. 2-1.**), it has been expected to obtain several types of oxide, i.e. Al_2O_3, Ti_3O_5 and Al_2TiO_5.

Second is controlling deoxidation time to produce the transient Al-Ti-O oxide inclusion, as seen in other studies, with a view to prediction of equilibrium oxide at 1473 K by measuring of evolution of chemical composition in the non-equilibrium oxide.

Lastly, for the evaluation of case of industrial condition, MgO crucible was used, since basic refractory, e.g. magnesia (MgO) based or dolomite ($CaMg(CO_3)_2$) refractory, has usually used for protecting furnace in industry.

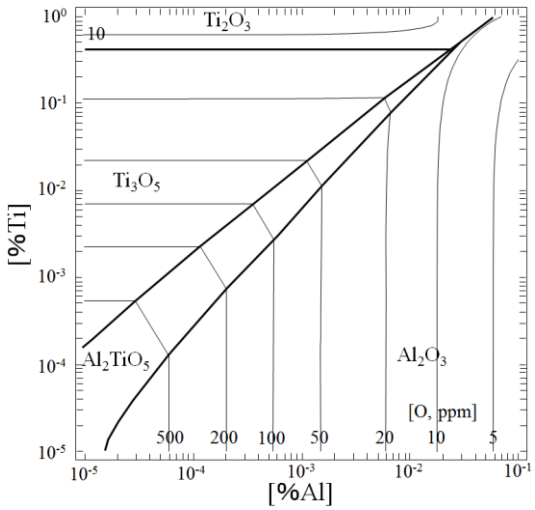

Figure 2-1. Stability diagram of oxide phases equilibrated with Fe-Al-Ti melt at 1873 K.[1]

2.2 Experimental procedure and analysis

2.2.1 Experimental procedure

Six kinds of Fe-Al-Ti-O-N alloys (hereafter, named as A, B, C, D, E and F) were prepared by several conditions as shown in **Table 2-1**. To clarify the formation and evolution behaviors of inclusions with or without oxide inclusions initially formed by complex deoxidation, the preformed oxide inclusions were collected at the outside of melt by the strong stirring. Therefore, an induction furnace was used in the present study.

Table 2-1. Alloy making conditions for each sample

Sample name	Crucible	Deoxidation type (holding time)	Atmosphere	Stable oxide region[1)]
A	MgO	1	Ar	Ti_3O_5
B	MgO	1	Ar	Boundary between Al_2O_3 and Al_2TiO_5
C	Al_2O_3	2	Ar	Al_2O_3
D	Al_2O_3	2	Ar+N_2	Al_2O_3
E	Al_2O_3	2	Ar	Ti_3O_5
F	Al_2O_3	2	Ar+N_2	Ti_3O_5

* Deoxidation Type 1: after Al and Ti additions, samples was kept for 10 min at 1873 K.

Deoxidation Type 2: after Al and Ti additions, samples was kept for 3 min at 1873 K.

In the case of A and B, about 200 g of electrolytic iron was put in an MgO crucible (OD 38 mm, ID 26 mm, height 123 mm) and the crucible was put in a quartz tube (OD 50 mm, ID 46 mm, length 360 mm). After the atmosphere of the reaction tube was replaced to high purity Ar gas (99.9 %, flow rate: about 400 cm^3/min), the sample was melted in an induction furnace (200 kHz, approximately 3

kW) at 1873 K for 1 h, in the case of MgO crucible, temperature was controlled for approaching to 1873 K for 1 hour, approximately. And then Al followed by Ti was added at an interval of 2 min. The melt was further kept for 10 min and then the crucible was taken out from the reaction tube and quenched by immersing a crucible into water.

In the case of C, D, E and F, about 100 g of electrolytic iron were melted in an Al_2O_3 Tammann tube (O.D.: 30 mm, I.D.: 24 mm, height: 150 mm) by using an induction furnace at 1873 K in Ar or Ar-N_2 atmosphere. For protecting of Al_2O_3 Tammann tube from thermal shock during increasing temperature, heating rate was carefully controlled until approaching 1873 K. The temperature was increased until 1873 K for around 230 min. Ar-N_2 gas mixture was introduced to add nitrogen in the melt. After melting, aluminum and titanium were added in sequence with the interval of 2 min. After holding 3 min, melt was quenched by immersing a crucible into water. The experimental installation was shown in **Fig. 2-2**.

The nitrogen content in the melt aimed at 100 ppm. And, suitable nitrogen partial pressure equilibrated with 100 ppm of nitrogen content in liquid iron was calculated using thermodynamic data for the dissolution of nitrogen in liquid iron as following equations.

$$\frac{1}{2}\mathrm{N_2(g)} = \underline{\mathrm{N}}(l\text{-Fe})$$

$$\Delta G^o = 9916 + 20.17T \ \mathrm{J/mol}$$

$$K = \frac{a_N}{\sqrt{P_{\mathrm{N_2}}}} = \frac{f_N[\%\mathrm{N}]}{\sqrt{P_{\mathrm{N_2}}}}$$

$$\log K = -\frac{518}{T} - 1.063$$

By computing data, 0.045 atm of nitrogen gas was introduced for 100 ppm of nitrogen in samples D and F.

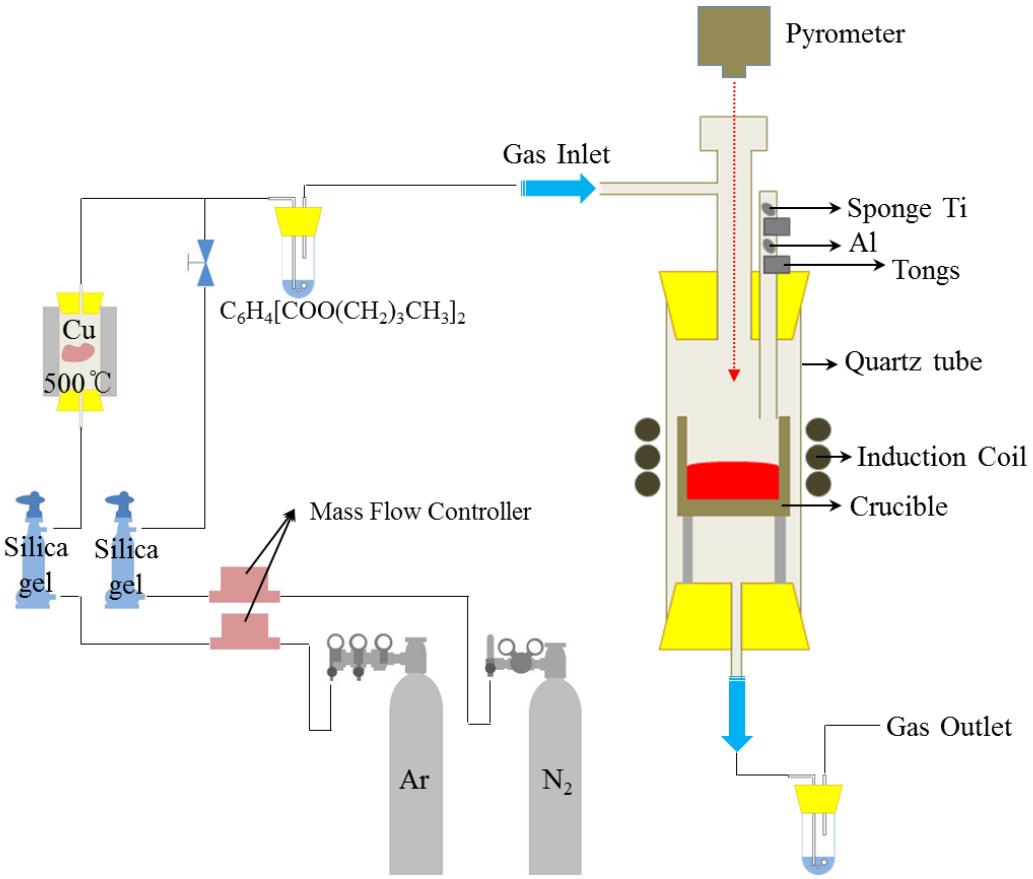

Figure 2-2. Sketch of experimental installation.

2.2.2 Analysis

2.2.2.1 Chemical analysis of samples

The compositions were analyzed by ICP-OES for soluble Al and Ti. Solutions were prepared as follows. About 1 g of steel pieces were cut off and dissolved into 40 ml of weak acid (HCl : HNO_3 : Pure water = 0.5 : 1 : 2.5) with low heat. And then, membrane filtration system with 0.45 μm membrane filter was used for eliminating the remaining inclusions in the solution.

And, total oxygen, nitrogen and sulfur in the metal were analyzed by using combustion analyzer (LECO TC600 and CSLS 600). Sulfur is mainly introduced from the electrolytic iron which contained 20 ppm of sulfur.

2.2.2.2 Analysis of Inclusion

As cast samples were embedded in the phenolic resin by using mounting machine (Struers, citopress-1), and polished by SiC papers and diamond suspensions up to 0.25 μm using polishing machine (Struers, TegraPol-11) to characterize the inclusions through observations by a field emission scanning electron microscope (FE-SEM, JEOL JSM-7001FA) and composition analyses by energy-dispersive spectrometry (EDS, JEOL JED-2300) attached to the FE-SEM. The parameters of polishing method are shown in **Table 2-2**.

Table 2-2. Parameters for polishing.

Paper No./ Abrasive paste size	320#	800#	1200#	1μm Diamond	0.25μm Diamond
Polishing time	10 min	5 min	5 min	30 min	30 min

More than 100 inclusions were observed and analyzed in each sample, and the compositions of Al, Ti, Fe, S, N and O were determined. In the present study, the size of an inclusion was defined as the maximal diameter of that particle. And, phase of inclusions was judged by not only point and mapping analysis but also shape of inclusion, especially titanium nitride.

Also, 3 dimension analysis of inclusion was carried out using etching technique as follows. Before etching step, procedures of sample preparation for 3D analysis were same with sample preparation process for FE-SEM analysis. And then, sample which finished polishing was etched with 5%Br+methanol solution for 20 sec. After etching, solution was absorbed by filter paper without touching surface of sample. The surface of sample was washed with methanol and methanol was removed by filter paper. This washing step was repeated 10 times at least. And then the sample surface was dried with light winds. The inclusions in the prepared sample were analyzed by using FE-SEM+EDS.

2.2.2.3 Judgment method of inclusion phase by FE-SEM and EDS

In the present research, phase of inclusions was judged by using not only point and mapping analysis but also SEM image.

First of all, number of phases in the inclusion was approximately checked on the SEM screen. If inclusion has just one phase at this step, phase of inclusion is determined by point analysis result.

If inclusion consists of at least two phases, point analysis is carried out in each phase. In the case of analysis result of large phase at which peaks are not affected by near other phase, phase of inclusion is determined by point analysis result. However, in the case of small phase, i.e. formed or precipitated phase on the edge or surface of large phase, existence of influence of near large phase was judged by mapping analysis result.

For example, **Figure 2-3** shows analysis results of point and mapping analyses. As shown in **Fig. 2-3**, considering point analysis result only, grey and dark parts both seem Al-Ti-O phase of dissimilar chemical compositions. However, Al, Ti and O peaks in dark and grey areas can affect each other, since grey and dark areas are too small approximately 1 μm. Therefore, mapping analysis is carried out and mapping results of Al and Ti is checked. From mapping data, Al peak is not detected in the grey part. On the contrarily, Al peak is just detected in the dark part. Consequently, inclusion consisted of grey and dark parts can be determined two phase inclusion which composed Al_2O_3 and TiO_x phases. In other words, 8.7 mass% of Al at point 1 and 3.0 mass% of Ti at point 2 can be ignored.

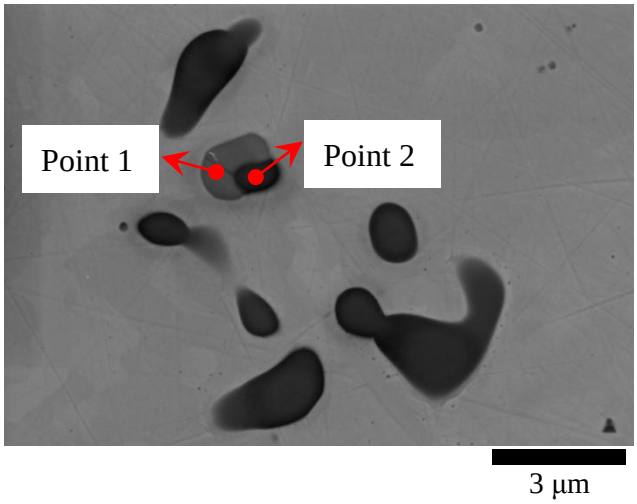

(mass%)

Point analysis	Al	Ti	O
1	8.7	40.0	51.3
2	50.1	3.0	46.9

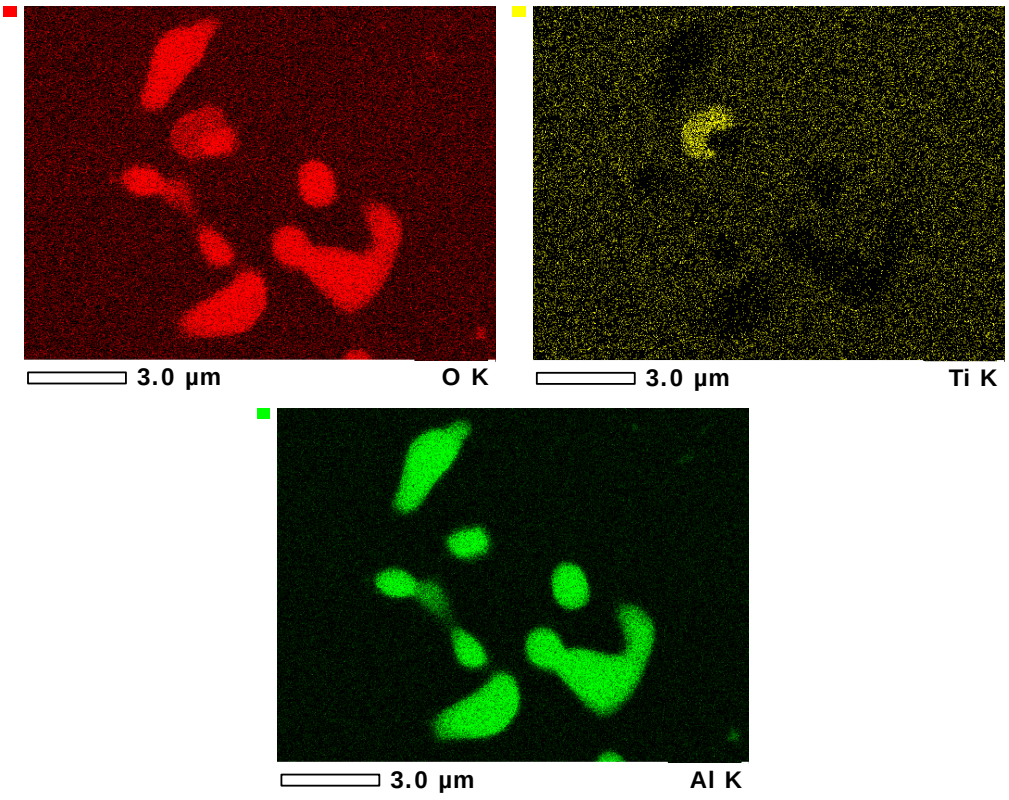

Figure 2-3. Analysis results of point and mapping analyses.

2.3 Results and discussion

The compositions of six kinds of samples were described as summarized in **Table 2-3**. The compositions of samples were also shown on the previously reported stable oxide phase diagram at 1873 K[1)] in **Fig. 2-4**. At deoxidation temperature as 1873 K, the stable oxide phase of samples A, E and F is expected to be Ti_3O_5, while that of samples C and D is to be Al_2O_3. And, that of sample B is predicted to Al_2TiO_5. In the case of sample A, even if Al was added, Al was not detected since all amount of Al consumed for deoxidation. Although aimed nitrogen content for the samples D and F was 100 ppm both, the analyzed nitrogen contents in the samples D and F were 58 and 55 ppm, respectively, due to the effect of other elements. And, in the case of samples A, B, C and E, nitrogen content was introduced from electrolytic iron. Furthermore, sulfur from 15 to 20 ppm was analyzed in the samples. Sulfur comes from electrolytic iron, as previously mentioned in Sec. 2.2.2.1.

Table 2-3. Metal compositions for each sample. (mass%)

Sample Name	Soluble Al	Soluble Ti	Total O	Total N	Total S
A	0.0000	0.277	0.0006	0.0004	0.0015
B	0.0064	0.036	0.0060	0.0010	0.0020
C	0.0274	0.089	0.0005	0.0005	0.0017
D	0.0392	0.093	0.0007	0.0058	0.0012
E	0.0003	0.109	0.0012	0.0013	0.0020
F	0.0009	0.123	0.0010	0.0055	0.0017

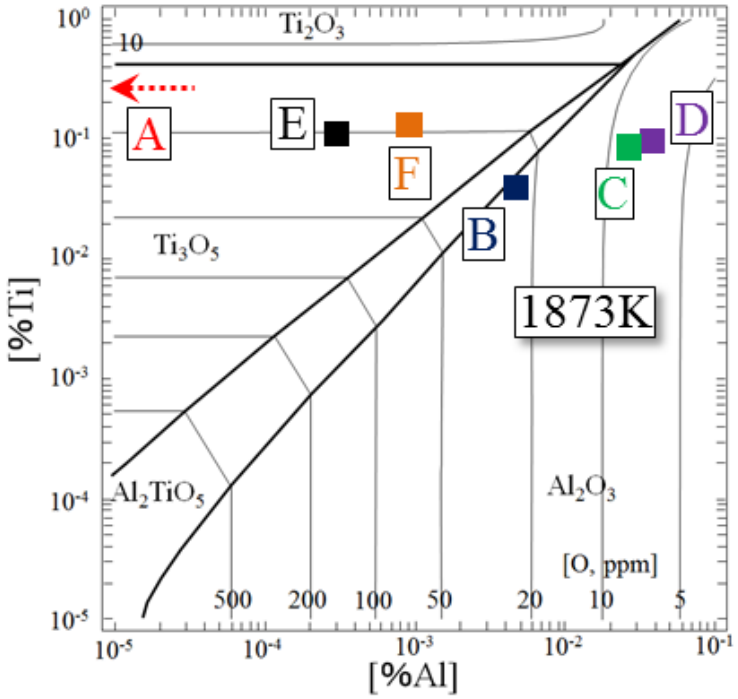

Figure 2-4. Metal composition on stability diagram of oxide phases equilibrated with Fe-Al-Ti melt at 1873 K.[1)]

2.3.1 Overall of areas of observed inclusions

In all as cast samples, the inclusions observation areas on the cross section of the cylindrical shaped as-cast samples were classified into two regions by morphology of inclusions. The schematic representation of cross section of two types of cylindrical shaped as cast samples was shown in **Fig. 2-5**. The radiuses of samples were 24 and 26 mm depending on crucible internal diameter. The grey area named as "Outer layer" is the cylindrical pipe shape and "Inner layer" is the inside of the outer layer described as green area. The thickness of outer layers in all samples was dissimilar even in a same sample depending on distance from top surface of sample.

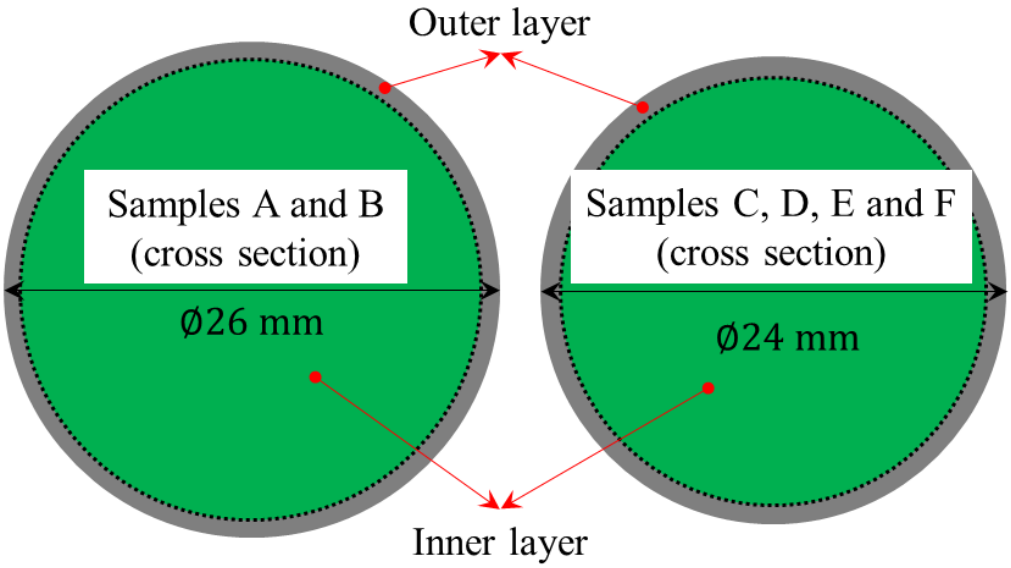

Figure 2-5. Schematic drawing of the classification of the observation regions.

In the outer layer in all samples, oxide based inclusions were usually observed. On the contrary, nitride and sulfide inclusions were mainly observed in the inner layer of all samples. The difference in morphology between two regions can be considered that the preformed oxide inclusions which formed by complex deoxidation were removed from the "Inner layer" by the inductive force. Therefore, inclusions with or without oxide inclusions were collected at two regions by the strong stirring as planned.

2.3.2 Outer layer

Outer layers have two types of morphology of inclusions with crucible type, e.g. porous MgO and non-porous Al_2O_3 crucibles. In the case of samples A and B by using MgO crucible, outer layer has two dissimilar areas at inclusion morphology in each sample. On the other hand, morphology of the produced inclusions in outer layer by using Al_2O_3 crucible is just one type. The illustration and SEM pictures of outer layers in each sample were shown in **Figs. 2-6, 2-7 and 2-8**. Description of inclusions as "X+Y" means that there are two different X and Y phases in one inclusion particle and "X-Y" denotes that two components in one phase of inclusion.

In the sample A, "Area 1" mainly consists of cluster type of Al_2O_3 based inclusions, i.e. Al_2O_3 and Al_2O_3+TiN, as shown in **Fig. 2-6**. Some Al_2O_3+TiS, Al_2O_3+TiS+TiN, Al_2O_3+TiO_x+TiN and (MgO-Al_2O_3)+Al_2O_3+TiN were observed. On the other hand, multi-phase inclusion which consists of various oxides and a lot of small Al_2O_3-TiO_x inclusions were observed in the area named as "Area 2".

In the case of sample B, cluster type of Al_2O_3 and/or Al_2O_3-MgO based inclusions almost observed in the "Area 1", e.g. Al_2O_3, Al_2O_3+TiN, (Al_2O_3-MgO), (Al_2O_3-MgO)+TiN and Al_2O_3+(Al_2O_3-MgO)+TiN. Various types of inclusions were observed as Al_2O_3+(Al_2O_3-MgO), (Al_2O_3-MgO-TiO_x), Al_2O_3+(Al_2O_3-MgO-TiO_x), Al_2O_3+TiO_x+(Al_2O_3-MgO)+TiN, (Al_2O_3+TiO_x) and (Al_2O_3-MgO)+(Al_2O_3-TiO_x). And, "Area 2" in the sample B was composed of small Al_2O_3-TiO_x inclusions and some of multi-phase inclusions.

The outer layer in the samples C, D, E and F produced by using Al_2O_3 crucible has just one area consist of Al_2O_3 based inclusions similar with "Area 1" in the samples A and B. However, the observed inclusions in samples C, D, E and F were not same with each other due to different metal compositions. The image of SEM in the **Fig. 2-8** was typical morphology of sample D.

The existence of "Area 2" might be resulted from amount of produced oxygen by crucible. Since interaction parameter between Ti and Mg is high negative value than Al and Mg ($e_{\mathrm{Mg}}^{\mathrm{Ti}} = -0.64$,

$e_{\mathrm{Mg}}^{\mathrm{Al}} = -0.27$) [2], titanium in melt can be caused dissolution of Mg from crucible than aluminum in melt. In addition, porous MgO crucible can be easily dissolved into the melt than dense Al_2O_3 crucible, since reaction area between melt and crucible is much larger in the case of MgO crucible. Therefore, in the case of MgO crucible, much more oxygen would be dissolved, and then the produced oxygen reacts with Al, Ti, Fe and Mg at close area of crucible.

The thickness of "Area 2" in samples A and B was dissimilar. In the case of sample A, thickness of "Area 2" was 200 μm approximately. On the contrary, thickness of "Area 2" was just around 85 μm in sample B. This kind of tendency can be explained by Ti content in melt. As previously mentioned, $e_{\mathrm{Mg}}^{\mathrm{Ti}}$ is very negative value. Therefore, high Ti content in melt can be accelerated dissolution of Mg from crucible. Since Ti content in sample A was 10 times than that in the sample B, more oxygen would be dissolved from the crucible. Therefore, thickness of "Area 2" in sample A was much larger than that in sample B.

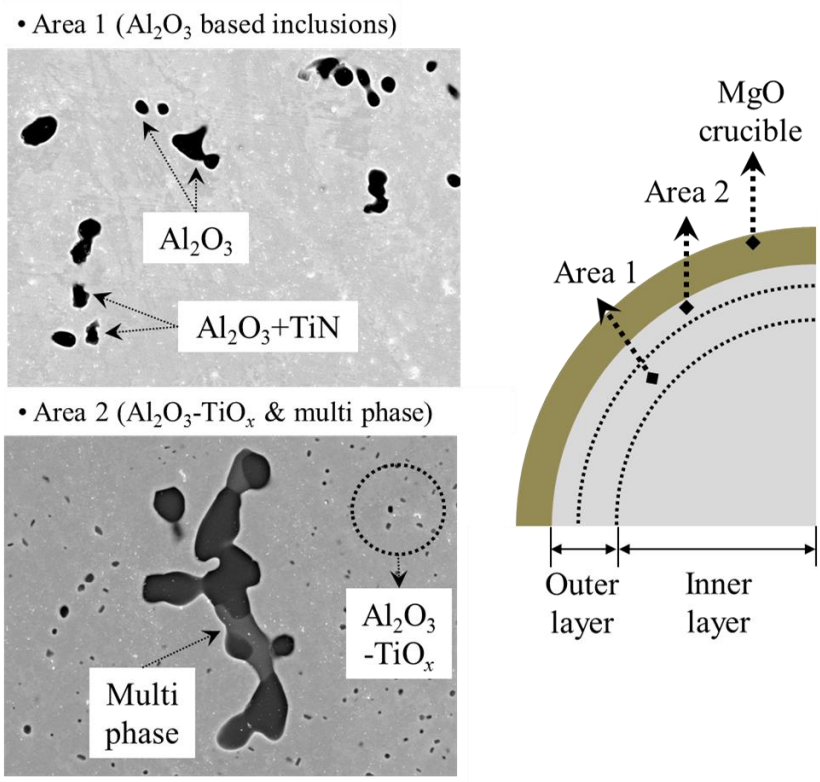

Figure 2-6. Illustration and SEM pictures of outer layers in sample A.

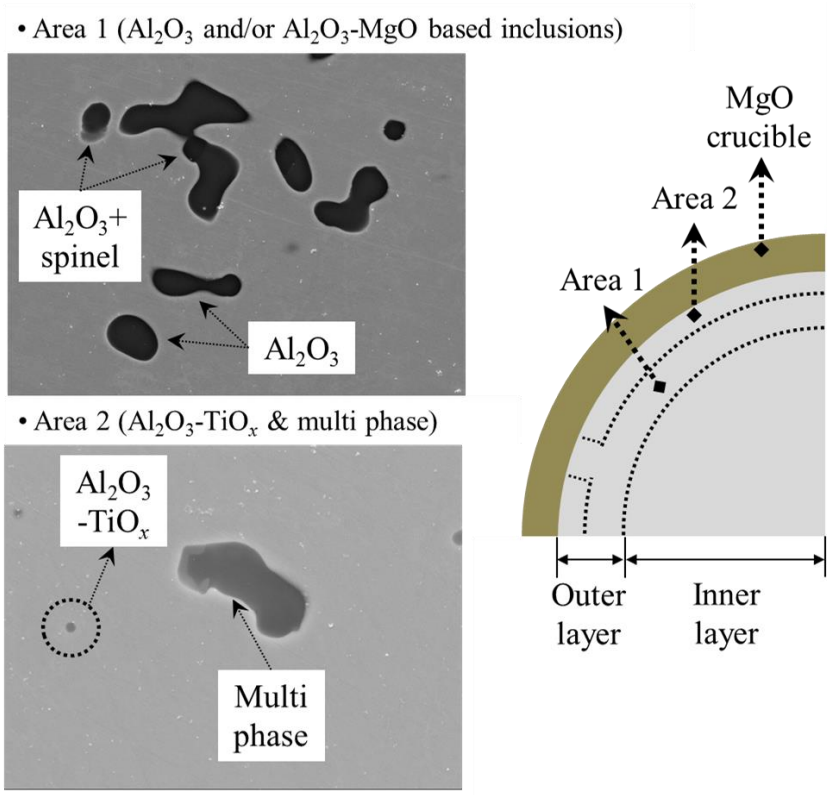

Figure 2-7. Illustration and SEM pictures of outer layers in sample B.

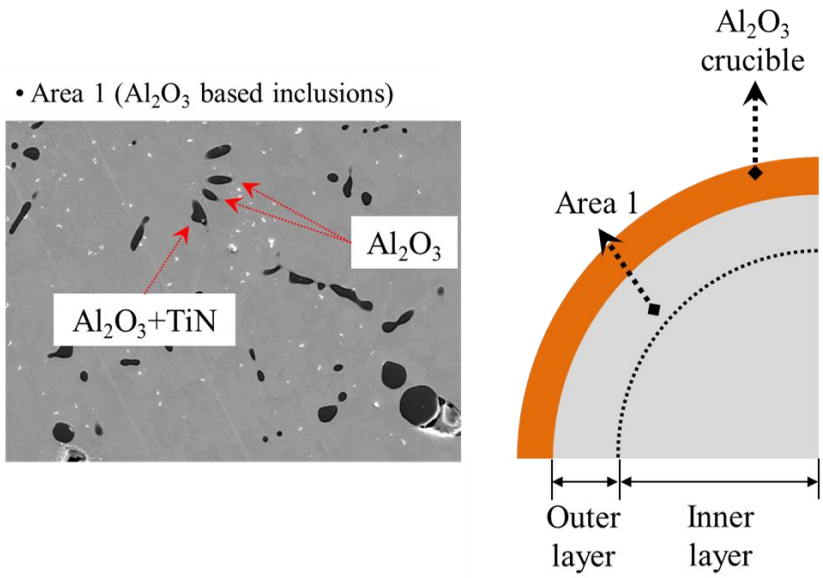

Figure 2-8. Illustration and SEM pictures of outer layers in samples C, D, E and F.

2.3.2.1 Type and composition of inclusions in outer layer

In Sec. 2.3.2, type of inclusions in outer layer introduced roughly. As explained, “Area 2” was just detected in the samples A and B. Many inclusions with high Fe content in the “Area 2” of both samples A and B were detected in comparison with Fe content of similar sized inclusions in the “Area 1”. However, judgment of existence of Fe oxide phase in inclusions by EDS observation was impossible, even if maximum 48 mol% of Fe content was detected in the some inclusions near the crucible, because Fe peak in inclusions should be affected by Fe matrix depending on inclusion size. The detected Fe content of inclusions in the samples A and B with distance from the surface of MgO crucible side was expressed in **Fig. 2-9**. “Other Inclusions” in **Fig. 2-9** means all inclusions except small Al_2O_3-TiO_x inclusions. Fe content in inclusions increased with decreasing distance in both samples A and B. It seems that the inclusions near the crucible wall consist of iron oxide phase by reaction between iron and dissolved oxygen from crucible.

In addition, Al_2O_3-TiO_x inclusions were just observed in the “Area 2”. The formation mechanism of small Al_2O_3-TiO_x inclusions will be discussed in Sec. 2.3.2.2. The average composition of small Al_2O_3-TiO_x inclusions was shown in **Table 2-4**. Mainly Al, Ti and Fe peaks were detected by EDS in Al_2O_3-TiO_x inclusions. However, observed Fe peak was ignored, since Fe peak in Al_2O_3-TiO_x inclusions, which are tiny particles approximately 1μm, might be influenced by Fe matrix. In the sample A, Al_2O_3-TiO_x inclusion consists of 18 mol% Al and 82 mol% Ti. On the other hand, Al_2O_3-TiO_x inclusion composed 60 mol% Al and mol% Ti in the sample B. The difference of chemical composition between Al_2O_3-TiO_x inclusions in two samples can be explained by equilibrium oxide depending on metal compositions.(Sec. 2.3. **Fig.2-4.**) At the metal composition of sample A, predicted equilibrium oxide was Ti_3O_5, whereas expected equilibrium oxide was Al_2TiO_5 in the case of sample B. Although detected chemical composition of Al_2O_3-TiO_x inclusions in two samples were not completely same with equilibrium oxide, it seems that observed and expected compositions of oxide exhibited considerably similar tendency. Furthermore, assuming Al_2O_3-TiO_x

inclusions in both of alloys were formed by identical mechanism, the greatest effect on formation of inclusion between two samples might be difference of metal compositions.

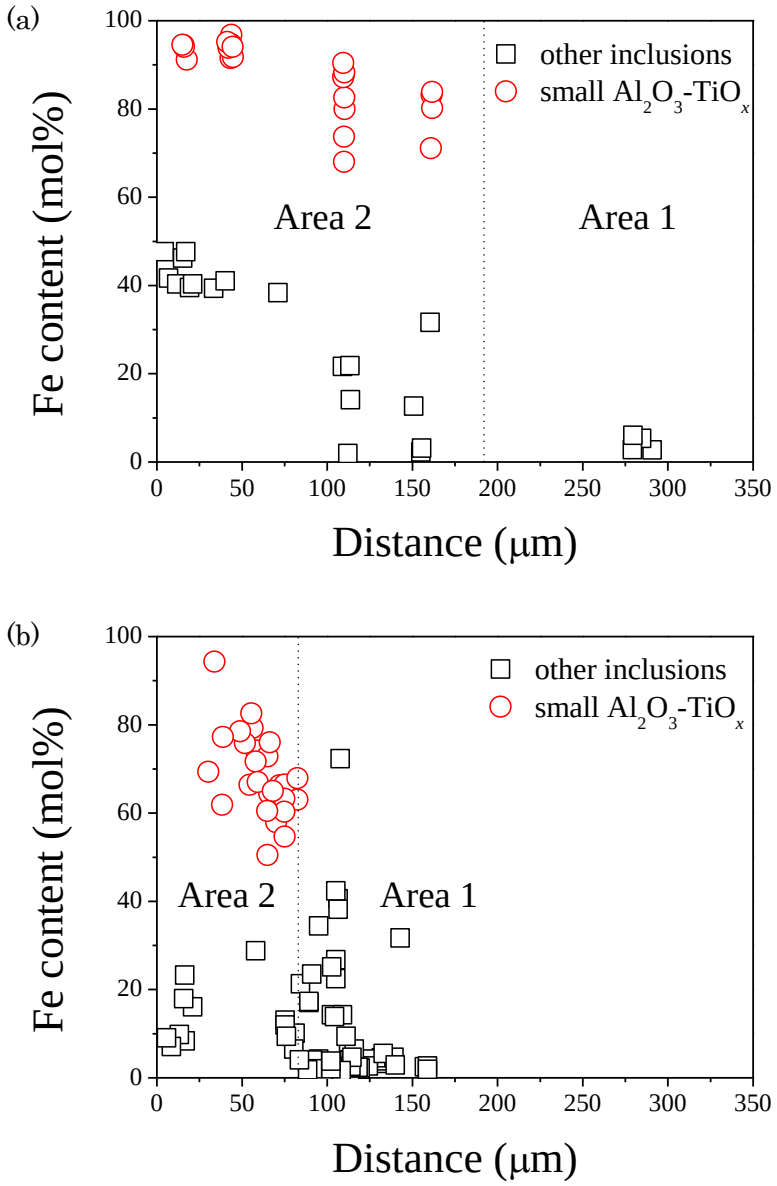

Figure 2-9. Fe content of inclusions with distance in samples (a) A and (b) B.

Table 2-4. Average composition of small Al_2O_3-TiO_x inclusions in "Area 2" of outer layer of samples A and B (mol%)

Sample name	Average Composition	
	Al	**Ti**
A	18	82
B	60	40

The type of inclusions in "Area 1" of samples A and B is shown in **Table 2-5**. And, **Figure 2-10** shows type of inclusions in samples C, D, E and F. Since various types of inclusions in the case of samples A and B were observed, type of inclusion described by using table to see it more clearly. As shown in **Table 2-5**, Al_2O_3-MgO based inclusions such as Al_2O_3-MgO, Al_2O_3-MgO-TiO_x were observed in the both of samples, however the ratio of Al_2O_3-MgO based inclusions in sample A was 3%, on the contrary 45% of Al_2O_3-MgO based inclusions were observed in sample B.

Table 2-5. Observed inclusion types in "Area 1" of outer layer of samples A and B (%)

Inclusion type	Sample name	
	A	**B**
Al_2O_3	49	31
Al_2O_3+TiN	39	22
Al_2O_3+TiS	3	-
Al_2O_3+TiN+TiS	6	-
(Al_2O_3-MgO)	-	11
(Al_2O_3-MgO)+TiN	-	9
Al_2O_3+(Al_2O_3-MgO)	-	4
Al_2O_3+(Al_2O_3-MgO)+TiN	2	11
Al_2O_3+(Al_2O_3-MgO)+TiN+TiS	1	-
(Al_2O_3-MgO-TiO_x)	-	2
Al_2O_3+(Al_2O_3-MgO-TiO_x)	-	4
Al_2O_3+TiO_x	-	2
Al_2O_3+TiO_x+TiN	1	-
Al_2O_3+TiO_x+(Al_2O_3-MgO)+TiN	-	2
(Al_2O_3-MgO)+(Al_2O_3-TiO_x)	-	2

- : not detected

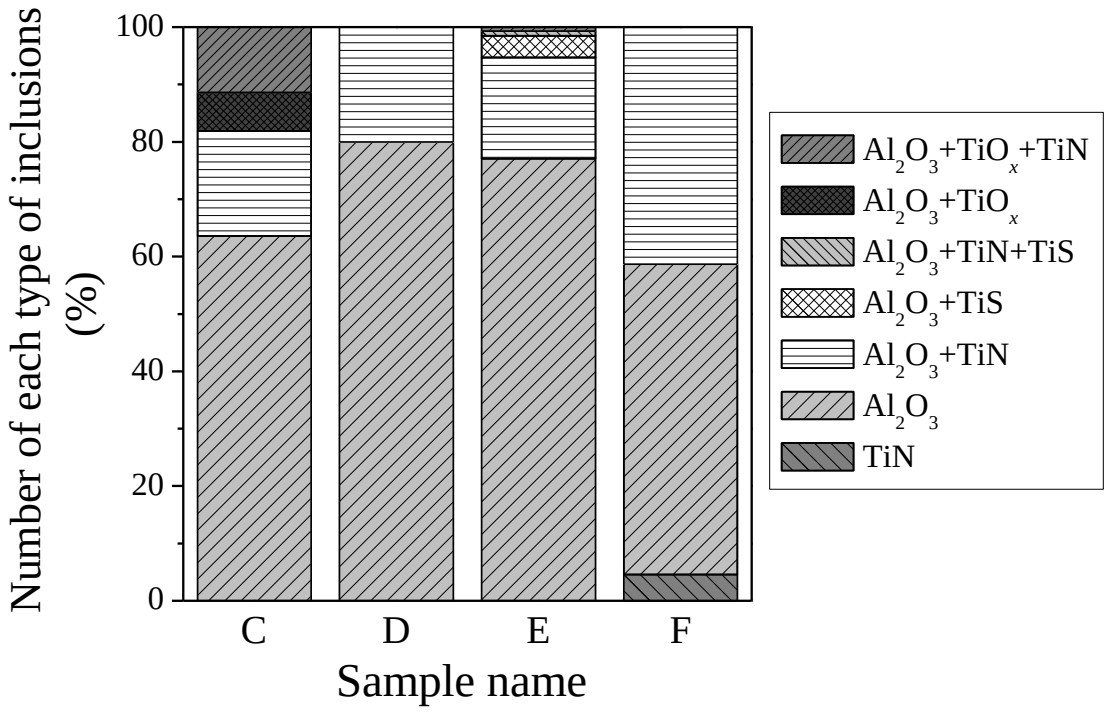

Figure 2-10. Observed inclusion types in "Area 1" of outer layer of samples C, D, E and F.

As explained in Sec. 2.3.2, dissolution of Mg was more easily occurred in sample A than sample B. However, Al_2O_3-MgO based inclusion was formed in sample B. It would be expounded by application of stability diagram of the Fe-Mg-Al-O system at 1873 K as shown in **Fig. 2-11**. [3] Surely, Seo *et al.*[3] did not consider Ti content in the melt for calculation of Mg-Al-O stability diagram at 1873 K. Nevertheless, metal composition of sample B can be just described as red allow in **Fig. 2-11**, by assuming Mg content in melt was less than 1 ppm. Obviously, Mg-Al-O stability diagram should be changed due to 360 ppm of Ti. However, consequentially, 45% of Al_2O_3-MgO based inclusions were observed in sample B. From these results, it can be considered that metal composition of sample B was still on the spinel ($MgO \cdot Al_2O_3$) stable region.

On the other hand, mainly Al_2O_3 based inclusions were observed not Al_2O_3-MgO based inclusions in sample A. Considering stable oxide by using Mg-Al-O stability diagram, MgO is probably expected inclusion in sample A. However, Mg-Al-O stability diagram might be changed high Ti

content (2770 ppm) in sample A. Therefore, it seems that metal composition of sample A is not on the MgO or spinel stable regions anymore due to high Ti content which is approximately 10 times larger than that in the sample B.

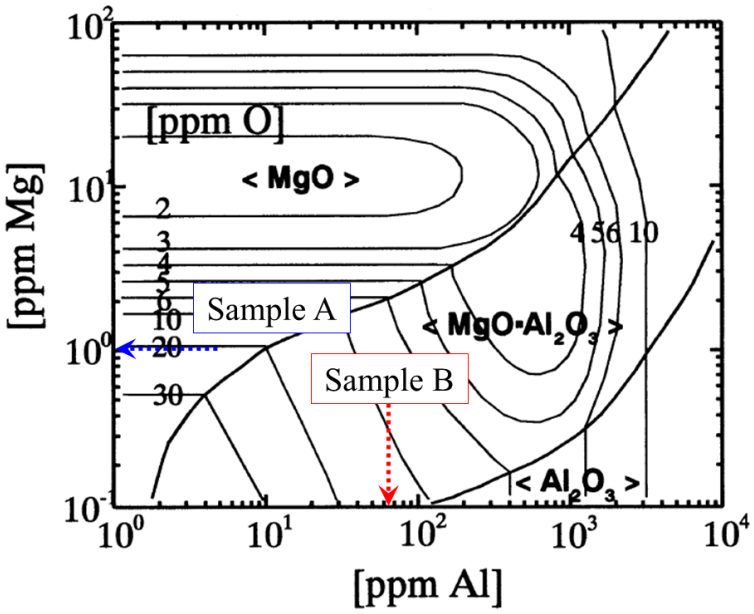

Figure 2-11. Stability diagram of Fe-Mg-Al-O system at 1873 K.[3)]

In the outer layer, mostly Al_2O_3(+TiN) inclusions were observed in the C, D, E and F as shown in **Fig.2-10**. In the sample C, some of the Al_2O_3+TiO_x(+TiN) inclusions were observed. And some of Al_2O_3+TiO_x+TiN and TiS-based inclusions were detected in the sample E. In the sample F, a fewer number of TiN particles were observed.

Oxide inclusions in all samples are produced by Al–Ti deoxidation reaction and it is considered that oxide inclusions were accumulated by the inductive flow of the melt and adhesion onto the crucible surface. However, TiN in all samples and TiS phase in samples A and E can be explained as follows.

The soluble nitrogen content of each sample at TiN saturating condition at 1873 K was calculated by **Eq. (2-1)** with soluble Al and Ti contents shown in **Table 2-3** in Sec. 2.3 and interaction parameters as shown in **Table 2-6**. As shown in **Fig. 2-12**, the calculated nitrogen content was in the

range from 0.0081 to 0.0628 mass%, which was much larger than total nitrogen content in all samples shown in **Table 2-3**. Therefore, TiN inclusions observed as independent particles or attached on the surface of oxide inclusions are formed due to the segregation of Ti and N during quenching.

$$TiN(s) = Ti\ (mass\%) + N\ (mass\%) \qquad \log K = -19{,}800/T + 7.78\ ^{4)} \tag{2-1}$$

Table 2-6. Interaction parameter at 1873 K.[4), 5)]

e_i^j	Ti	N	S	Al	O
Ti	0.042[4)]	-2.04[4)]	-0.27[4)]	0.026[5)]	-1.62[4)]
N	-0.503[4)]	0[4)]	0.007[4)]	0.01[4)]	-0.12[4)]
S	-0.18[4)]	0.01[4)]	-0.046[4)]	0.041[4)]	-0.27[4)]

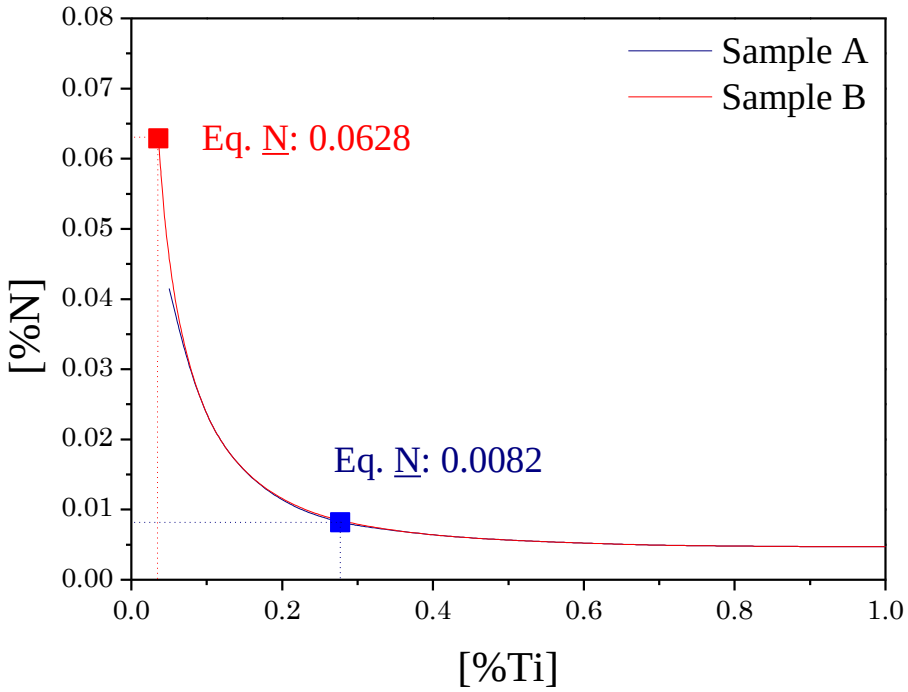

Figure 2-12. Equilibrium relationship between Ti and N inclusions in samples A and B.

TiS formation in outer layer of samples A and E could be explained as follows. Assuming the interaction parameters during quenching are equal to those at 1873 K,[4), 5)], activity of sulfur in samples A and E is 0.00134 and 0.00191, respectively. It is the large value among six samples. On the other hand, activity of titanium in the sample A is the largest of 0.2831. As a result, the product of the sulfur and titanium activities of the samples A and E is the large values as 0.00038 and 0.00021 than that of the other samples and thus it is expected that the formation of TiS inclusion in the samples A and E is most advantageous.

In the samples C, D, E and F, transient inclusions can be observed as aimed. In the case of samples C and D, Al_2O_3 is thermodynamically the stable oxide at 1873 K as shown in **Fig. 2-4**. On the other hand, TiO_x is the stable oxide at the metal composition of samples E and F. Nevertheless, Al_2O_3 inclusions were also mainly observed in those samples. It would be explained that the holding time after Ti addition is too short to convert the firstly formed Al_2O_3 inclusions into the stable TiO_x inclusions completely. Al_2O_3 inclusions in the samples E and F could be considered one of the transient inclusions as mentioned in Sec. 2.1.

In the samples C and E with relatively small nitrogen contents, some (Al_2O_3+TiO_x)-based inclusions with the diameter of more than 3.5 μm were observed. Similar (Al_2O_3+TiO_x)-based inclusions have reported by several investigators as introduced in literature review in Sec. 1.2.1.2. **Figure 2-13** shows the SEM images of the observed (Al_2O_3+TiO_x)-based inclusions in samples C and E. It consists of two phases, namely Al-rich oxide and Ti-rich oxide phase. **Figure 2-14** shows mole fractions of Al, Ti and Fe in (Al_2O_3+TiO_x)-based inclusions in sample C on the Al-Ti-Fe ternary composition diagram calculated from measured compositions of Al_2O_3-TiO_x-FeO oxide inclusions, since the measured peaks are mainly Al, Ti and Fe. The oxide phase rich in Ti could be TiO_x, since the Al peak detected by EDS in Ti-rich phase would be from the Al-rich phase because of the fine structure of Ti-rich phase. In the case of samples D and F, (Al_2O_3+TiO_x)-based inclusions were not detected.

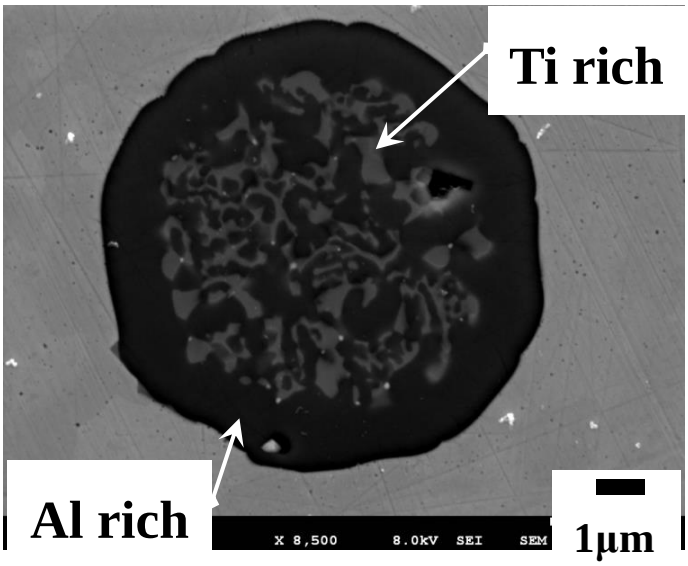

Sample C

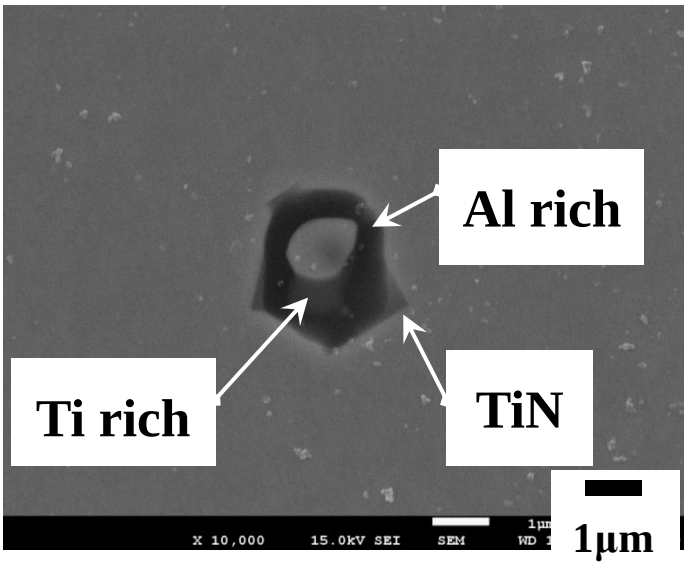

Sample E

Figure 2-13. SEM images of the observed (Al_2O_3+TiO_x)-based inclusions in samples C and E.

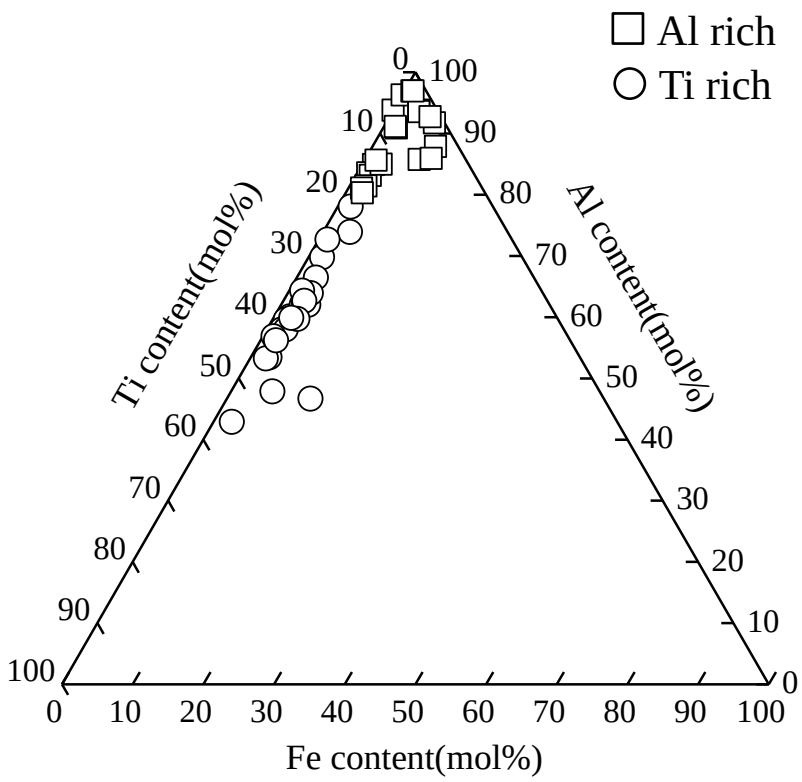

Figure 2-14. Chemical composition of the observed (Al_2O_3+TiO_x)-based inclusions on the Al-Ti-Fe ternary in sample C.

2.3.2.2 Size of inclusions in outer layer

Average size of the observed inclusions in the "Area 1" of all samples was shown in **Table 2-7**.

Table 2-7. Average size of the observed inclusions in the "Area 1" of all samples. (μm)

Inclusion type	Sample name					
	A	**B**	**C**	**D**	**E**	**F**
TiN	-	-	-	-	-	1.8
Al_2O_3	2.9	3.5	2.9	1.9	3.1	2.5
Al_2O_3+TiN	4,6	4.5	4.6	3.4	3.8	3.8
Al_2O_3+TiS	3.7	-	-	-	2.7	-
Al_2O_3+TiN+TiS	7.4	-	-	-	-	-
(Al_2O_3-MgO)	-	3.4	-	-	-	-
(Al_2O_3-MgO)+TiN	-	3.4	-	-	-	-
Al_2O_3+(Al_2O_3-MgO)	-	4.8	-	-	-	-
Al_2O_3+(Al_2O_3-MgO)+TiN	6.4	8.5	-	-	-	-
Al_2O_3+(Al_2O_3-MgO)+TiN+TiS	6.8	-	-	-	-	-
(Al_2O_3-MgO-TiO_x)	-	5.4	-	-	-	-
Al_2O_3+(Al_2O_3-MgO-TiO_x)	-	7.4	-	-	-	-
Al_2O_3+TiO_x	-	5.7	9.2	-	-	-
Al_2O_3+TiO_x+TiN	11.2	-	8.2	-	3.1	-
Al_2O_3+TiO_x+(Al_2O_3-MgO)+TiN	-	4.2	-	-	-	-
(Al_2O_3-MgO)+(Al_2O_3-TiO_x)	-	3.2	-	-	-	-

- : not detected

As shown in **Table 2-7**, size of multi-phase oxide was much larger than that of single phase oxide. For example, in the sample B, average sizes of Al_2O_3, (Al_2O_3-MgO), (Al_2O_3-MgO-TiO_x) inclusions were 3.5, 3.4 and 5.4 μm, respectively. On the other hand, average size of Al_2O_3+TiO_x, Al_2O_3+(Al_2O_3-MgO), and Al_2O_3+(Al_2O_3-MgO-TiO_x) inclusions were 5.7, 4.8 and 7.4 μm, respectively.

In addition, TiN and/or TiS precipitated oxide inclusions were certainly much bigger than oxide inclusions. For example, size of Al_2O_3 inclusions was from 1.9 to 3.5 μm in all samples. On the other hand, size of Al_2O_3+TiN, Al_2O_3+TiS and Al_2O_3+TiN+TiS inclusions was from 2.7 to 7.4 μm.

Size distribution of inclusion in the "Area 1" of outer layer of all samples was shown in **Figs 2-15, 2-16 and 2-17**. The number of observed inclusions in the "Area 1" in samples A, B, C, D, E and F was 101, 54, 60, 85, 131 and 109, respectively. As shown in **Figs 2-15, 2-16 and 2-17**, overall, size of the observed inclusions in the samples A and B was much larger than that in the samples C, D, E and F. This tendency in the samples A and B might be due to the long holding time at which inclusion was agglomerated each other.

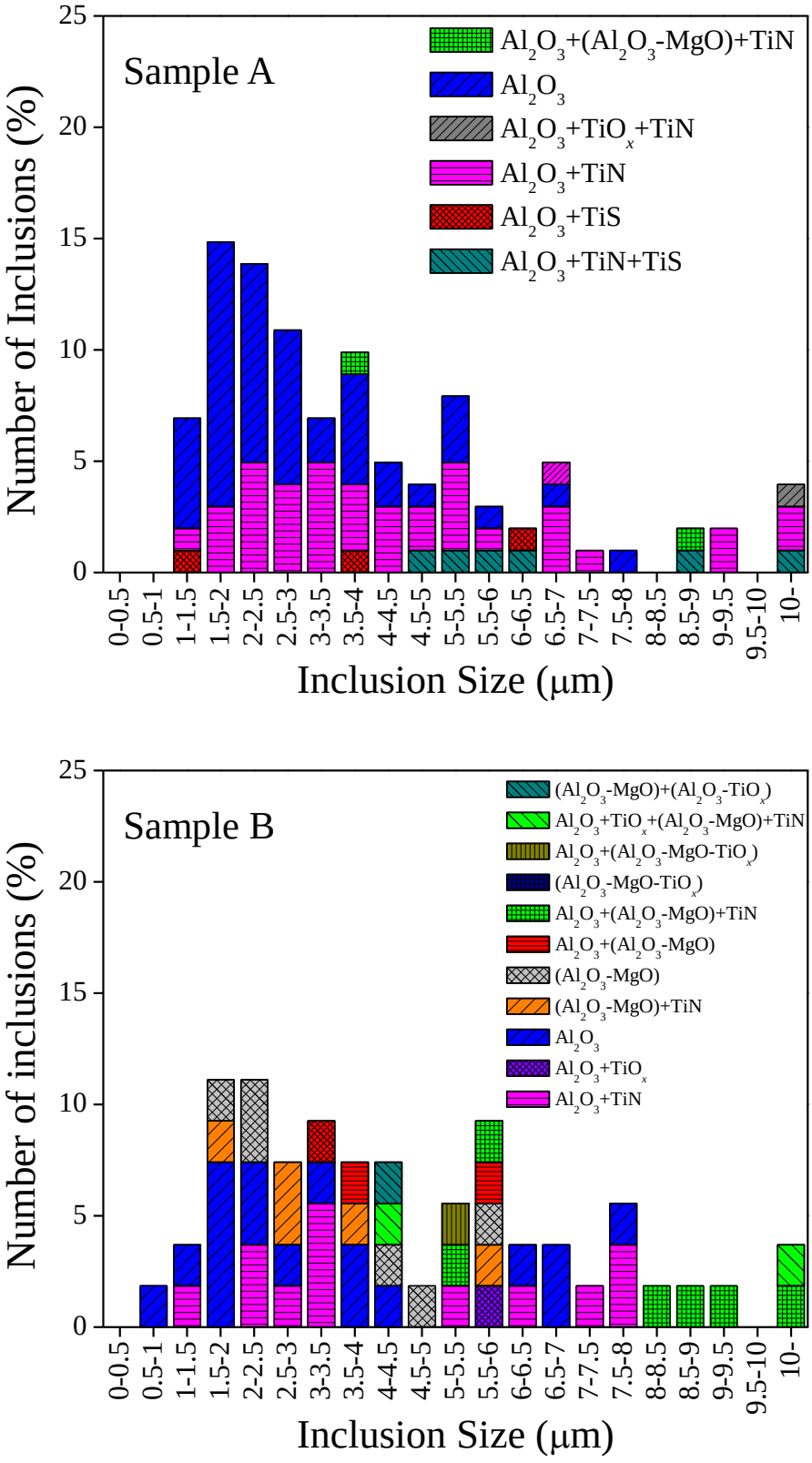

Figure 2-15. Size distribution of inclusions in the "Area 1" of samples A and B.

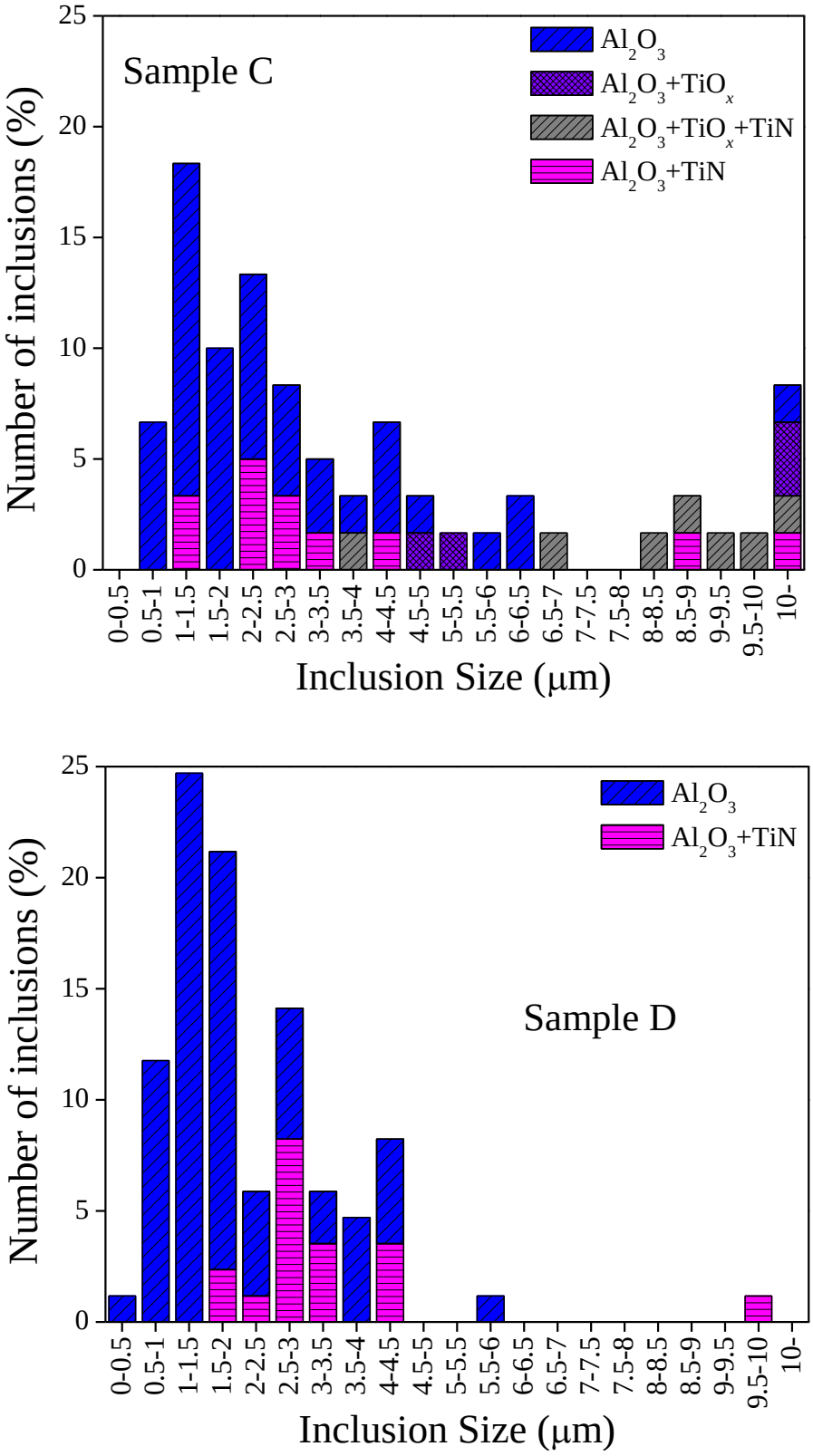

Figure 2-16. Size distribution of inclusions in the "Area 1" of samples C and D.

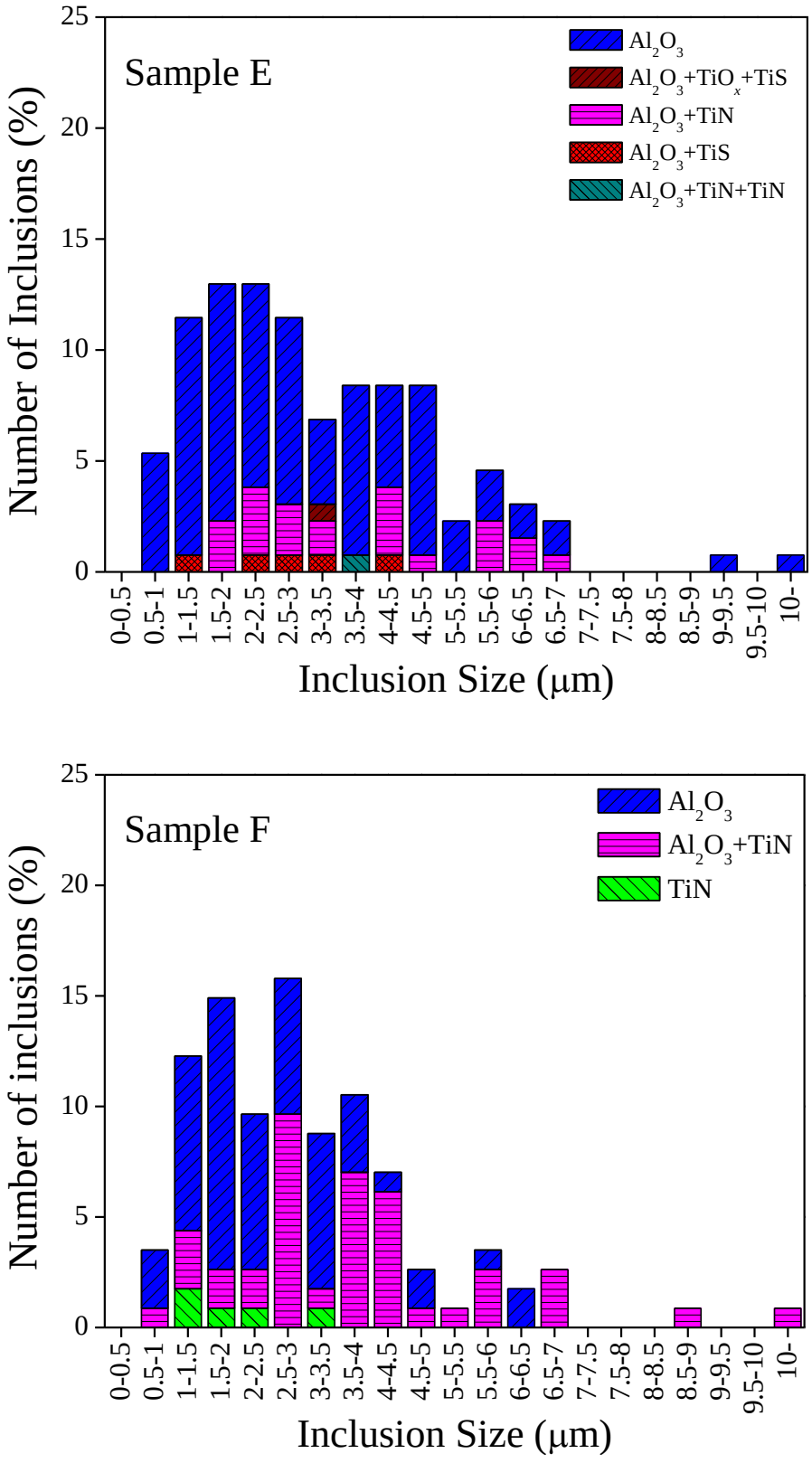

Figure 2-17. Size distribution of inclusions in the "Area 1" of samples E and F.

In the case of “Area 2”, average size of multi-phase inclusions in the samples A and B was 5.0 and 3.2 μm, respectively. Size of multi-phase inclusions in the “Area 2” was almost similar with that of multi-phase oxide inclusions in the “Area 1”. Size of Al_2O_3-TiO_x inclusions in the “Area 2” was around 1 μm in the samples A and B as shown in **Table 2-8**.

Table 2-8. Average size of the observed inclusions in the “Area 1” of samples A and B

. (μm)

Inclusion type	Sample name	
	A	**B**
Multi-phase inclusions	5.0	3.2
Small Al_2O_3-TiO_x	0.6	1.1

Figure 2-18 shows size of small Al_2O_3-TiO_x inclusions with distance from MgO crucible. **Figure 2-19** shows SEM image of Al_2O_3-TiO_x inclusions in the “Area 2” of samples A and B. As shown in **Figs. 2-18 and 2-19**, size of Al_2O_3-TiO_x inclusions in both samples increased with increasing distance from crucible increases.

From these results, the formation mechanism of small Al_2O_3-TiO_x inclusions in the samples A and B can be explained as follows. If Al_2O_3-TiO_x inclusions were formed at deoxidation step before solidification, size of Al_2O_3-TiO_x inclusions near the crucible wall would be much larger. However, completely opposite result was obtained. The occurring of size distribution of Al_2O_3-TiO_x inclusions with distance can be explained by extremely small difference of cooling speed even if the distance was just less than 200 μm. Cooling speed was fast at outer layer of melt. As a result, time was not enough to grow Al_2O_3-TiO_x inclusions at near crucible.

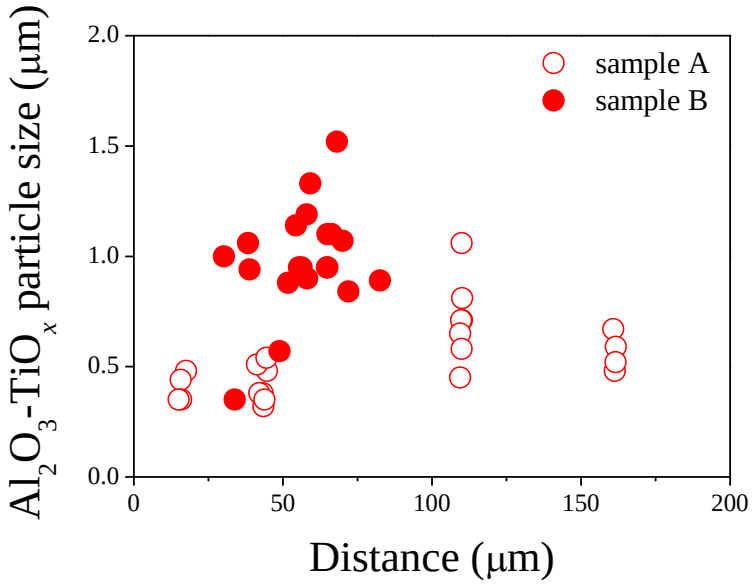

Figure 2-18. Al_2O_3-TiO_x particle size with distance in samples A and B.

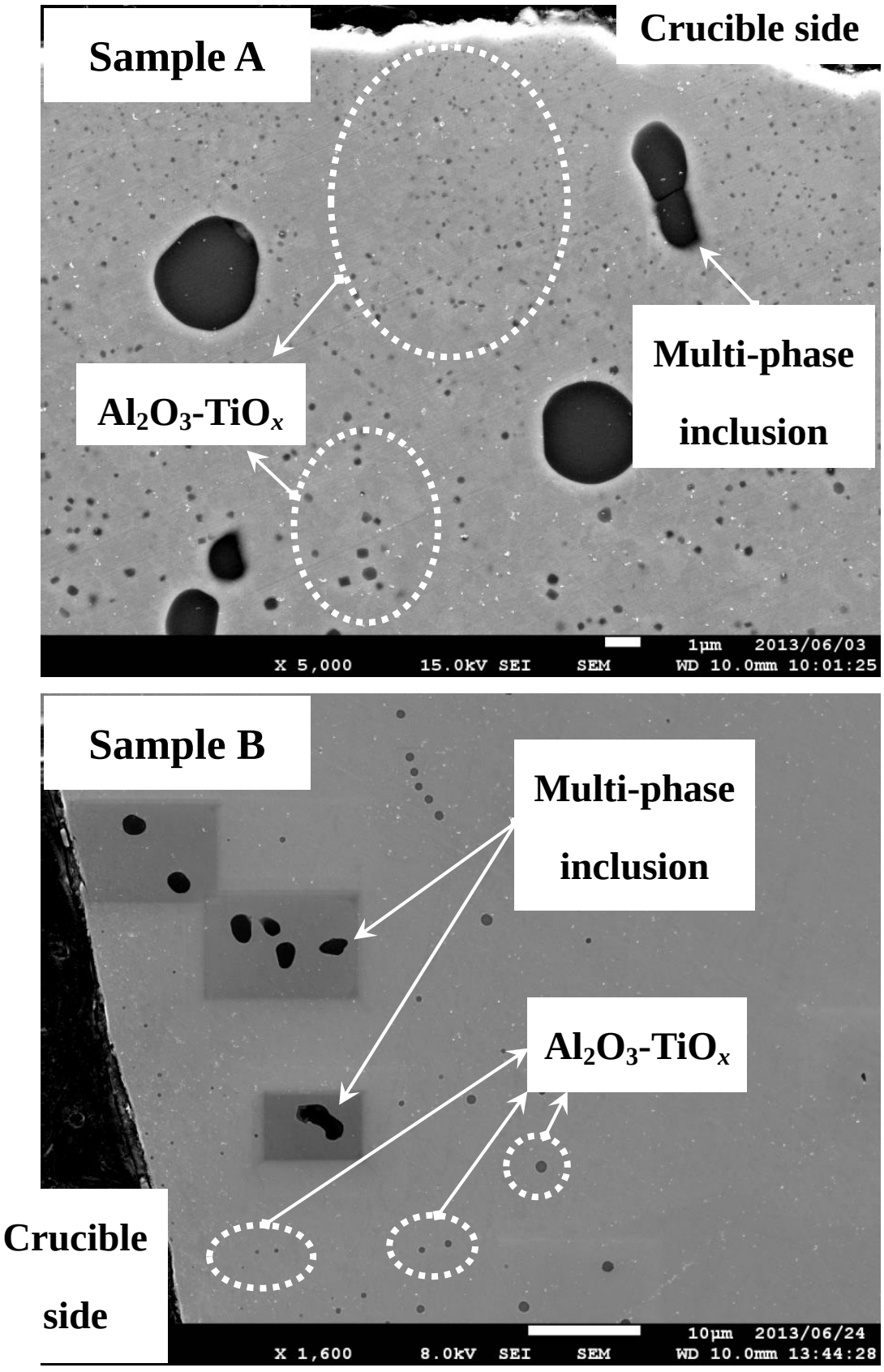

Figure 2-19. SEM image of "Area 2" in samples A and B.

2.3.2.3 Comparison of 2-demension and 3-demension analyses

In order to identify advantage for using 3-demension analysis, 3D analysis was carried out just outer layer of sample A. Average size of inclusions in the "Area 2" by using 3D analysis shown in **Table 2-9**. The average size of Al_2O_3-TiO_x inclusions was almost same with that by using 2D analysis. However, in the case of multi-phase inclusions, big difference was observed between two kinds of analysis.

Table 2-9. Average size of the observed inclusions in the "Area 2" of sample A by using 3D analysis method.

(μm)

Inclusion type	Sample name
	A
Multi-phase inclusions	18.2
Small Al_2O_3-TiO_x	0.8

In addition, the average size of inclusions in the "Area 1" by 3D analysis was 4.7 μm. The obtained average size of all inclusions in the "Area 1" by 2D analysis was 6.4 μm as shown in **Table 2-7** in Sec. 2.3.2.2. In fact, although the size of inclusion which detected by using 3D analysis would be original size of inclusions because the surrounding Fe matrix was excluded by etching, the measured size of inclusions in "Area 1", which observed in all samples, by using 2D and 3D analysis methods was almost similar in present study.

Figure 2-20 shows the comparison of results of composition analysis of Al_2O_3-TiO_x inclusions by using 2D and 3D analysis methods. As shown in **Fig. 2-20**, there was no difference between two results. **Figure 2-21** shows the result of mapping analysis by using 3D analysis method. As shown in **Fig. 2-21**, there was no detectable area in which phase of inclusion could not be determined by using EDS. Consequently, 3D analysis method was same or worse for analysis of chemical composition of

inclusions.

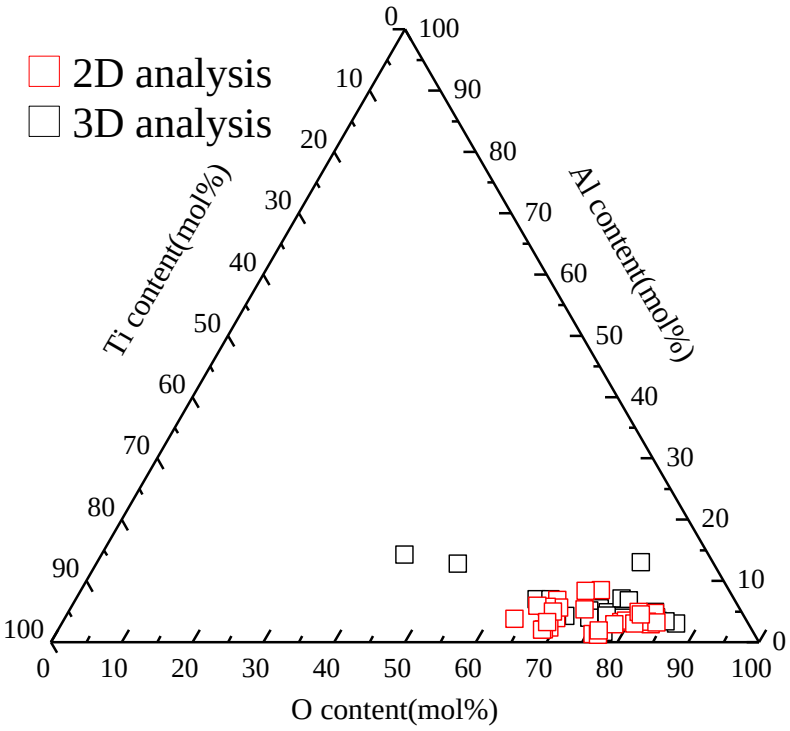

Figure 2-20. Chemical composition of Al_2O_3-TiO_x inclusions by using 2D and 3D analysis methods.

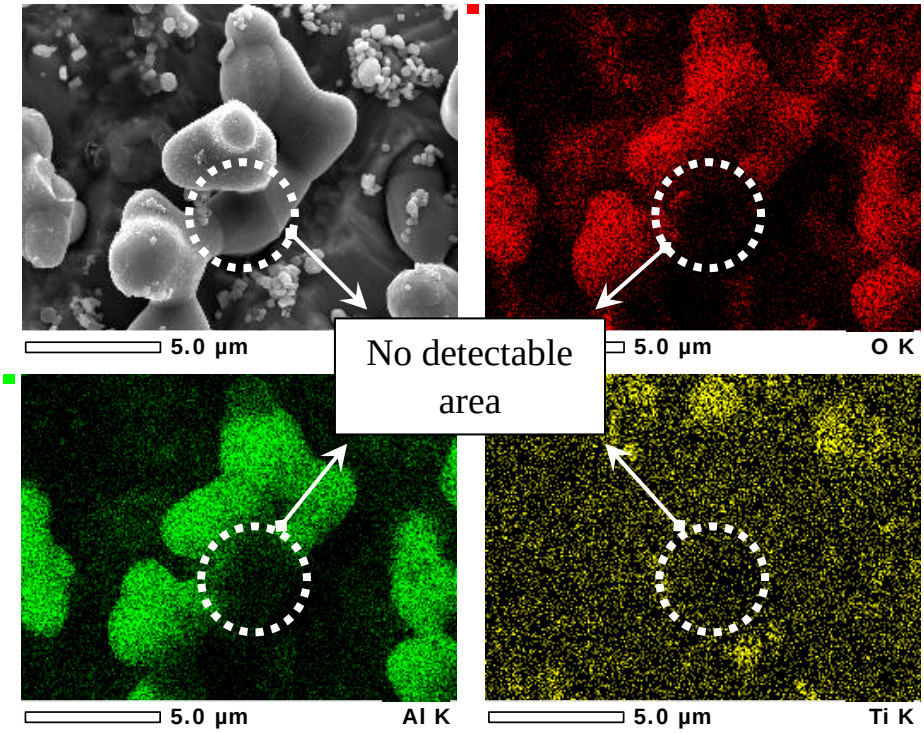

Figure 2-21. EDS mapping image of multi-phase inclusion in the "Area 2" of sample A.

2.3.3. Inner layer

2.3.3.1 Type and composition of inclusions in inner layer

TiN and/or TiS based inclusions were mainly observed in the inner layer. TiN and TiS were formed during solidification as mentioned in Sec. 2.3.2.1. The type of inclusions in the inner layer of all samples is shown in **Figure 2-22**. In the sample A, numerous TiS based inclusions were observed. The formation of TiS in the sample A was explained by considering of the product of the sulfur and titanium activities in Sec. 2.3.2.1. In the case of sample B, Al_2O_3-MgO based inclusions were detected approximately 30%. Al_2O_3-MgO based inclusions were usually observed in outer layer and it was also expounded in Sec. 2.3.2.1 by using Mg-Al-O diagram.

In the inner layer, mostly TiN and Al_2O_3+TiN, and some Al_2O_3 and Al_2O_3+TiO_x inclusions were observed in the samples C and E. In the case of samples D and F, TiN inclusions were mainly observed and some Al_2O_3 and Al_2O_3+TiN inclusions were also detected. Inclusions consist of just oxide were maximum 9.4% in the sample C.

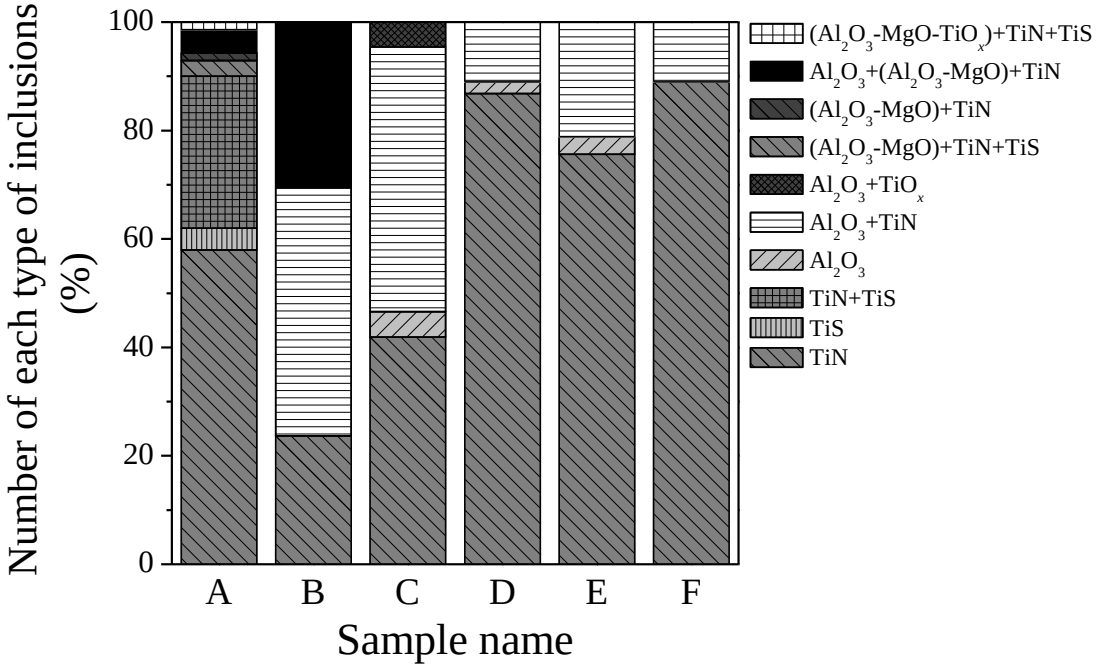

Figure 2-22. Observed inclusion types in inner layer of all samples.

2.3.3.2 Size of inclusions in inner layer

Average size of the observed inclusions in the inner layer of all samples was shown in **Table 2-10**. The average size of TiN and TiS single particles was around 1μm. And, the average size of the observed oxide based inclusions in inner layer was smaller than that in the outer layer. It can be explained that big oxide inclusions were moved to outside of melt by stirring force. Therefore, small inclusions were remained inside of melt.

Table 2-10. Average size of the observed inclusions in the inner layer of all samples. (μm)

Inclusion type	Sample name					
	A	**B**	**C**	**D**	**E**	**F**
TiN	1.0	0.6	0.4	0.9	1.0	1.1
TiS	0.4	-	-	-	-	-
TiN+TiS	1.3	-	-	-	-	-
Al_2O_3	-	-	1.9	2.4	2.2	-
Al_2O_3+TiN	-	1.5	1.1	2.5	2.9	3.9
(Al_2O_3-MgO)+TiN	4.1	2.6	-	-	-	-
(Al_2O_3-MgO)+TiN+TiS	0.7	-	-	-	-	-
Al_2O_3+(Al_2O_3-MgO)+TiN	2.9	-	-	-	-	-
(Al_2O_3-MgO-TiO_x)+TiN+TiS	2.1	-	-	-	-	-
Al_2O_3+TiO_x	-	-	1.4	-	-	-

- : not detected

Size distribution of inclusions in the inner layer of all samples was shown in **Figs 2-23, 2-24 and 2-25**. The number of observed inclusions in the inner layer of samples A, B, C, D, E and F was 69, 59, 43, 91, 90 and 109, respectively.

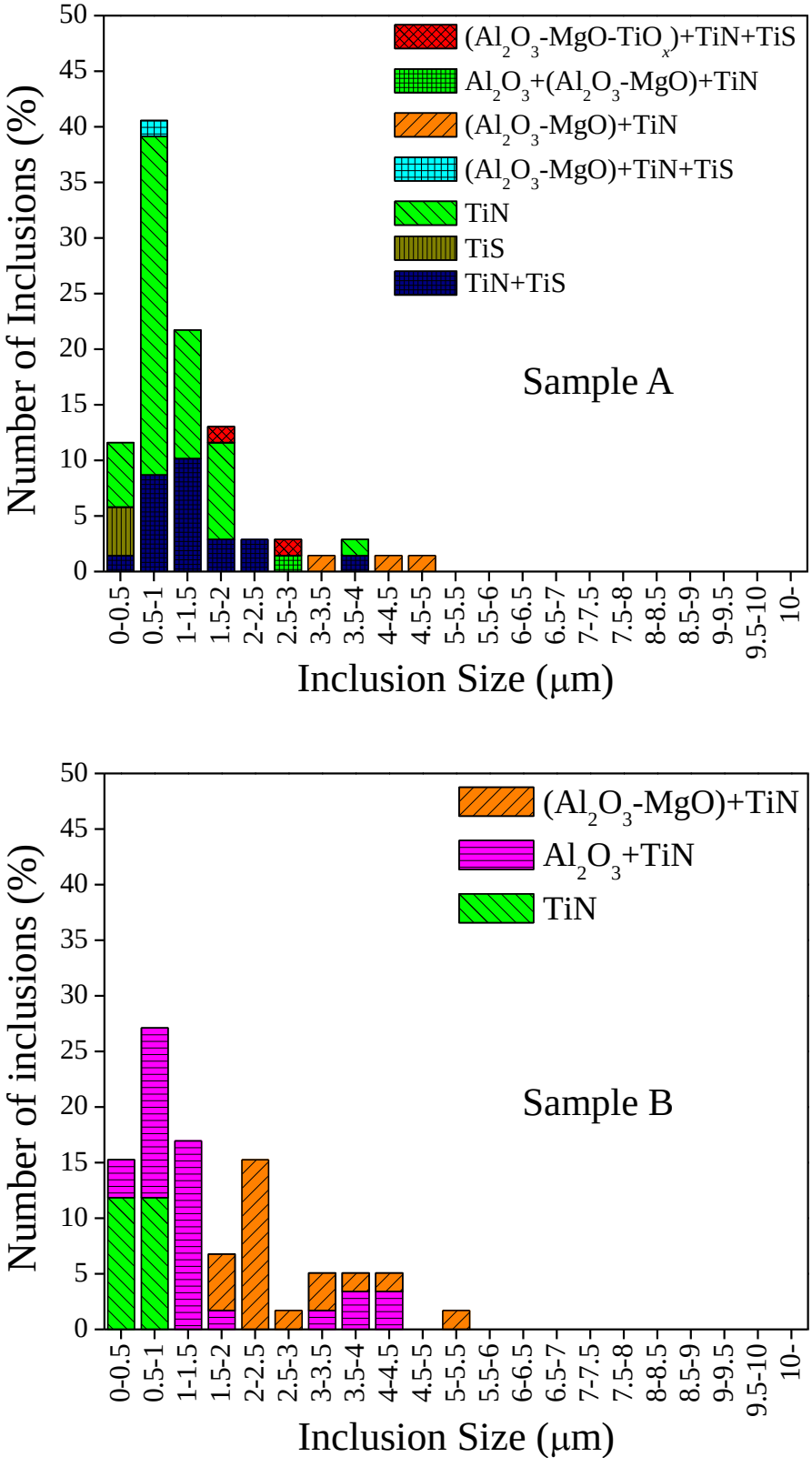

Figure 2-23. Size distribution of inclusions in the inner layer of samples A and B.

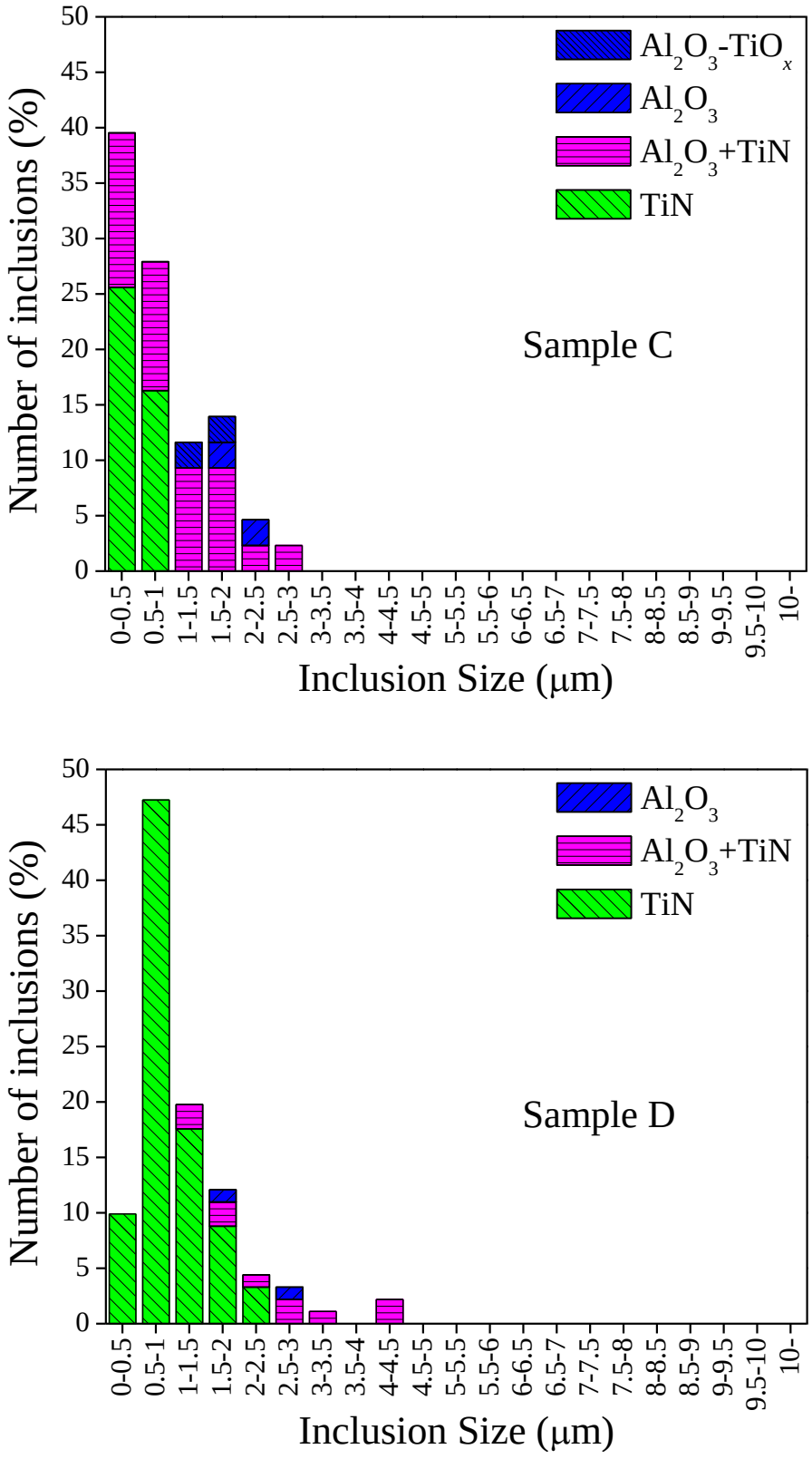

Figure 2-24. Size distribution of inclusions in the inner layer of samples C and D.

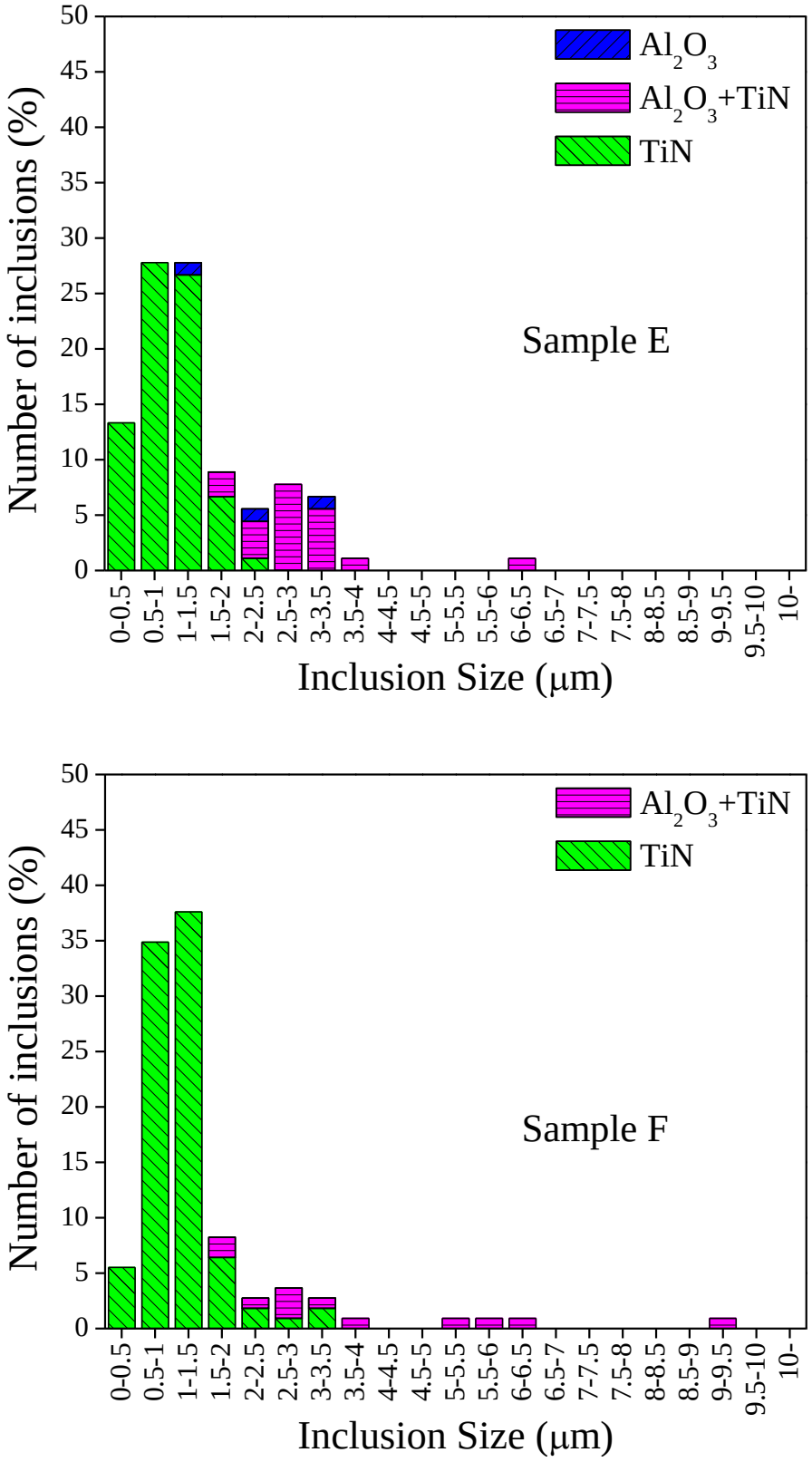

Figure 2-25. Size distribution of inclusions in the inner layer of samples E and F.

2.3.3.3 Shape of inclusions in inner layer

In the inner layer, morphological characteristic was observed. TiN phases were almost polyhedral type and TiS phases were mainly roundish type. **Figure 2-26** shows typical morphology of TiN and/or TiS inclusions in the inner layer. Polyhedral type of inclusion consisted of one phase. Irregular type of inclusion was composed of two phase. Inclusion which consists of more than three phases was judged as cluster type.

On the other hand, oxide+(TiN and/or TiS) inclusions were polyhedral and irregular types. **Figure 2-27** shows typical morphology of oxide based inclusions in the inner layer. Polyhedral type of oxide+(TiN and/or TiS) inclusion was the two or three phase inclusions in which TiN and/or TiS phase covered all oxide surface. In the case of irregular type, TiN and/or TiS also covered but not all surface.

Table 2-11 shows fraction of the number of each morphological type of inclusions in the inner layer of all samples with two types of inclusions, i.e. TiN and/or TiS inclusion and oxide+(TiN and/or TiS) inclusion. Over 78% of polyhedral type of TiN and/or TiS inclusions was observed in the samples B, C, D, E and F. In the case of sample A, irregular type of TiN and/or TiS inclusions was 42% approximately. Almost irregular type of TiN and/or TiS inclusion was TiN+TiS in the sample A. In addition, roundish type of TiN and/or TiS inclusion also often detected in the inner layer of sample A. Roundish type of TiN and/or TiS inclusion was TiS inclusion.

On the other hand, the fraction of the number of polyhedral type of oxide+(TiN and/or TiS) inclusions was 86% at maximum.

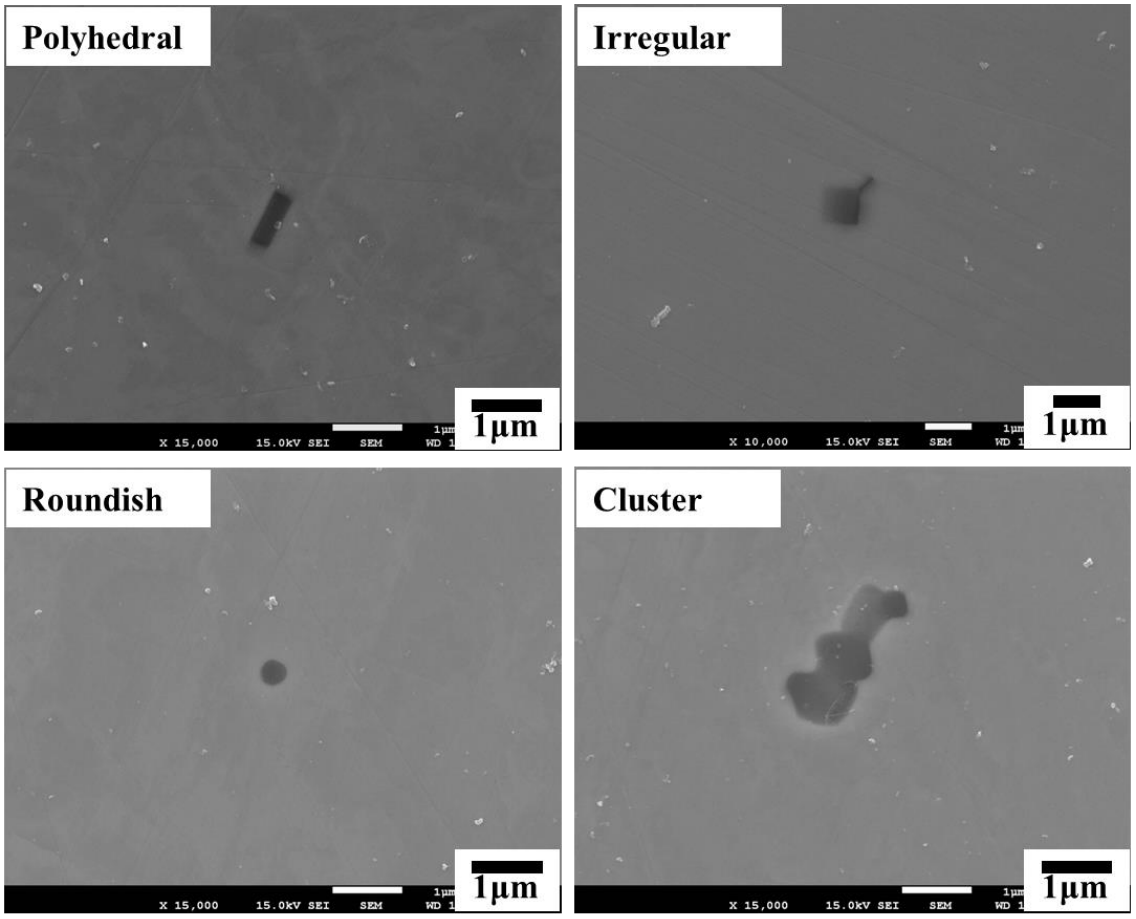

Figure 2-26. Typical morphology of TiN and/or TiS inclusions in the inner layer.

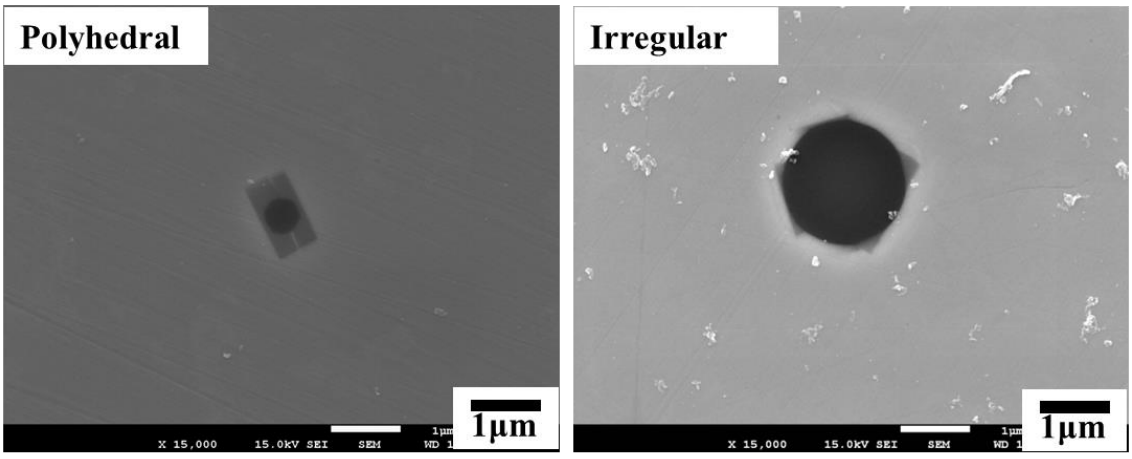

Figure 2-27. Typical morphology of oxide based inclusions in the inner layer.

Table 2-11. Type of the observed inclusions in the inner layer of all samples. (%)

Sample name	TiN and/or TiS inclusion				Oxide+(TiN and/or TiS) inclusion	
	Polyhedral	Irregular	Cluster	Roundish	Polyhedral	Irregular
A	45	42	3	10	86	14
B	93	7	-	-	46	54
C	94	6	-	-	71	29
D	82	18	-	-	30	70
E	82	18	-	-	16	84
F	78	22	-	-	33	67

- : not detected

2.3.4 Effect of nitrogen on the formation of inclusions

In the samples C, D, E and F, effects of nitrogen content in the melt on the inclusion characteristics were observed.

In the outer layer, as mentioned in **Figs. 2-13** and **2-14** in Sec. 2.3.2.1., in the samples C and E with relatively small nitrogen contents, some (Al_2O_3+TiO_x)-based inclusions were observed. On the other hand, in the case of samples D and F, (Al_2O_3+TiO_x)-based inclusions were not detected. These different tendencies would be due to the strong interaction between solute Ti and N in the alloy and decreased Ti activity.

In the inner layer, as shown in **Fig. 2-22** in Sec. 2.3.3.1., the fraction of the number of TiN single-phase particles in samples C and E containing 0.0005 and 0.0013 mass%N was 42 and 76 % of observed inclusions, respectively. On the contrary, in the case of samples D and F, the fraction of the number of TiN inclusions was more than 87 % of total inclusions. The increase in N content of the alloy resulted in the increase of the number of independently precipitated TiN single phase

particles.

As shown in **Table 2-11** in the Sec. 2.3.3.3, fraction of the number of irregular type of TiN and/or TiS inclusions in the samples D and F was much larger than that in the samples C and E with the same content of Al. The observed irregular type of TiN and/or TiS inclusions in the samples C, D, E and F were composed of only two TiN phases but not TiS. From this result, it can be considered that TiN particles were more easily formed at high nitrogen content during solidification.

Figures 2-28 and **2-29** show the size distribution of TiN single phase particles in the inner layer at similar metal composition with different nitrogen content. The size of TiN single phase particles in sample D (0.0058 mass%N) is much larger than that in sample C (0.0005 mass%N). In the case of samples E and F, the same phenomenon was observed. This tendency indicates that the formation of larger TiN inclusions easily happened in the sample with larger nitrogen content than smaller nitrogen content during quenching.

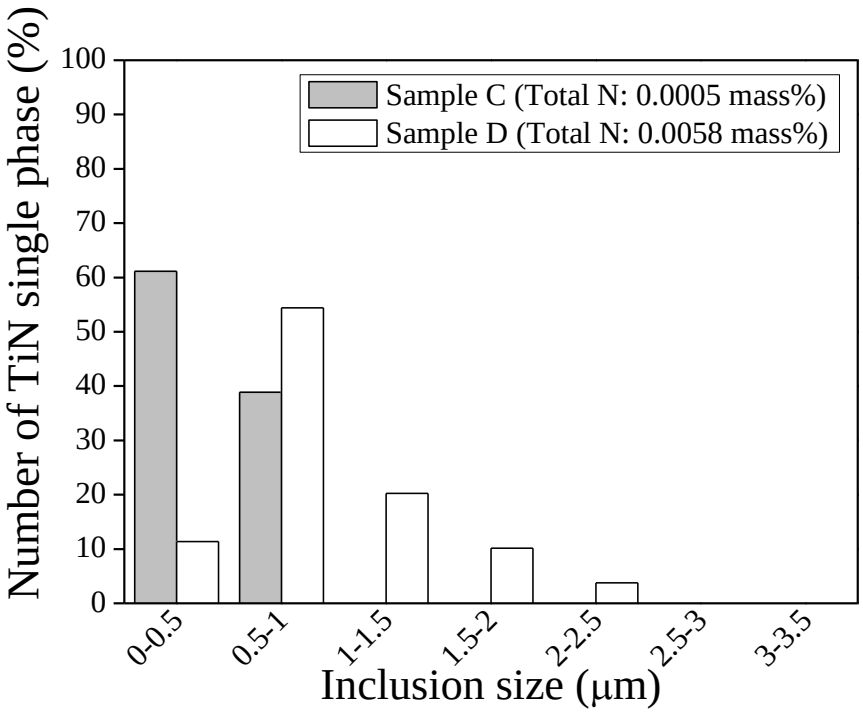

Figure 2-28. Size distribution of the observed TiN inclusions in inner layer of samples C and D.

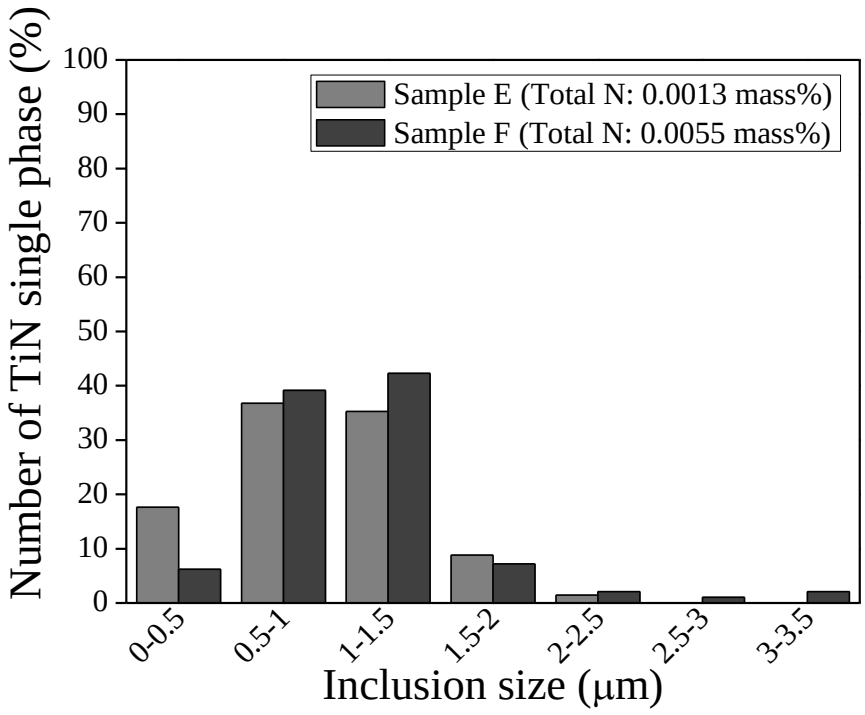

Figure 2-29. Size distribution of the observed TiN inclusions in inner layer of samples E and F.

2.4 Summary

In this chapter, the morphology of formed inclusions during deoxidation at 1873 K and solidification has been observed with several metal compositions, holding times and crucibles. The formation process of oxide, nitride, sulfide and complex phase inclusions was clarified based on calculation of thermodynamic data and measurement of inclusion characteristics such as size, morphology and composition.

MgO crucible dissolved depending on titanium concentration in the melt and it resulted in the formation of “Area 2” in the outer layer. Equilibrium oxide corresponded to the Al-Ti-O stable oxide phase diagram and the transient oxide inclusions, especially Al_2O_3+TiO_x inclusions in samples C and E, were also observed. TiN and/or TiS based inclusions which formed during solidification were observed and fraction of the number and size increased with increasing nitrogen content in the inner layer.

References

[1] H. Matsuura, K. Nakase and F. Tsukihashi: *CAMP-ISIJ*, **23**(2010), 956.

[2] S.K. Jo, B. Song and S.H. Kim: *Metall. Mater. Trans. B*, **33B**(2002), pp. 703-709.

[3] J.D. Seo and S.H. Kim: *Steel Res.*, **71**(2000), pp. 101-106.

[4] M. Hino and K. Ito ed.: THERMODYNAMIC DATA FOR STEELMAKING, Tohoku university press, Sendai, (2010), pp. 42, 236, 255 and 259.

[5] W.Y Kim, J.O. Jo, C.O. Lee, D.S. Kim and J.J. Pak: *ISIJ Int.*, **48**(2008), pp. 17-22.

Chapter 3. Change behavior of inclusions in Fe-Al-Ti-O-N alloy at 1473 K

3.1 Experimental procedure

In order to observe the evolution of various types of inclusions in solid state alloy, the prepared Fe-Al-Ti-O-N alloy samples were heated at 1473 K with or without ampoule.

In the case of samples A and B, heating experiment was carried out as following steps. A piece of sample (13 mm radius, thickness 5 mm) was machined from each sample and hanged in the reaction tube of an electric furnace by steel wire. Then, samples were heated at 1473 K for 3 hours and the atmosphere was replaced by high purity Ar gas (purity 99.9 %, flow rate: about 500 cm^3/min). After prescribed heating time, the samples were quickly taken out of the reaction tube and quenched by immersing into water. The shape of sample piece and experimental installation was shown in **Fig. 3-1**.

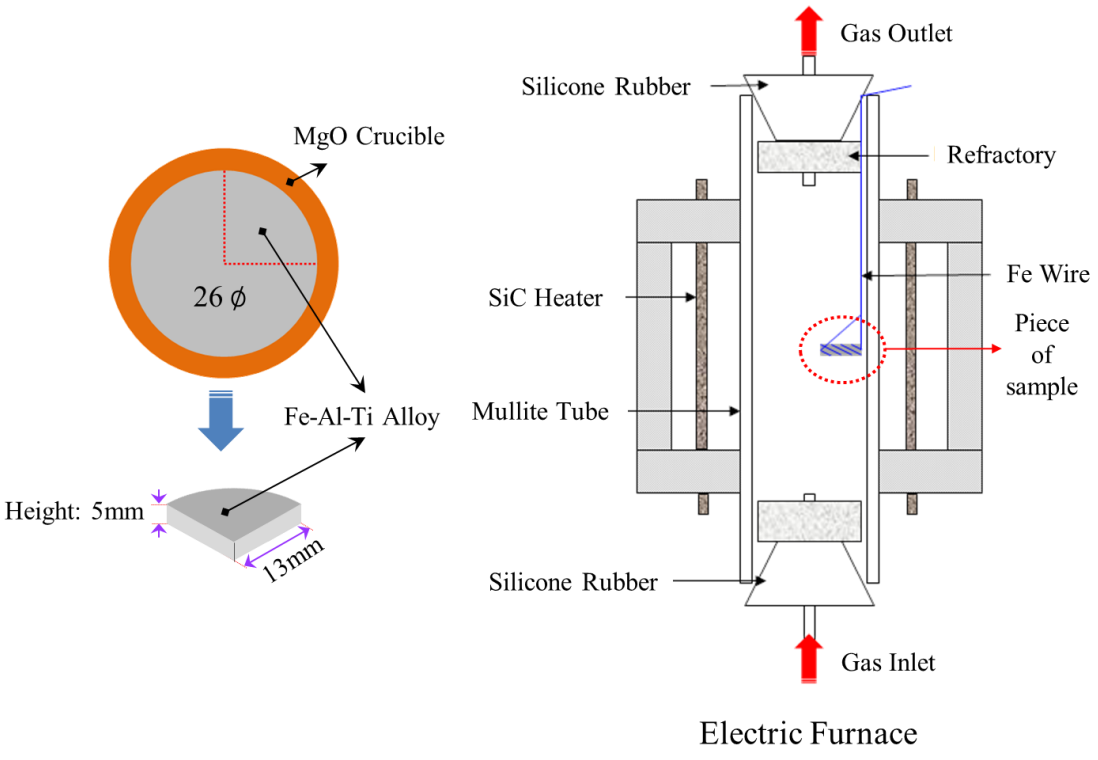

Figure 3-1. Sketch of sample piece and experimental installation.

In the case of other four kinds of Fe-Al-Ti-O-N samples, procedure of heating experiment was as follows. A cylindrical piece of the alloy (24 mm diameter, height: from 13 to 15 mm) was machined from the produced alloy and the piece was encapsulated into a low carbon steel ampoule (O.D.: 32 mm, I.D.: 24 mm, height: 20 mm) by Ar arc-welding at high purity Ar atmosphere of approximately 0.5 atm for the inhibition of oxidation of sample. The pictures of ampoule before and after welding and sectional view of ampoule were shown in **Fig. 3-2**. The welded ampoule was then heated at 1473 K which is normal heat treatment temperature for 3 hours in an electric furnace. The sketch of experimental installation was shown in **Fig. 3-3**. And then, the ampoule was quenched by immersing into water. The sample before and after heating at 1473 K was shown in **Fig. 3-4**. As shown in **Fig. 3-4**, the sample piece was not oxidized.

The inclusions in the heated samples were analyzed by using FE-SEM and EDS. The analysis method of inclusions in the the heated samples was the same as that for as cast samples as mentioned in Sec. 2.2.2.2.

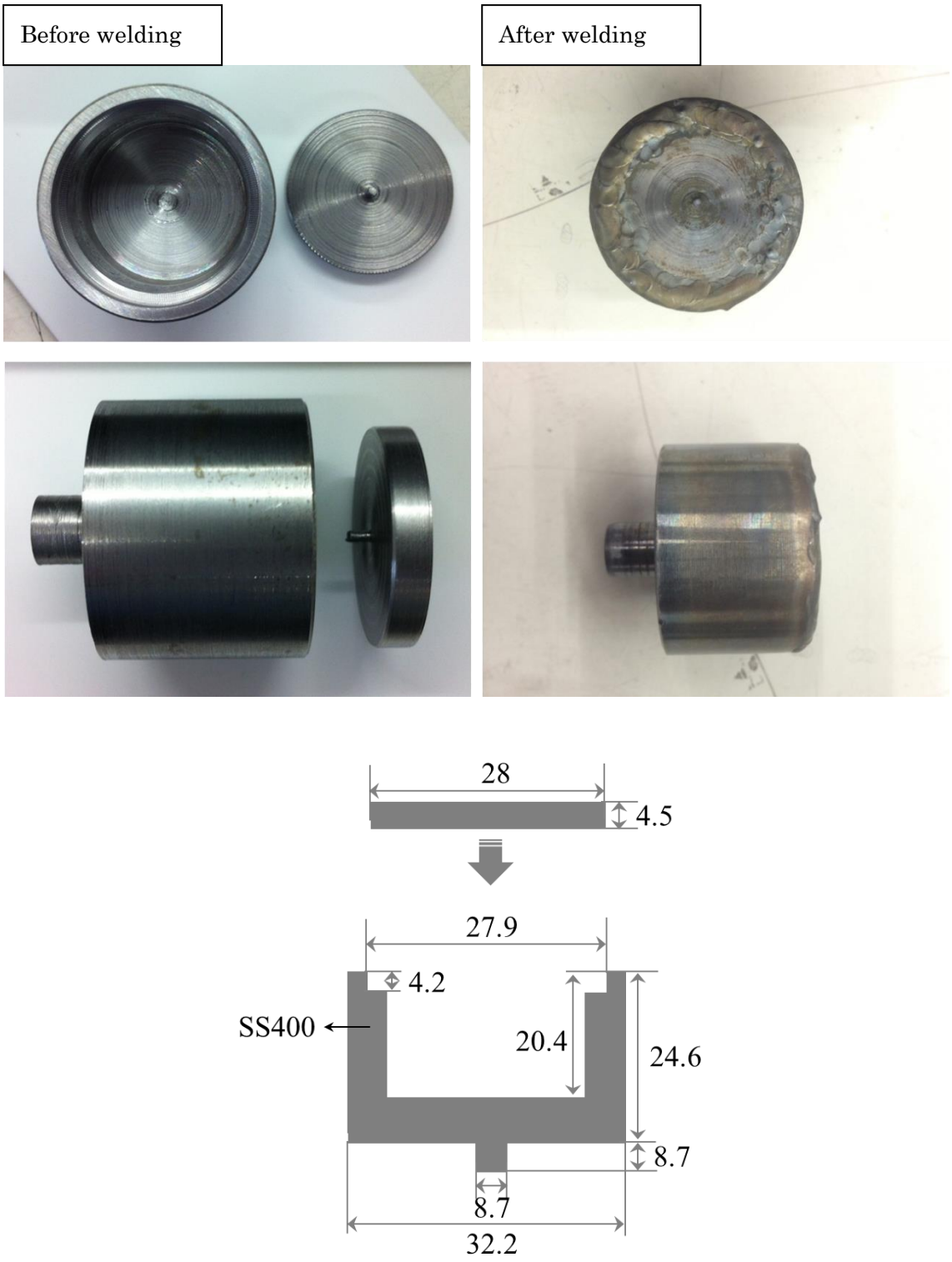

Figure 3-2. Picture and sectional view of ampoule.

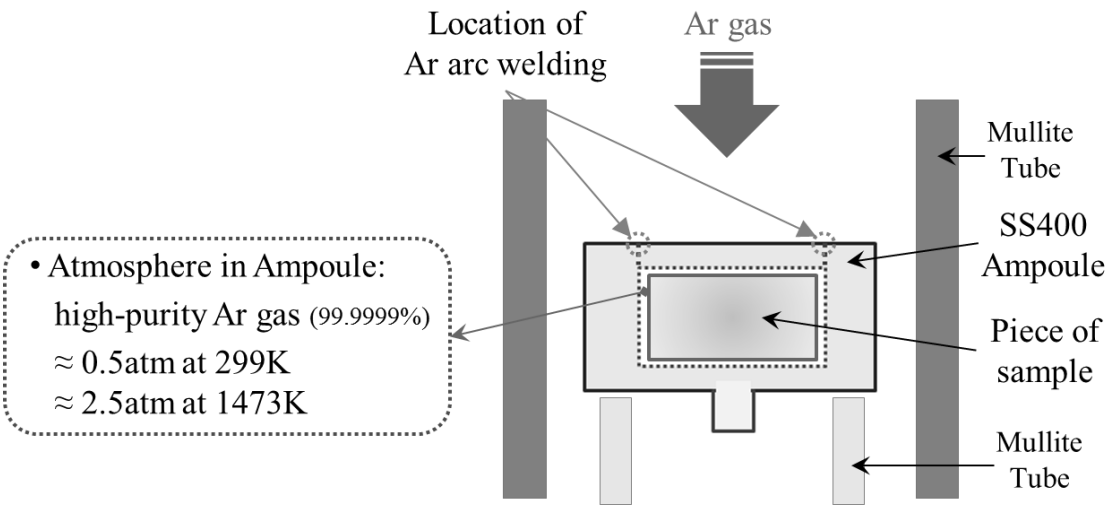

Figure 3-3. Sketch of experimental installation for using ampoule.

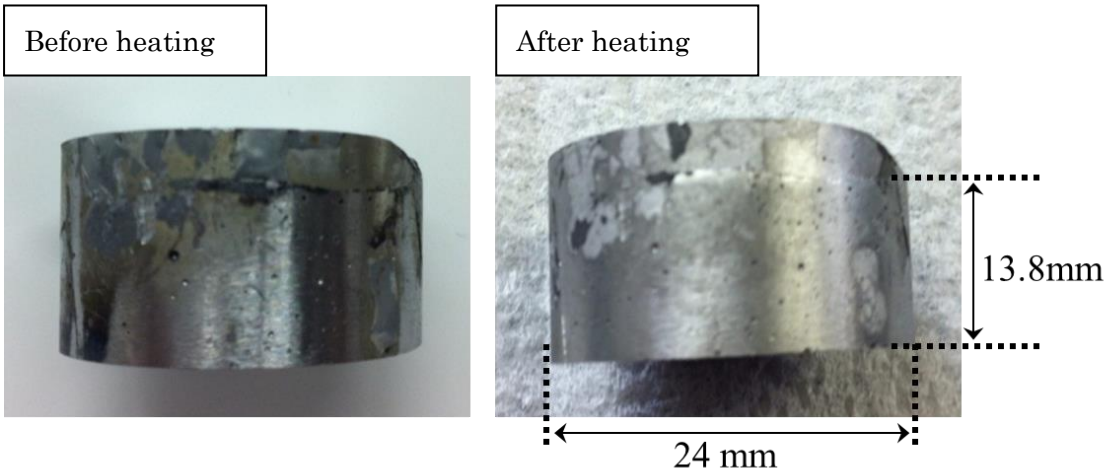

Figure 3-4. Picture of sample C before and after heating at 1473K.

3.2 Results and discussion

3.2.1 Protecting samples from oxygen during heating

The clarification that the samples were not oxidized during heating was quite important. The analysis of oxygen content in the samples A and C was carried out with different heating experiment methods representatively as shown in **Table 3-1**. The oxygen content in the samples A and C did not change drastically by heating. From these results, it is concluded that the samples were not oxidized during heating at 1473 K for 3 hours.

Table 3-1. Oxygen content before and after heating. (mass%)

	A	B	C	D	E	F
Before heating	0.0006	0.0060	0.0005	0.0007	0.0012	0.0010
After heating	0.0014	-	0.0008	-	-	-

- : not analyzed

3.2.1.1 Fe content with distance

No oxidation of the samples A and B could be also clarified by inclusion composition near the surface of sample. **Figure 3-5** shows Fe content with distance in as cast and heated samples. In the case of sample A, black and red lines mean change of Fe content for each type of inclusions in the as cast sample A. Fe content in the inclusions except small Al_2O_3-TiO_x had almost the same tendency with distance before and after heating. If oxygen was provided from gas into the samples, Fe in metal phase would be oxidized and Fe content should be increased. However, this kind of behavior was not observed. Therefore, oxidation of sample did not occur. Fe content in the small Al_2O_3-TiO_x inclusions was reduced due to size increasing of inclusions. In the case of the sample B, Fe content

in the inclusions did not change by heating.

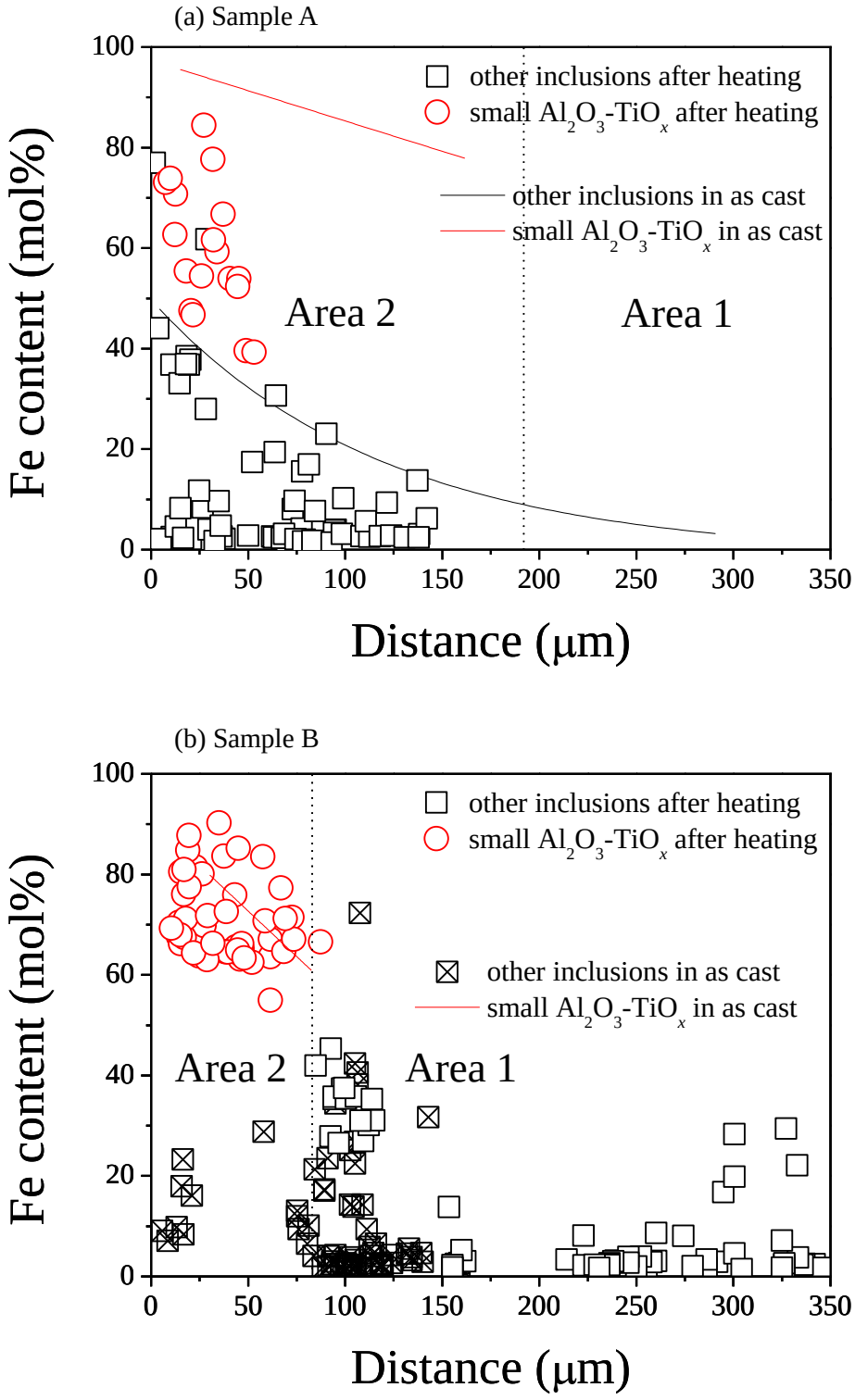

Figure 3-5. Change of Fe content with distance in the samples (a) A and (b) B before and after heating.

3.2.2 Change behavior of inclusions in outer layer of samples A and B by heating

3.2.2.1 Type and compositional change of inclusions

Table 3-2 shows the change of ratio of inclusion types by heating in the "Area 1" of outer layer of the samples A and B. "+*x*" means of the increase the ratio of inclusion types by heating. "-*x*" describes the decrease of the ratio of each inclusion type by heating.

As shown in **Table 3-2**, the number of TiO_x based inclusions increased by heating in the "Area 1" of the sample A. Furthermore, Al_2O_3+TiO_x and Al_2O_3+TiO_x+(Al_2O_3-TiO_x)+TiN inclusions were just observed in the heated sample. And, the some MgO based inclusions existed in the as cast were not detected after heating. These phenomena can be certainly observed in the **Fig. 3-6**. The observed inclusions can be described as small Al_2O_3-TiO_x, Al_2O_3, -MgO, +TiS, +TiN, -TiO_x and +TiO_x. Here the complex inclusions were counted repeatedly by classifying with its type. For example, (Al_2O_3-MgO)+TiS+TiN inclusion was represented as -MgO, +TiS and +TiN, simultaneously. Although inclusions were not analyzed in the area of the distance more than 300 μm in the as cast sample A and distance range from 150 to 550 μm in the heated sample A, many inclusions were in there. As shown in **Fig. 3-6**, TiO_x based inclusions can be detected in the heated sample A. Furthermore, TiN and TiS based inclusions were observed in the "Area 1" of the heated sample A. In addition, MgO based inclusions were not detected anymore after heating. From these results, it is concluded that MgO based inclusion was not stable oxide at 1473 K.

In the case of sample B, notable changes of inclusion type were the drastic decrease in the ratio of MgO based inclusions and the sharp increase in the ratio of Al_2O_3 inclusions as shown in **Table 3-2**. As explained in Sec. 2.3.2.1, spinel inclusion ($MgAl_2O_4$) would be stable oxide in the sample B at 1873 K. However, it seems spinel like inclusion was no longer stable oxide in the sample B. From the change of fraction of inclusion types, stable oxide would be regarded as Al_2O_3 in the sample B at 1473 K.

Table 3-2. Observed inclusion types in "Area 1" of outer layer of the heated samples A and B

(%)

Inclusion type	Sample name	
	A	**B**
Al_2O_3	51(+2)	46(+15)
Al_2O_3+TiN	25(-14)	25(+3)
Al_2O_3+TiS	4(+1)	-
Al_2O_3+TiN+TiS	4(-2)	-
(Al_2O_3-MgO)	-	7(-4)
(Al_2O_3-MgO)+TiN	-	8(-1)
Al_2O_3+(Al_2O_3-MgO)	-	3(-1)
Al_2O_3+(Al_2O_3-MgO)+TiN	-(-2)	-(-11)
Al_2O_3+(Al_2O_3-MgO)+TiN+TiS	-(-1)	-
(Al_2O_3-MgO-TiO_x)	-	-(-2)
Al_2O_3+(Al_2O_3-MgO-TiO_x)	-	-(-4)
Al_2O_3+TiO_x	1(+1)	10(+8)
Al_2O_3+TiO_x+TiN	7(+6)	-
Al_2O_3+TiO_x+TiN+TiS	1(+1)	-
Al_2O_3+TiO_x+(Al_2O_3-MgO)+TiN	-	-(-2)
Al_2O_3+TiO_x+(Al_2O_3-TiO_x)+TiN	4(+4)	-
(Al_2O_3-MgO)+(Al_2O_3-TiO_x)	-	-(-2)

- : not detected

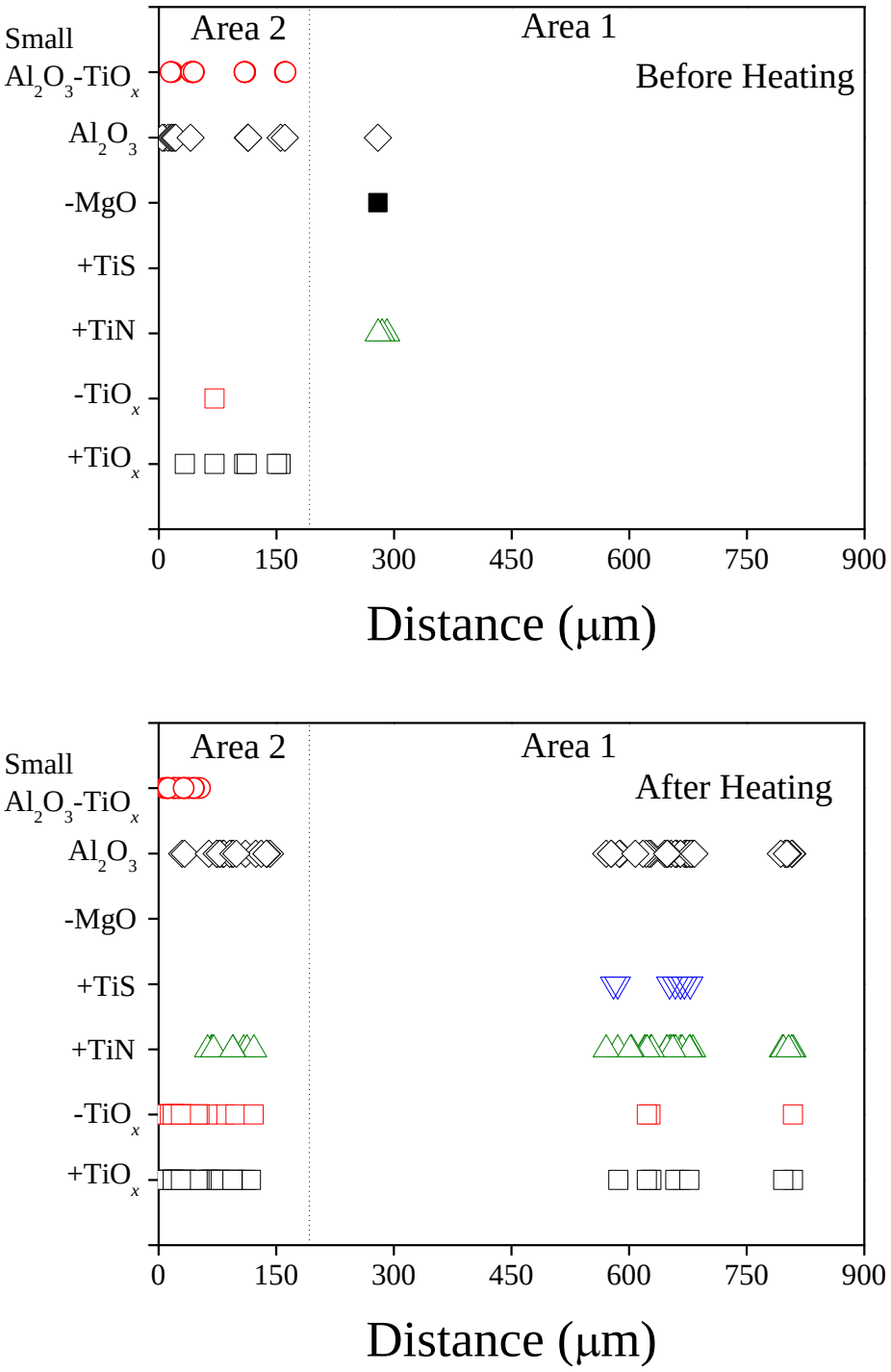

Figure 3-6. Change of inclusion types with distance in the sample A before and after heating.

In the case of the “Area 2” in the sample A, TiO_x based inclusions were more usually detected in the heated sample such as Al_2O_3-TiO_x and Al_2O_3+TiO_x. In **Fig. 3-6**, Al_2O_3-TiO_x and Al_2O_3+TiO_x were represented as -TiO_x and +TiO_x, respectively.

Composition of small Al_2O_3-TiO_x inclusions dispersed widely and the Al content as the Al-Ti binary system was between 5 and 32 mol%. The average composition of small Al_2O_3-TiO_x inclusions was shown in **Table 3-3**. Average Ti content in the small Al_2O_3-TiO_x inclusions increased by 4 mol% by heating.

Table 3-3. Average composition of small Al_2O_3-TiO_x in the samples A before and after heating.

(mol%)

	Before heating	After heating
Al	19	15
Ti	81	85

3.2.2.2 Mechanisms of compositional change of inclusions

As mentioned previously in Sec 3.2.2.1, number of the MgO based inclusions decreased by heating in outer layer of the samples A and B. Most Al_2O_3-MgO phase in the MgO based inclusions contained from 18 to 34 mol%Mg as the Al-Mg binary system. The Al_2O_3-MgO phase (average composition: 72 mol%Al-28 mol%Mg as the Al-Mg binary system) correspond to $MgAl_2O_4$ (spinel). Therefore, the dissolution of spinel inclusions expressed as **Eq. (3-1)** occurred and thus the fraction of spinel inclusions decreased by heating in the both samples A and B.

$$MgAl_2O_4(s) = \underline{Mg} + 2\underline{Al} + 4\underline{O} \quad (3\text{-}1)$$

In the case of sample A, simultaneously, TiO_x phase formed. Neither the valence of Ti nor the mineralogical phase of inclusions was measured, and the chemical stability of oxide phase in solid steel has not been reported. Therefore, the formed Ti oxide was represented as TiO_x.

Figure 3-7 shows a mapping analysis result of Al_2O_3+TiO_x+(Al_2O_3-TiO_x)+TiN in the sample A after heating. As shown in **Fig. 3-7**, an inclusion on the right consists three layers, i.e. Al_2O_3 core, Al-Ti-O middle layer and outermost TiO_x layer. From morphological result, it indicates that Al_2O_3 inclusion reacts with Ti from outside as Eq. (3-2). In addition, since such inclusions with completely separated Al_2O_3 core and TiO_x outer layer were also detected in the sample A after heating, the formation of TiO_x phase could be also considered as the result of precipitation of TiO_x on the Al_2O_3 inclusion. Therefore, formation of TiO_x phase can be expressed as both **Eqs. (3-2)** and **(3-3)**.

$$x Al_2O_3(s) + 3\underline{Ti} = 3TiO_x(s) + 2x\underline{Al} \quad (3\text{-}2)$$

$$\underline{Ti} + x\underline{O} = TiO_x(s) \quad (3\text{-}3)$$

On the contrary, according to the change of inclusion type by heating, Al_2O_3 inclusions were

formed in the sample B as **Eq. (3-4)**.

$$2\underline{Al} + 3\underline{O} = Al_2O_3(s) \quad (3\text{-}4)$$

The source of Al, Ti and O would be the dissolution of spinel inclusions. However, number of spinel inclusions is quite small in the sample A before heating. The change of number density of small Al_2O_3-TiO_x inclusions is shown in **Table 3-4** and **Fig 3-8**. The number of small Al_2O_3-TiO_x inclusion extremely decreased by heating. From this result, the dissolved small Al_2O_3-TiO_x inclusions provided Ti and O for TiO_x formation in the sample A.

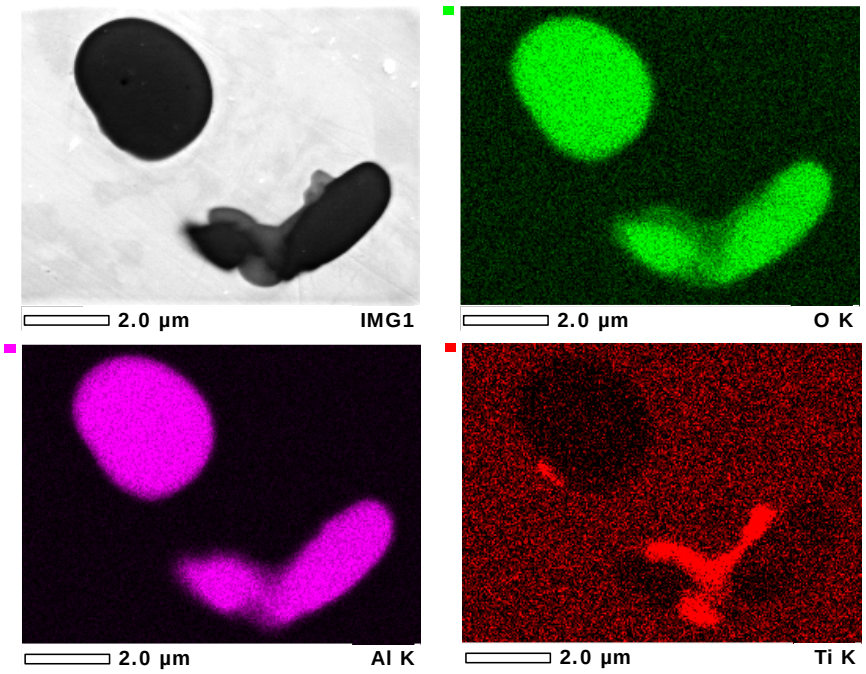

Figure 3-7. Mapping result of Al_2O_3+TiO_x+(Al_2O_3-TiO_x)+TiN in the sample A after heating.

Table 3-4. Number density of small Al_2O_3-TiO_x in the samples A before and after heating.

(number / mm^2)

	Before heating	After heating
Number distribution	170,000	7,000

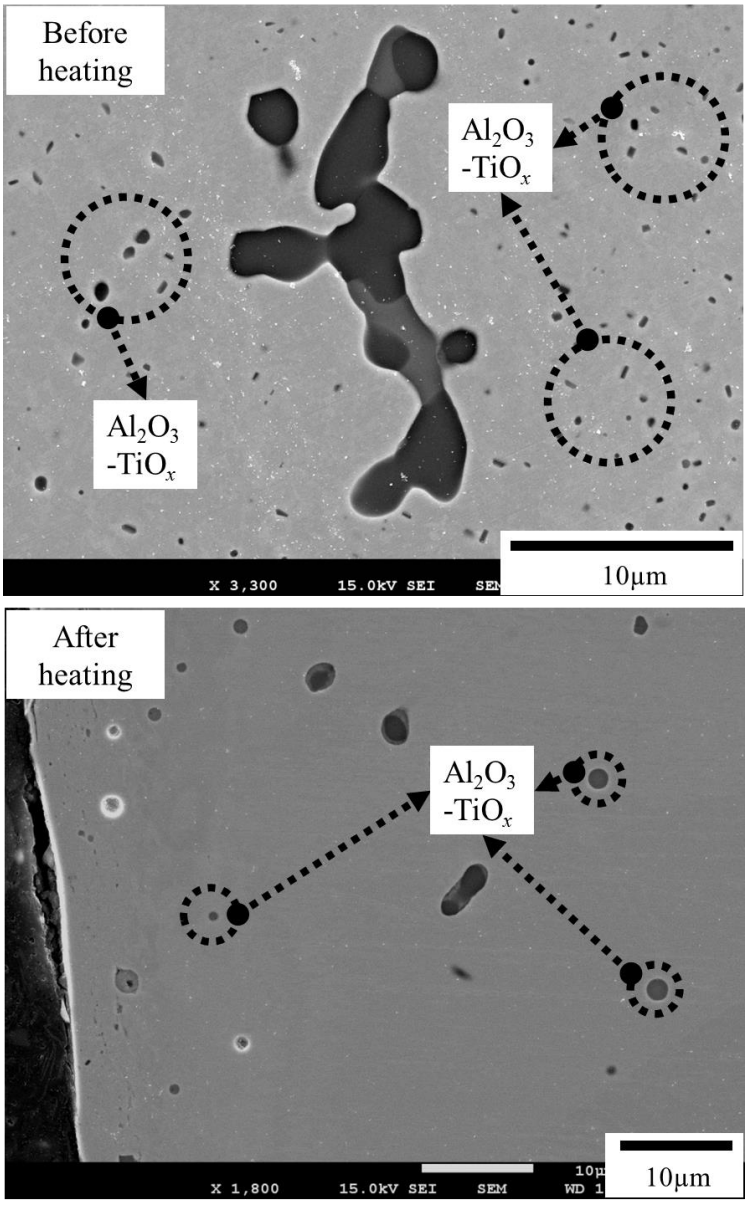

Figure 3-8. SEM image of small Al_2O_3-TiO_x in the sample A before and after heating.

3.2.2.3 Size change of inclusions

Average size of the observed inclusions in the "Area 1" of the heated samples A and B was shown in **Table 3-5**. Average size of Al_2O_3+TiO_x+(Al_2O_3-TiO_x)+TiN inclusion, i.e. 4.1 μm, in the sample A after heating was almost the same as that of Al_2O_3+TiN inclusion in the sample before heating, i.e. 4.6 μm, since Al_2O_3+TiO_x+(Al_2O_3-TiO_x)+TiN inclusion was formed by the reaction between Al_2O_3+TiN inclusion and Ti in the metal as explained in previous Sec. 3.2.2.2.

The average size of the observed Al_2O_3+TiO_x+TiN+TiS inclusion after heating was quite large as 11.7 μm because TiS was just formed on the surface of pre-existing large Al_2O_3+TiO_x+TiN inclusion by heating.

In the case of the sample B, the average size of Al_2O_3 and Al_2O_3+TiN inclusions increased from 3.5 to 4.0 and 4.5 to 6.9 μm, respectively. On the other hand, the average size of MgO based inclusions decreased.

Although these size changes of each inclusion type occurred by heating, overall size distribution was not observed in the samples A and B. **Figure 3-9** shows the size distribution of inclusions in the samples A and B. Black line means the size distribution of inclusions in the samples before heating. Maximum peaks of size distribution in the samples A and B before and after heating were located at 1.5 to 2.5 μm.

Table 3-5. Average size of the observed inclusions in the "Area 1" of samples A and B.

(μm)

Inclusion type	A		B	
	Before heating	**After heating**	**Before heating**	**After heating**
Al_2O_3	2.9	2.9	3.5	4.0
Al_2O_3+TiN	4.6	4.1	4.5	6.9
Al_2O_3+TiS	3.7	2.6	-	-
Al_2O_3+TiN+TiS	7.4	4.9	-	-
(Al_2O_3-MgO)	-	-	3.4	1.9
(Al_2O_3-MgO)+TiN	-	-	3.4	4.1
Al_2O_3+(Al_2O_3-MgO)	-	-	4.8	4.8
Al_2O_3+(Al_2O_3-MgO)+TiN	6.4	-	8.5	-
Al_2O_3+(Al_2O_3-MgO)+TiN+TiS	6.8	-	-	-
(Al_2O_3-MgO-TiO_x)	-	-	5.4	-
Al_2O_3+(Al_2O_3-MgO-TiO_x)	-	-	7.4	-
Al_2O_3+TiO_x	-	1.7	5.7	6.0
Al_2O_3+TiO_x+TiN	11.2	6.7	-	-
Al_2O_3+TiO_x+TiN+TiS		11.7	-	-
Al_2O_3+TiO_x+(Al_2O_3-MgO)+TiN	-	-	4.2	-
Al_2O_3+TiO_x+(Al_2O_3-TiO_x)+TiN		4.1	-	-
(Al_2O_3-MgO)+(Al_2O_3-TiO_x)	-	-	3.2	-

- : not detected

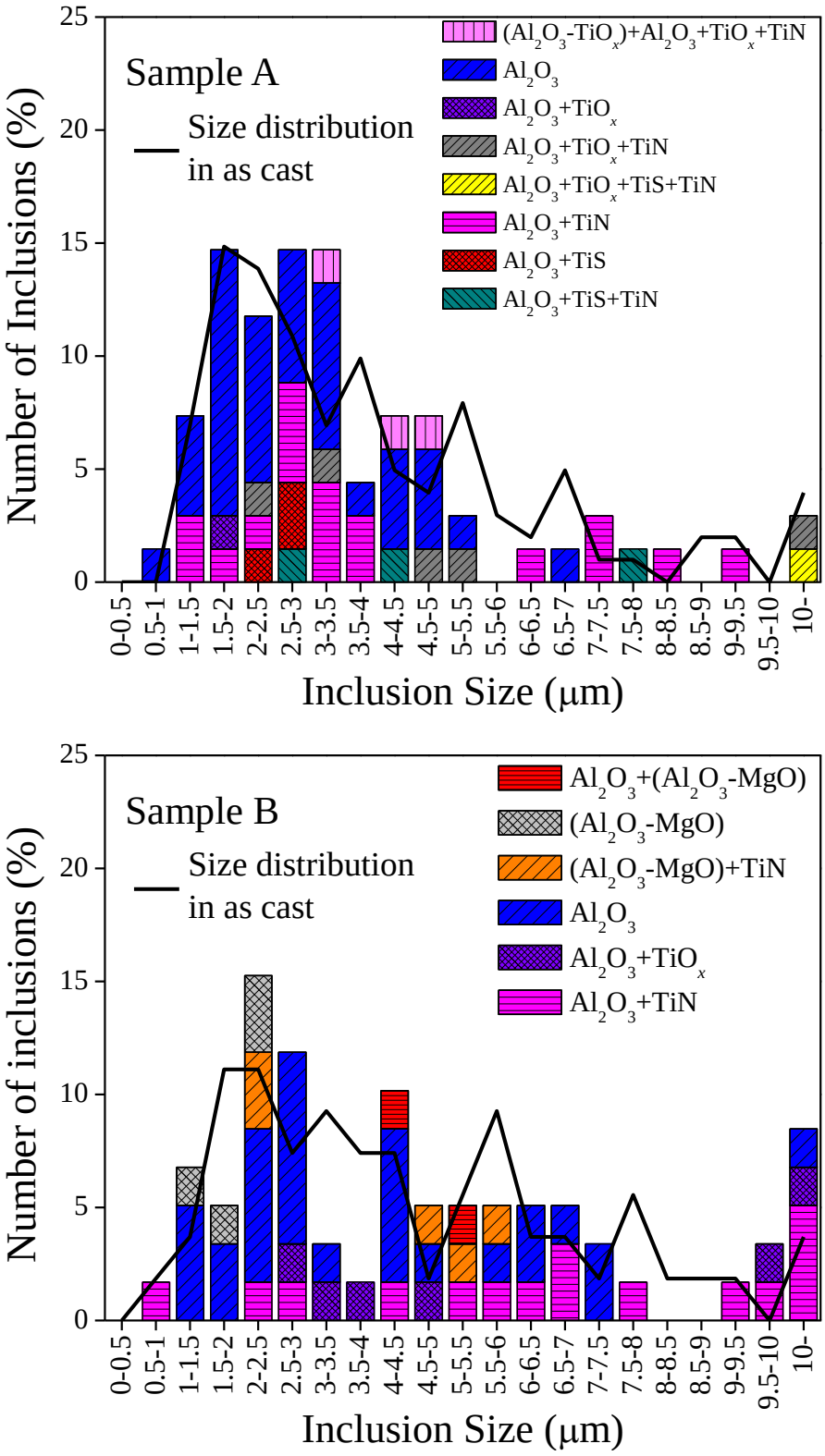

Figure 3-9. Size distribution of inclusions in the "Area 1" of samples A and B before and after heating.

3.2.3 Change behavior of inclusions in inner layer of samples A and B by heating

3.2.3.1 Type and compositional change of inclusions

Figure 3-10 shows the change of inclusion types in the inner layer of the samples A and B by heating at 1473 K. In the sample A, fraction of TiN inclusion increased by heating. However, fraction of TiS based inclusions, i.e. TiS and TiN+TiS, decreased. In the case of oxide types of inclusions, MgO based inclusions were hardly observed after heating.

In the sample B, fraction of TiN inclusion increased and fraction of (Al_2O_3-MgO)+TiN inclusion decreased by heating as well as the sample A. However, TiS based inclusions were more openly observed. This type change behavior in the sample B was exactly opposite results compared with that in the sample A. Fraction of Al_2O_3+TiN inclusion decreased by 7.3%, while 1.3% of Al_2O_3 inclusion, which did not exist before heating, was observed by heating.

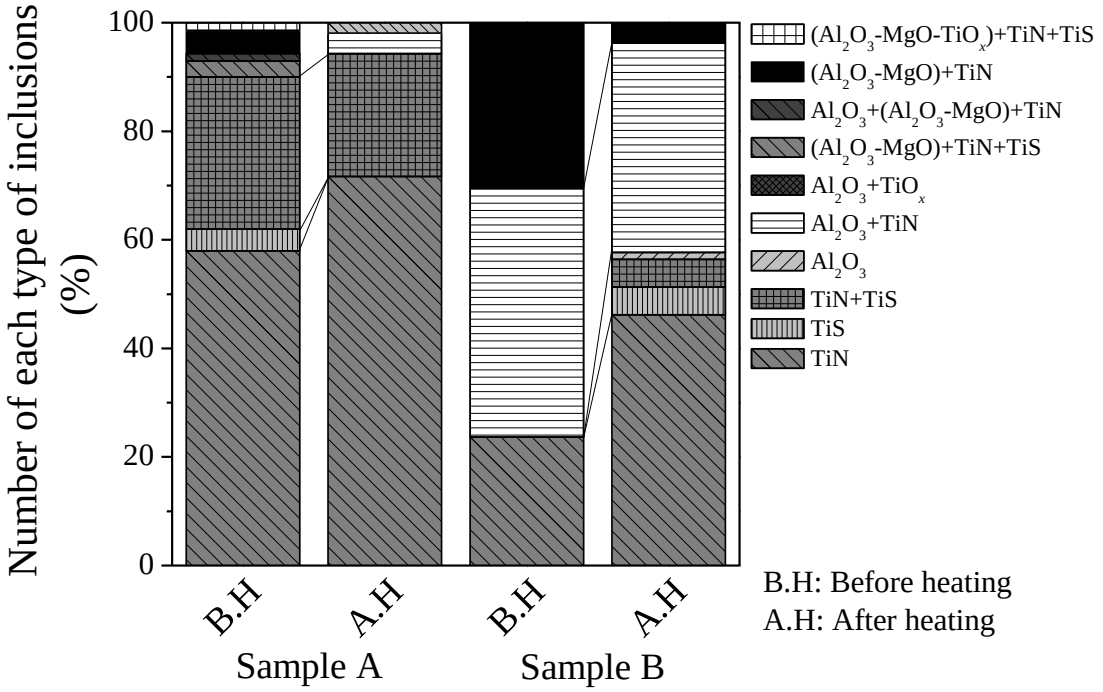

Figure 3-10. Type change of inclusions in the inner layer of the samples A and B before and after heating.

The change behavior of oxide inclusions in the inner layer of both samples would be affected by equilibrium oxide at the each metal composition at 1473 K.

3.2.3.2 Size change of inclusions

Figures 3-11 and **3-12** show the change of average size of inclusions in the samples A and B, respectively. In the figures, minimum and maximum sizes of each type of inclusions were represented by error bar. When only one inclusion is observed, error bar is not indicated.

In the case of the sample A, average size of TiN and TiN+TiS inclusions in the samples before and after heating were almost similar. The pre-existing TiS inclusions less than 1 μm were not detected anymore in the heated sample.

The size of the observed Al_2O_3+TiN and Al_2O_3+TiN+TiS inclusions in the heated sample was quite large from 4.8 to 6.1 μm. Such types of big inclusions would be formed by evolution of pre-existing Al_2O_3-MgO inclusion rather than precipitation.

As explained in Secs. 3.2.2.1 and 3.2.2.2, TiO_x based inclusions were usually formed by heating with opposite phenomenon of dissolution of Al_2O_3-MgO inclusions in the outer layer. However, TiO_x phase was not observed in the inner layer. This phenomenon would be occurred by sufficiently provided Ti and O sources in the outer layer. It can be expounded by that evolution of inclusions can be affected by not only bulk metal composition but also partial morphology change of primarily existing inclusions.

In the case of the sample B, even if TiN inclusion more than 1 μm was only observed in the heated sample, the average size was slightly decreased by heating as shown in **Fig. 3-12**. It would be explained by newly precipitated small TiN particles during heating. TiS and TiN+TiS inclusions less than 1 μm were also formed by heating.

The average size of Al_2O_3+TiN inclusions slightly decreased. However, minimum size of Al_2O_3+TiN inclusion increased from 0.3 to 0.7 μm. It means that the number of Al_2O_3+TiN

inclusions in the size range from 0.7 to 1.4 μm increased by heating. By considering the number change of Al_2O_3+TiN inclusion together, around 1 μm of Al_2O_3+TiN inclusion would be formed during heating.

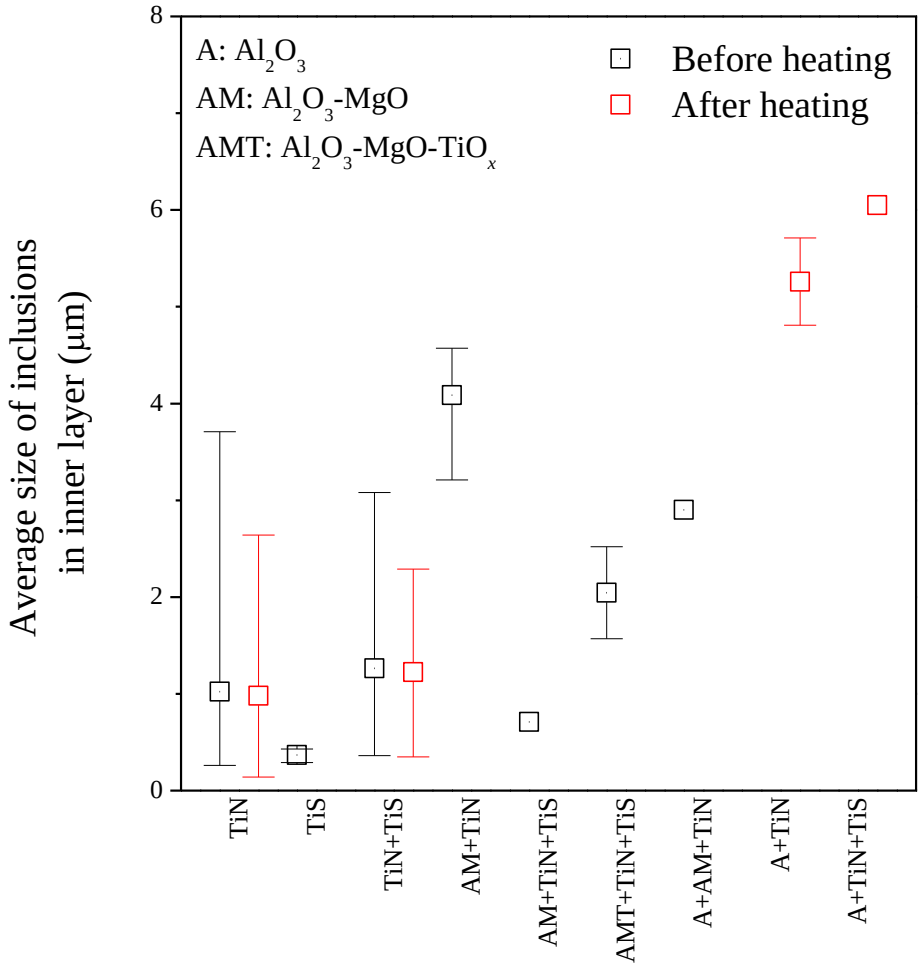

Figure 3-11. Size change of inclusions in the inner layer of the sample A before and after heating.

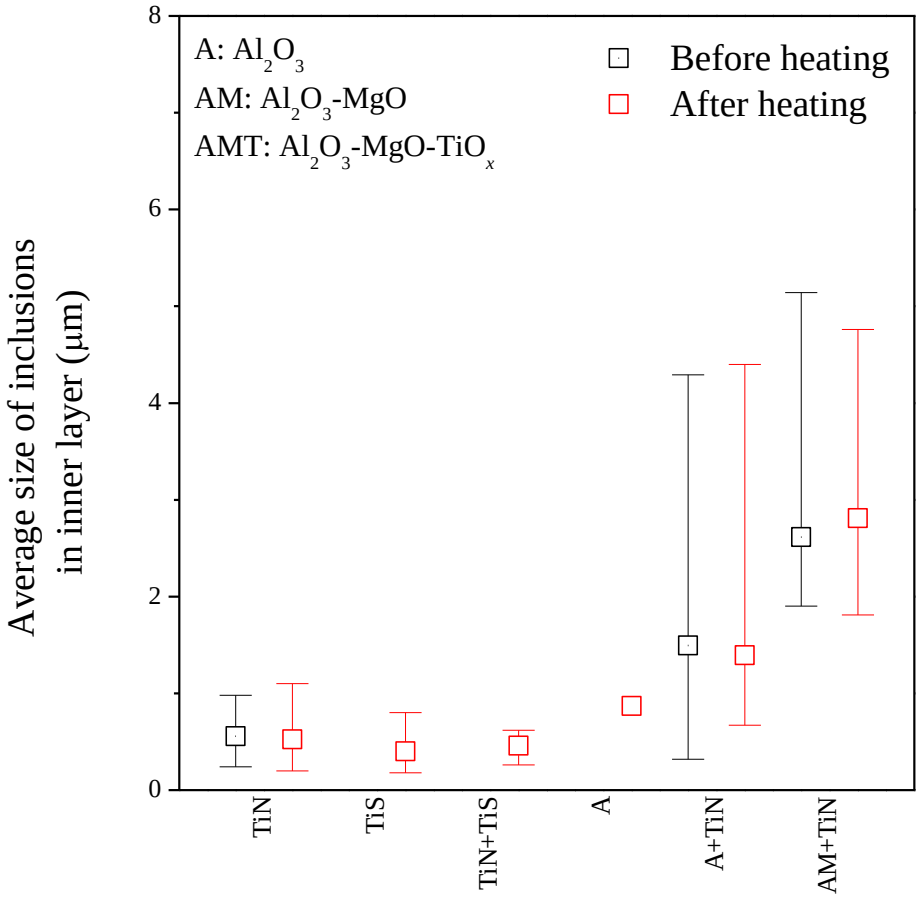

Figure 3-12. Size change of inclusions in the inner layer of the sample B before and after heating.

Figure 3-13 shows size distribution of inclusions in the samples A and B before and after heating. In the case of the sample A, almost similar size distributions were observed before and after heating.

On the other hand, in the case of the sample B, even though maximum peaks were observed in the same range of from 0.5 to 1 μm, overall size of inclusions decreased by heating due to the formation of small TiN and Al_2O_3+TiN inclusions as explained above.

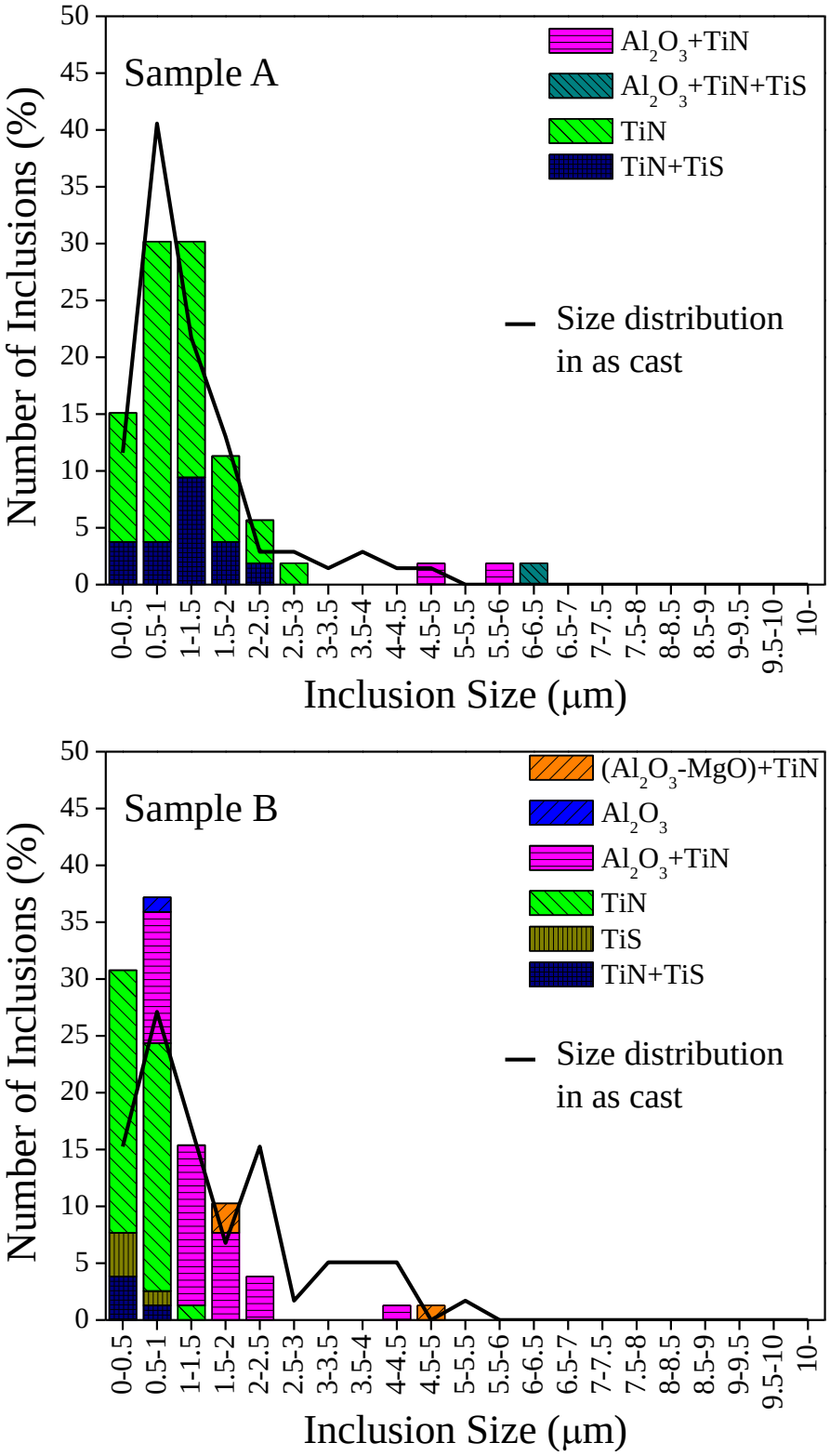

Figure 3-13. Size distribution of inclusions in the inner layer of the samples A and B before and after heating.

3.2.3.3 Shape change of inclusions

The definition of shape of inclusions in the inner layer has been described in Sec. 2.3.3.3. **Figures 3-14** and **3-15** show the morphology change of inclusions in the inner layer of the samples A and B, respectively.

In the case of sample A, fraction of cluster type of TiN and/or TiS inclusions increased from 3 to 24 %. On the other hand, fraction of irregular and polyhedral types of TiN and/or TiS inclusions slightly decreased by heating for 3 hours. It indicated that TiN or TiS precipitated on the pre-existing polyhedral or irregular types of TiN and/or TiS inclusions during heating.

All the observed oxide+TiN and/or TiS inclusions were polyhedral type in the heated sample A. In other words, TiN or TiS covered all surface of oxide phase. From these results, it can be considered that TiN or TiS formed on the nucleation site, i.e. unstable surface of the pre-existing inclusions, rather than its homogeneous nucleation.

In the case of sample B, fraction of polyhedral and irregular types of TiN and/or TiS inclusions slightly decreased from 93 to 86 and 7 to 5 %, respectively. On the other hand, fraction of cluster and roundish types of TiN and/or TiS inclusions slightly increased by heating. Especially, all of the observed roundish type inclusions were TiS single particles. By heating, precipitation of TiS single particles and formation of TiN on the surface of pre-existing TiN and/or TiS inclusions occurred.

The fraction of polyhedral type of oxide+TiN and/or TiS inclusions decreased. Consequently, the fraction of irregular type of oxide+TiN and/or TiS inclusions increased by heating. In other words, oxide+TiN and/or TiS inclusions in which TiN and/or TiS phase was partially precipitated on the oxide surface were more easily observed. It would be explained as follows.

As mentioned in Sec. 3.2.3.2, small Al_2O_3+TiN inclusions formed by heating. The mechanism of formation of such kind of small Al_2O_3+TiN inclusions might be that Al_2O_3 formed first and grew until particular particle size and then TiN formed on the Al_2O_3 particles. Since it might take some time for Al_2O_3 formation and growth, there was no time to cover Al_2O_3 phase by TiN. Therefore,

irregular type of oxide+TiN and/or TiS inclusions was more easily observed in the heated sample.

Besides, the size of Al_2O_3 phase in the Al_2O_3+TiN inclusions was from 0.62 to 1.65 μm. And, the average size of Al_2O_3 phase was 1.1 μm. From these results, it can be presumed that particular size of Al_2O_3 for TiN formation was at least 0.62 μm in the sample B at 1473 K.

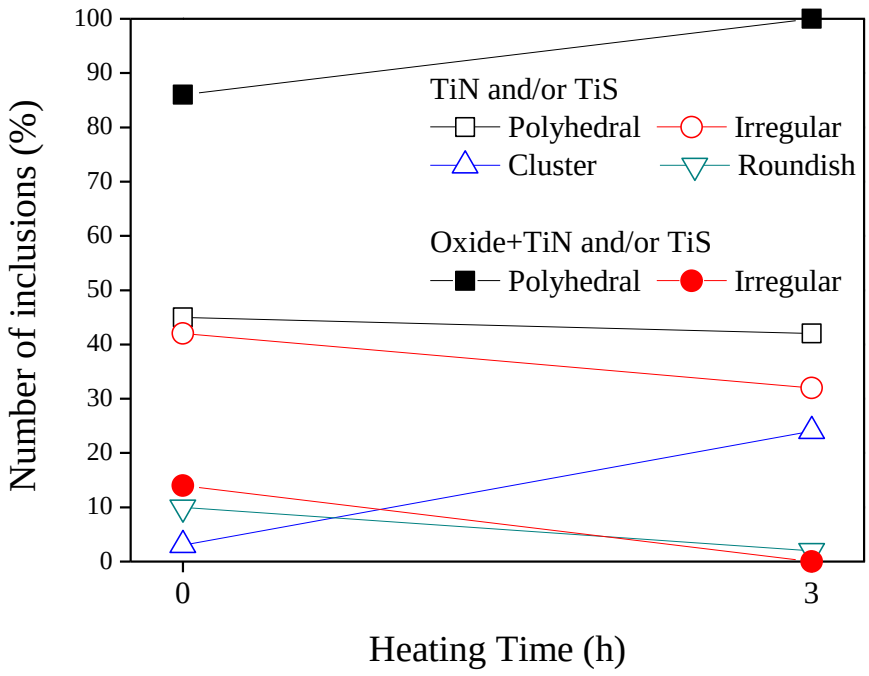

Figure 3-14. Morphology change of inclusions in the inner layer of the samples A by heating.

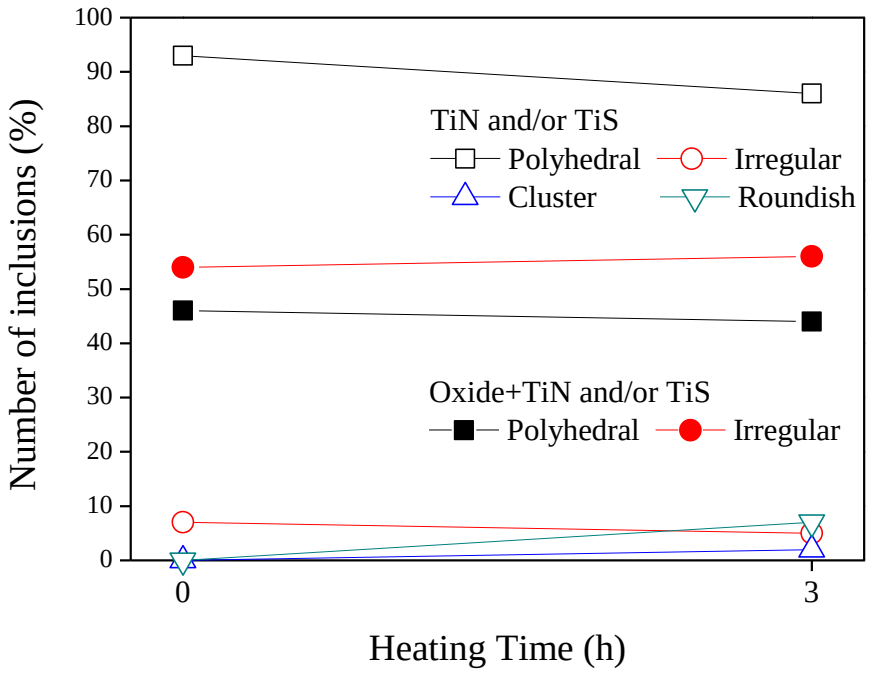

Figure 3-15. Morphology change of inclusions in the inner layer of the samples B by heating.

3.2.4 Change behavior of inclusions in outer layer of samples C, D, E and F by heating

3.2.4.1 Type and compositional change of inclusions

Figure 3-16 shows the change of ratio of inclusion types by heating in the outer layer of the samples C, D, E and F. In all heated samples, Al_2O_3 and Al_2O_3+TiN inclusions were mainly observed. In the sample C, some Al_2O_3+TiO_x(+TiN) inclusions were observed. Some Al_2O_3+TiO_x+TiN, Al_2O_3+TiS, TiS and TiN inclusions were also detected in the sample E. In the samples D and F, some TiN inclusions were observed. One of the most evident changes in all samples C, D, E and F by heating was that the fraction of the number of Al_2O_3 inclusions decreased, on the contrary, the fraction of the number of Al_2O_3+TiN inclusions increased by heating as shown in **Fig 3-16**.

From these results, it can be considered that TiN phase usually precipitated on the nucleation sites such as pre-existing inclusions by heating since the fraction of the number of TiN single phase scarcely increased in spite of increasing of the fraction of the number of TiN based inclusions, especially in samples C and E.

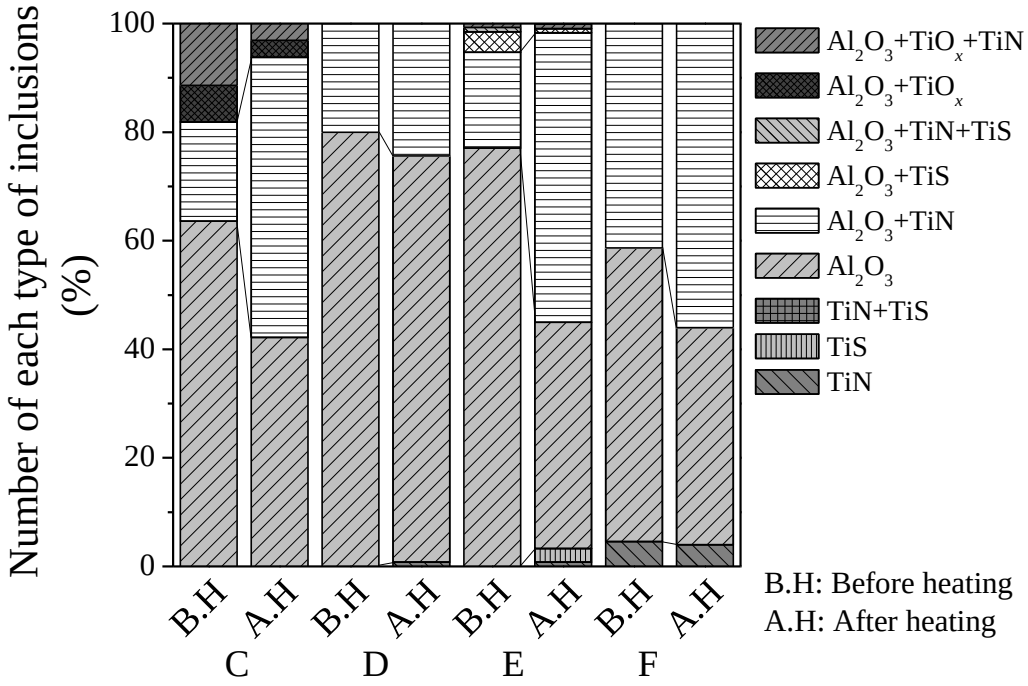

Figure 3-16. Observed inclusion types in the outer layer of samples C, D, E and F before and after heating.

The Al_2O_3+TiO_x based inclusions as shown in **Fig. 2-13** in Sec. 2.3.2.1 were observed in the heated samples C and E. The morphology of Al_2O_3+TiO_x based inclusions did not change by heating, however the change of chemical composition of Al_2O_3+TiO_x based inclusions observed. **Figure 3-17** shows chemical composition change of Al_2O_3+TiO_x based inclusions in the sample C.

As shown in **Fig. 3-17**, change of chemical composition in Al rich part by heating was not detected. On the other hand, Al content in Ti rich part increased from 61 to 80 mol% by heating.

The change of average compositions of Al and Ti in each part of Al_2O_3+TiO_x based inclusions in sample E were shown in **Table 3-6**. By heating, the average compositions of Ti in the Al and Ti rich parts increased by 5 and 10 mol%, respectively.

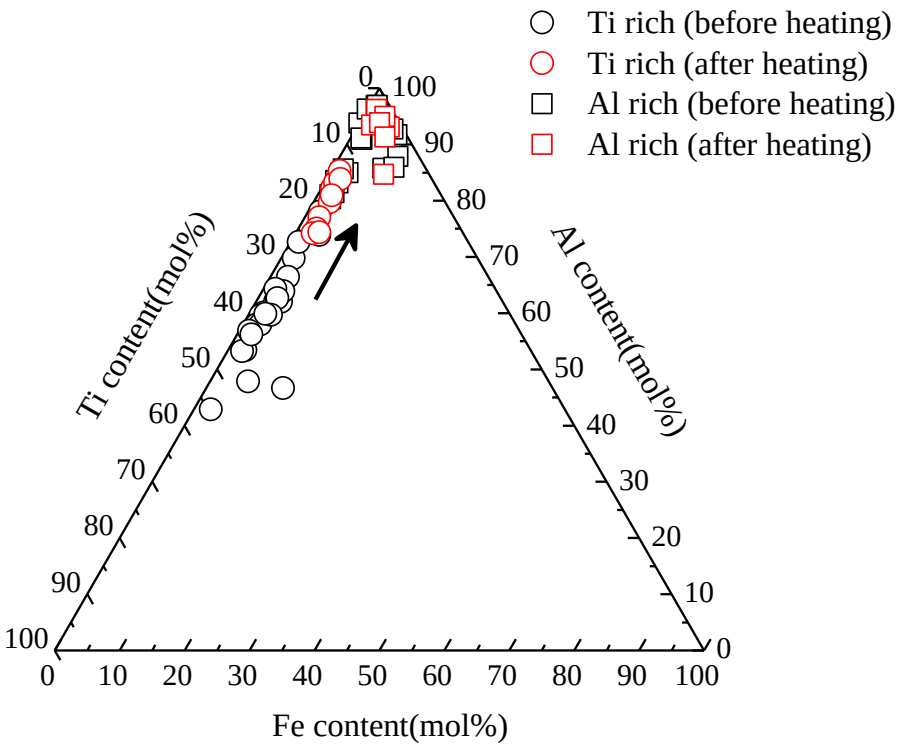

Figure 3-17. Change of chemical composition of the observed (Al_2O_3+TiO_x) based inclusions by heating on the Al-Ti-Fe ternary system in sample C.

Table 3-6. Change of average chemical composition of the observed (Al_2O_3+TiO_x) based inclusions as the Al-Ti binary system in samples E. (mol%)

		Al content	Ti content
Before heating	Al rich	88	12
	Ti rich	60	40
After heating	Al rich	83	17
	Ti rich	50	50

These changing tendencies of composition in two phases, i.e. Al and Ti rich parts, could be very strong evidence to clarify stable oxide at metal composition of samples C and E. It can be considered that Al_2O_3 was stable oxide in sample C, on the other hand, TiO_x was stable in sample E. Furthermore, since metal compositions of samples D and F were very similar with those of samples C and E as shown in **Fig. 2-4** in Sec. 2.3, stable oxide in samples D and F is expected to be Al_2O_3 and TiO_x, respectively.

3.2.4.2 Size change of inclusions

Figures 3-18 and **3-19** show the size change of inclusions in the samples C, D, E and F. In the sample C, average size of the observed Al_2O_3 inclusions slightly increased by heating. However, the average size of Al_2O_3+TiN inclusions decreased from 4.6 to 2.8 μm. In the sample E, around 0.6 μm of TiN and TiS formed by heating. And, average size of Al_2O_3 and Al_2O_3+TiN inclusions decreased from 3.1 to 1.8 and 3.8 to 3.3 μm, respectively. In the case of samples D and F, average size change of the pre-existing inclusions, i.e. Al_2O_3 and Al_2O_3+TiN inclusions in sample D and TiN, Al_2O_3 and Al_2O_3+TiN inclusions in sample F, was very insignificant.

The size change of Al_2O_3 and Al_2O_3+TiN inclusions in the samples C and E would be explained as follows.

As explained in Sec. 3.2.4.1, TiN usually formed on the Al_2O_3 inclusions. Especially, in the samples C and E, since TiN would form on the Al_2O_3 inclusions which size was less than the average size of Al_2O_3+TiN inclusions, around 5 μm, the average size of the observed Al_2O_3+TiN inclusions in the heated samples could decrease. Therefore, the average size of the observed Al_2O_3 inclusion increased in sample C. However, the average size of the observed Al_2O_3 inclusion decreased in sample E. The reason would be partial dissolution of Al_2O_3 inclusions since Al_2O_3 was not stable in sample E. Stable oxide was explained by measuring of composition change of Al_2O_3+TiO_x based inclusions in Sec. 3.2.4.1.

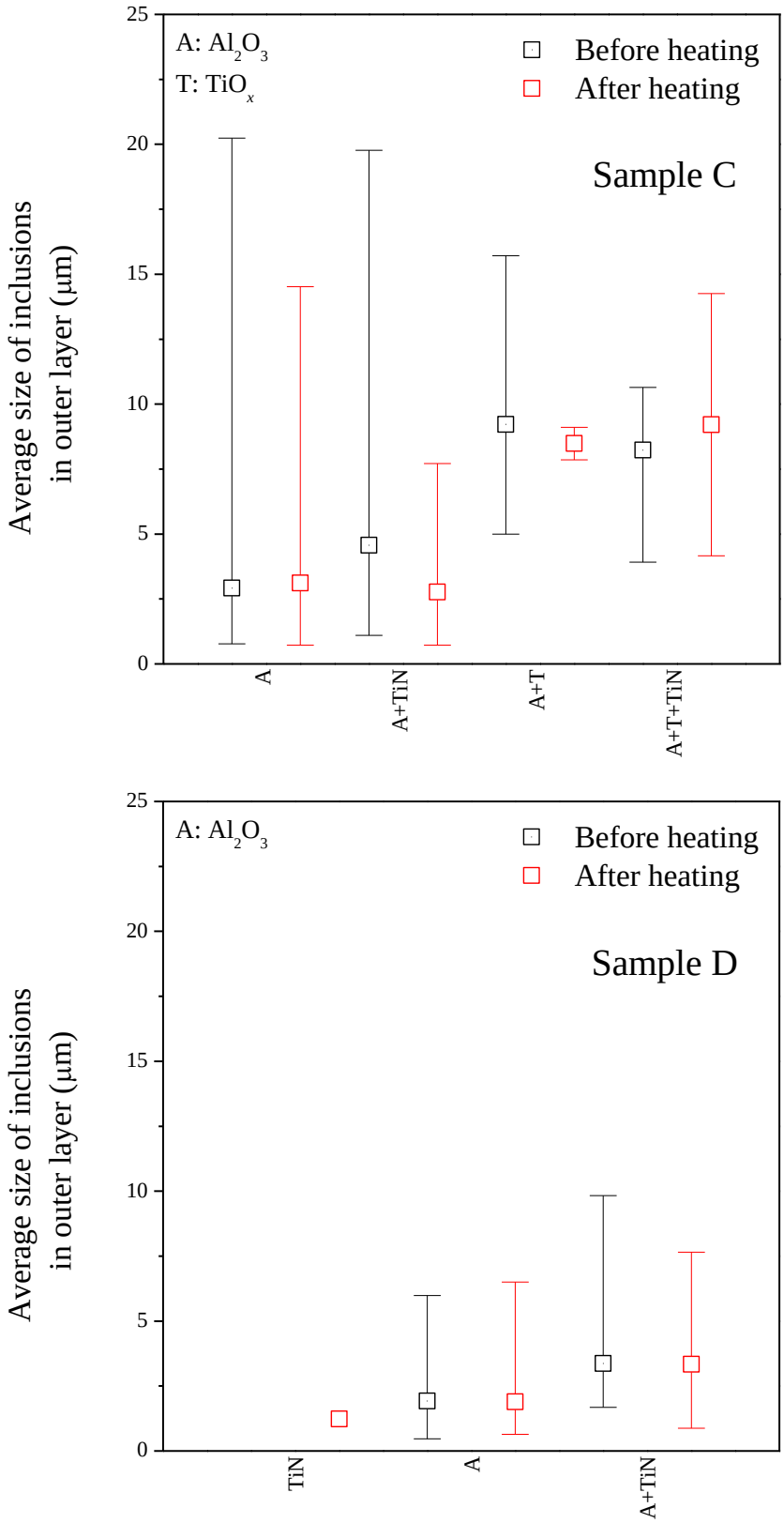

Figure 3-18. Size change of inclusions in the outer layer of the samples C and D by heating.

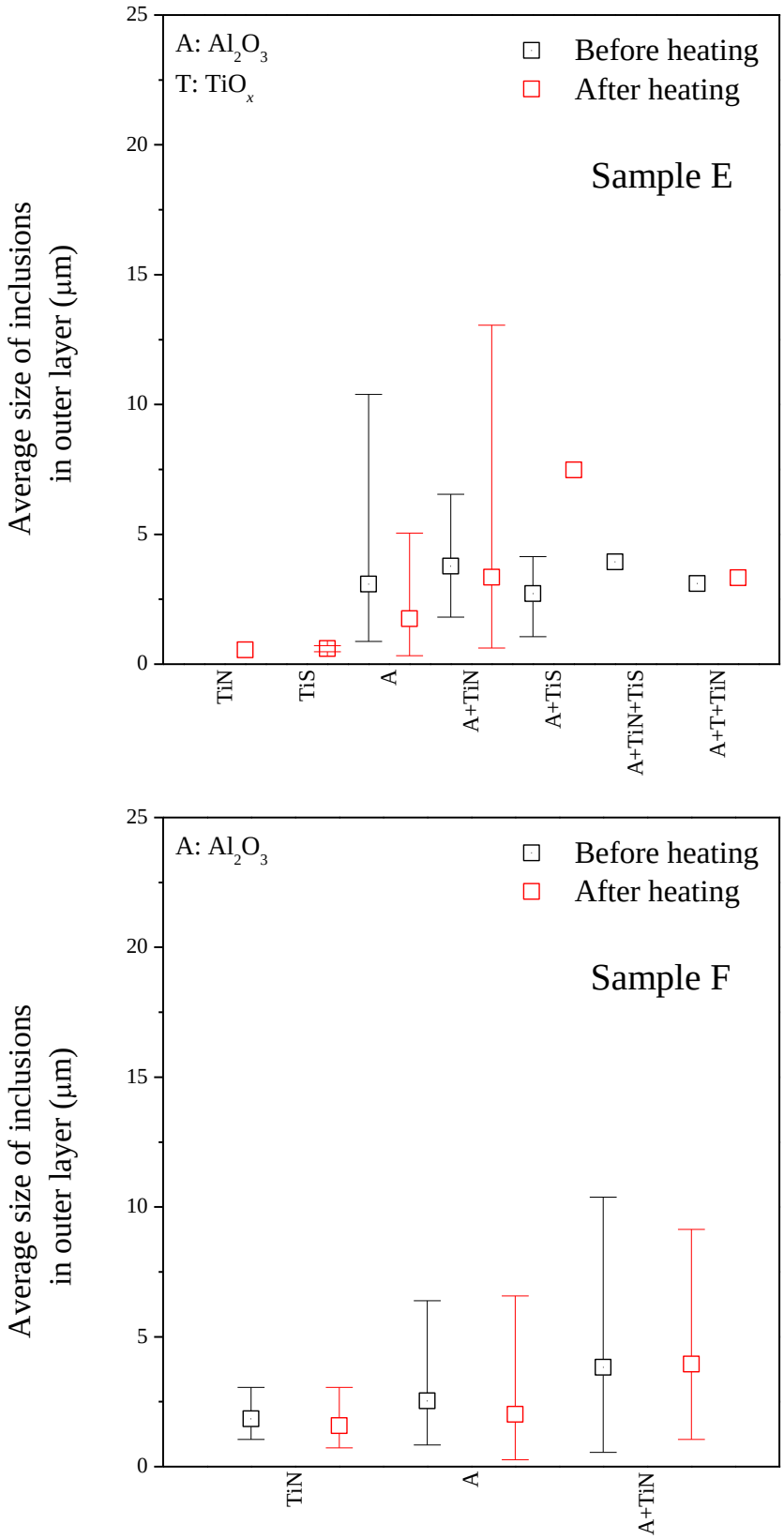

Figure 3-19. Size change of inclusions in the outer layer of the samples E and F by heating.

Figures 3-20, **3-21** and **3-22** show the size distribution of inclusions in the samples C, D, E and F before and after heating. In the case of the samples D and F, the size distributions of inclusions in samples before and after heating were very similar.

The number of inclusions in the range from 1 to 1.5 μm increased around 2 times in the sample C. From this result, it was indicated that TiN formed on the Al_2O_3 less than 1 μm.

In the case of the sample E, the size distribution slightly moved to the left by heating, i.e. size of inclusions decreased due to dissolution of Al_2O_3 inclusions as explained above.

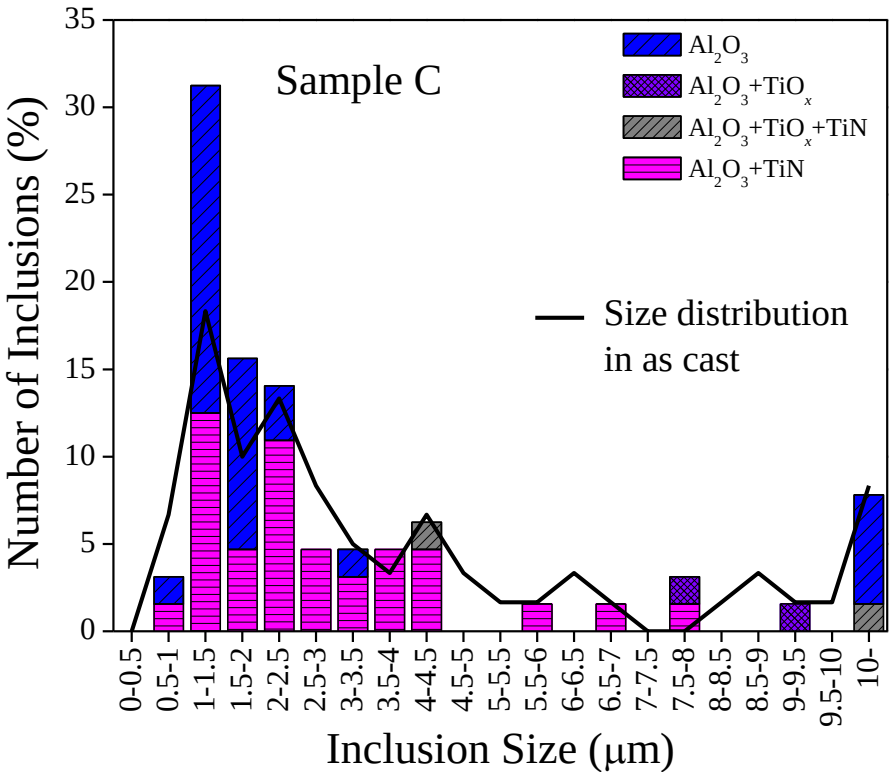

Figure 3-20. Size distribution of inclusions in the outer layer of the sample C before and after heating.

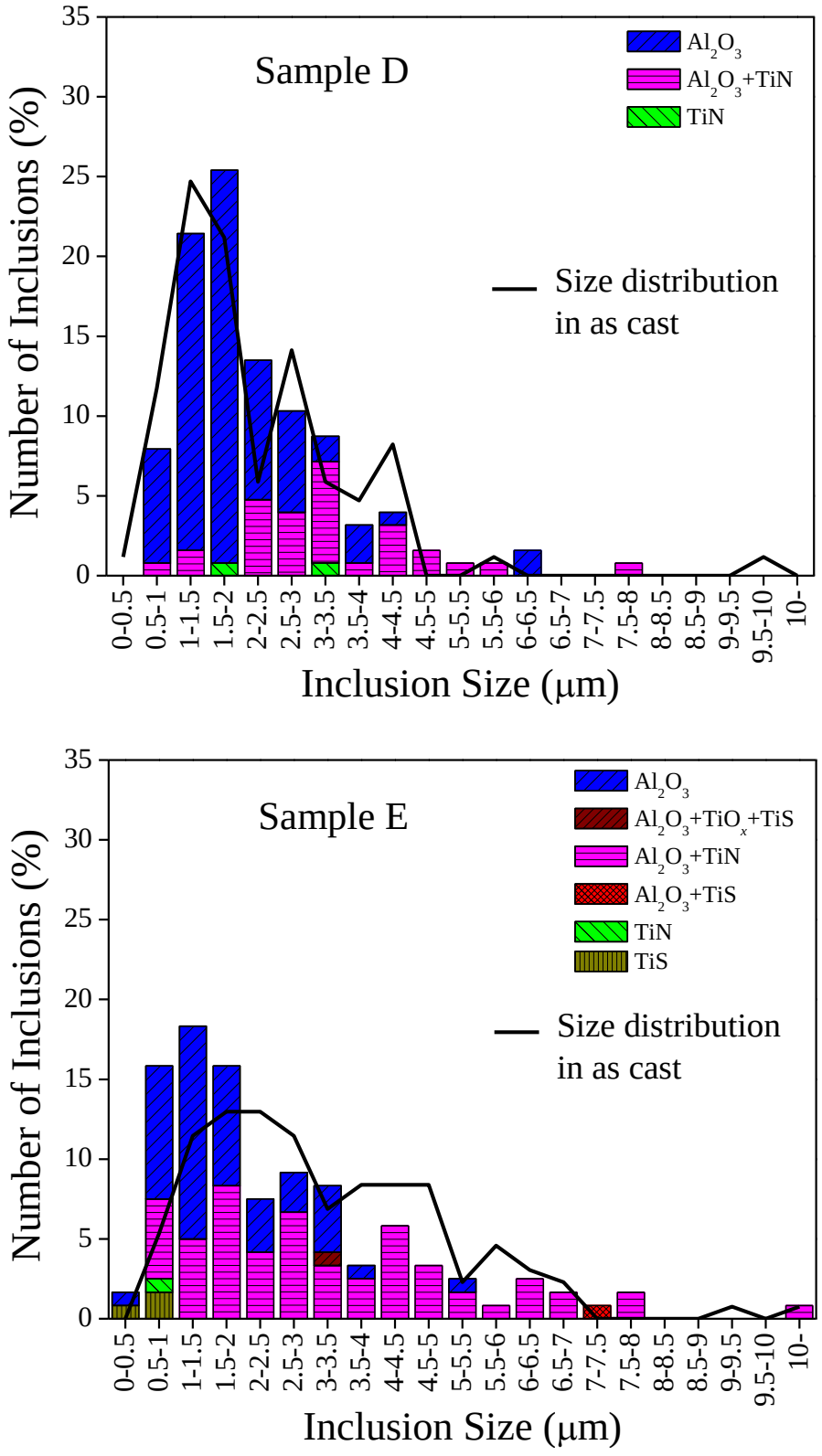

Figure 3-21. Size distribution of inclusions in the outer layer of the samples D and E before and after heating.

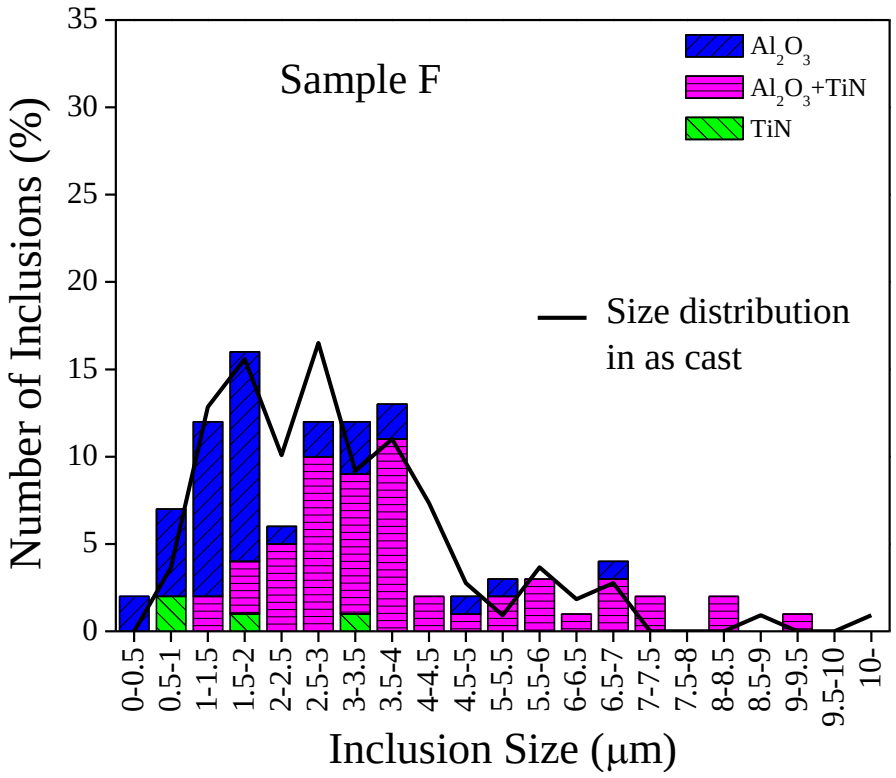

Figure 3-22. Size distribution of inclusions in the outer layer of the sample F before and after heating.

3.2.5 Change behavior of inclusions in inner layer of samples C, D, E and F by heating

3.2.5.1 Type and compositional change of inclusions

Figure 3-23 shows the change of fraction of inclusion types by heating in the inner layer of the samples C, D, E and F. In the sample C, mostly TiN, TiS and Al_2O_3+TiN inclusions were observed, and some TiN+TiS, Al_2O_3+TiS, Al_2O_3+TiN+TiS and Al_2O_3+TiO_x inclusions were also observed. In the case of sample D, almost all inclusions were TiN and some Al_2O_3+TiN inclusions were also detected. In the case of sample E, TiN, TiS and TiN+TiS were main inclusion. Some Al_2O_3,

Al_2O_3+TiN(+TiS) and Al_2O_3+TiS inclusions were observed. TiN(+TiS), TiS and Al_2O_3+TiN(+TiS) inclusions were observed in the sample F.

The fraction of the number of TiS-based inclusion increased in the inner layer by heating. The fraction of the number of TiS-based inclusions in samples C and E increased to 38 and 68 %, respectively. On the other hand, TiS inclusions were not detected in sample D and observed TiS-based inclusions were 32 % of total inclusions in the sample F.

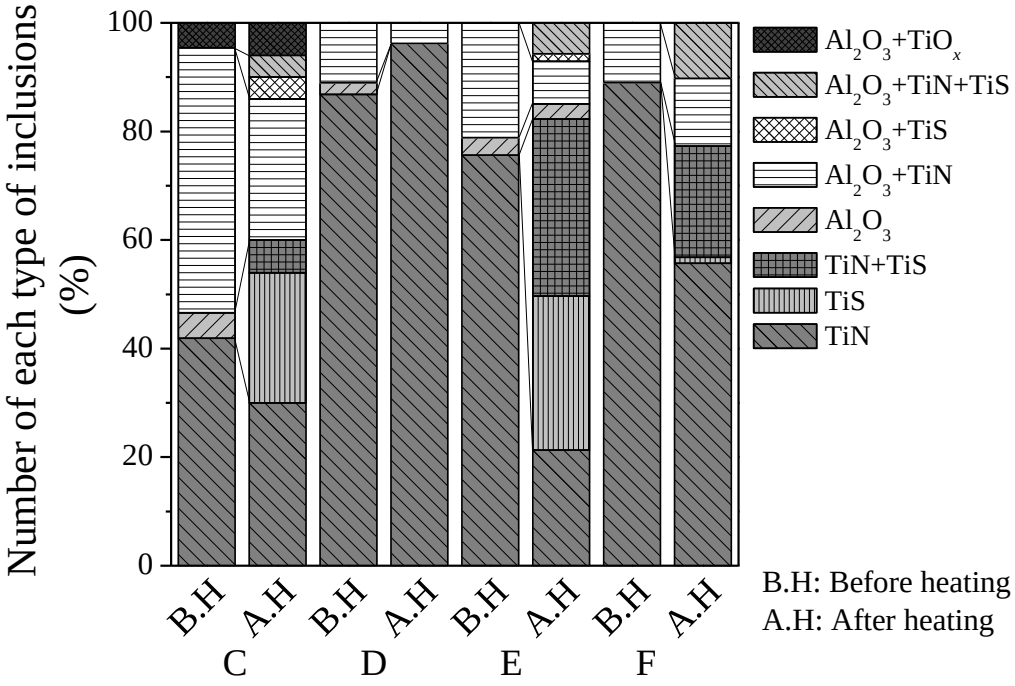

Figure 3-23. Observed inclusion types in the inner layer of samples C, D, E and F before and after heating.

3.2.5.2 Size change of inclusions

Figures 3-24 and **3-25** show the size change of inclusions in the samples C, D, E and F. The average size of TiN inclusions increased by heating in the samples C, D and F. On the contrary, in the sample E, the average size of TiN inclusions decreased. This tendency can be explained by the formation of small TiN particles by heating. The average size of the observed TiN+TiS inclusions in the heated samples C and F was much larger than those of pre-existing TiN in the before heating samples C and F since TiS formed on the TiN particles. The formed TiS particles by heating in the samples C, E and F were very tiny less than 1 μm. Therefore, it can be concluded that TiN particles not only grew but also precipitated during heating and TiS phase usually precipitated on the pre-existed TiN or formed homogeneously.

In the samples C and D, the average size of Al_2O_3+TiN inclusions increased. The opposite size transformation tendency was observed in the samples E and F, even the formation of TiN on the Al_2O_3 inclusions which have similar size of pre-existing Al_2O_3(+TiN) inclusions and growth of TiN phase in the pre-existing Al_2O_3+TiN inclusions would occur simultaneously, which leads to the size increase of Al_2O_3+TiN inclusions by heating. These tendencies are due to the dissolution of Al_2O_3 phase depending on stable oxide observed in the outer layer of each sample.

Figures 3-26 and **3-27** show the size distribution of inclusions in the samples C, D, E and F before and after heating. In the case of sample C, inclusions in the range from 0.5 to 1 μm decreased significantly due to growth of TiN and formation of TiN and TiS on the Al_2O_3 and TiN as seen previously in the results of average size change of inclusions.

The fraction of number of inclusions less than 0.5 μm increased by heating in the sample D because of the formation of small TiN particles. In the heated sample E, inclusions less than 1 μm were mainly observed. As shown in **Fig 3-27**, the fraction of inclusion in the range from 0 to 1 μm increased mainly due to the TiS formation.

In the case of samples F, no change of size distribution by heating was observed.

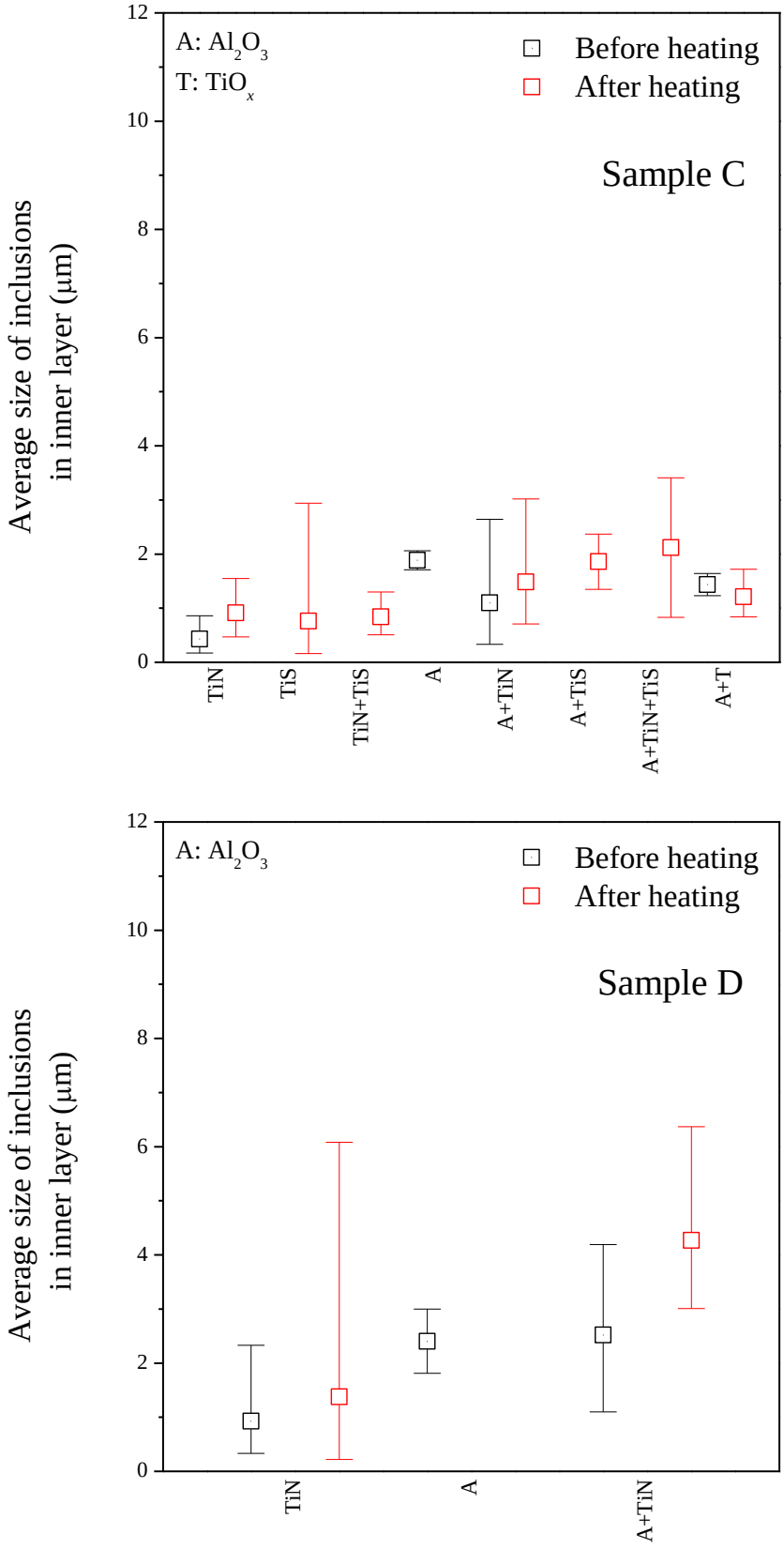

Figure 3-24. Size change of inclusions in the inner layer of the samples C and D by heating.

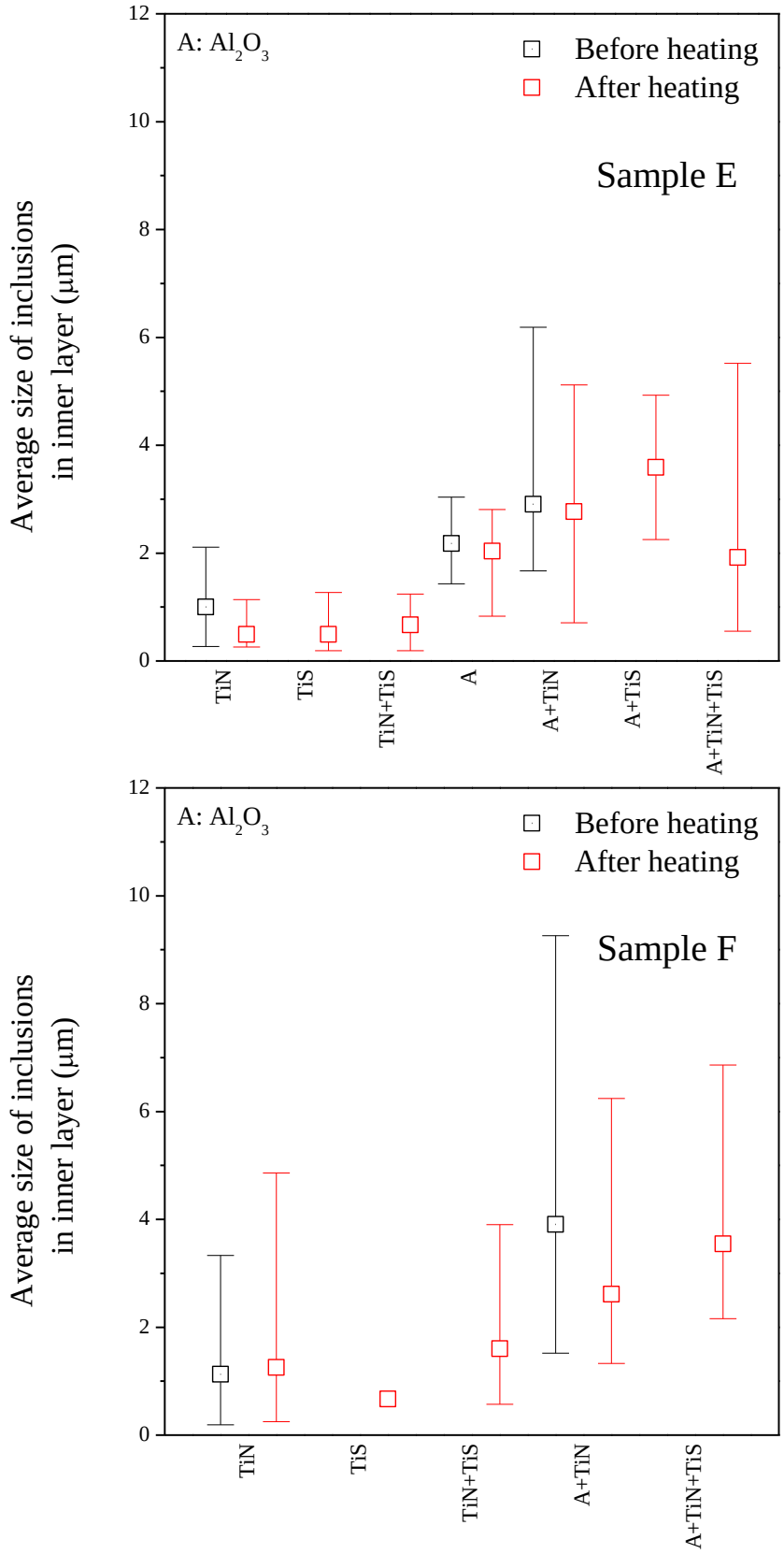

Figure 3-25. Size change of inclusions in the inner layer of the samples E and F by heating.

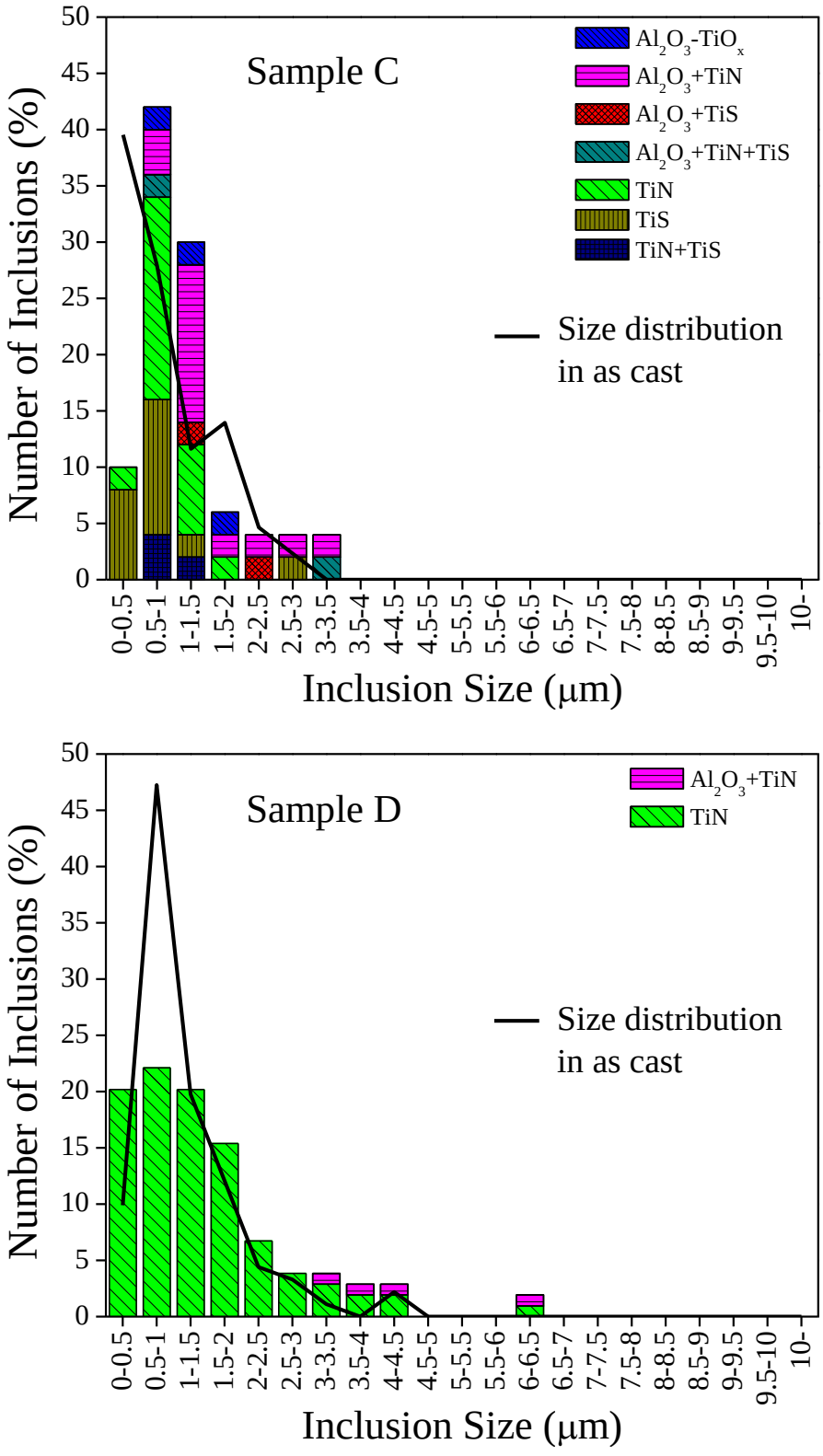

Figure 3-26. Size distribution of inclusions in the inner layer of the samples C and D before and after heating.

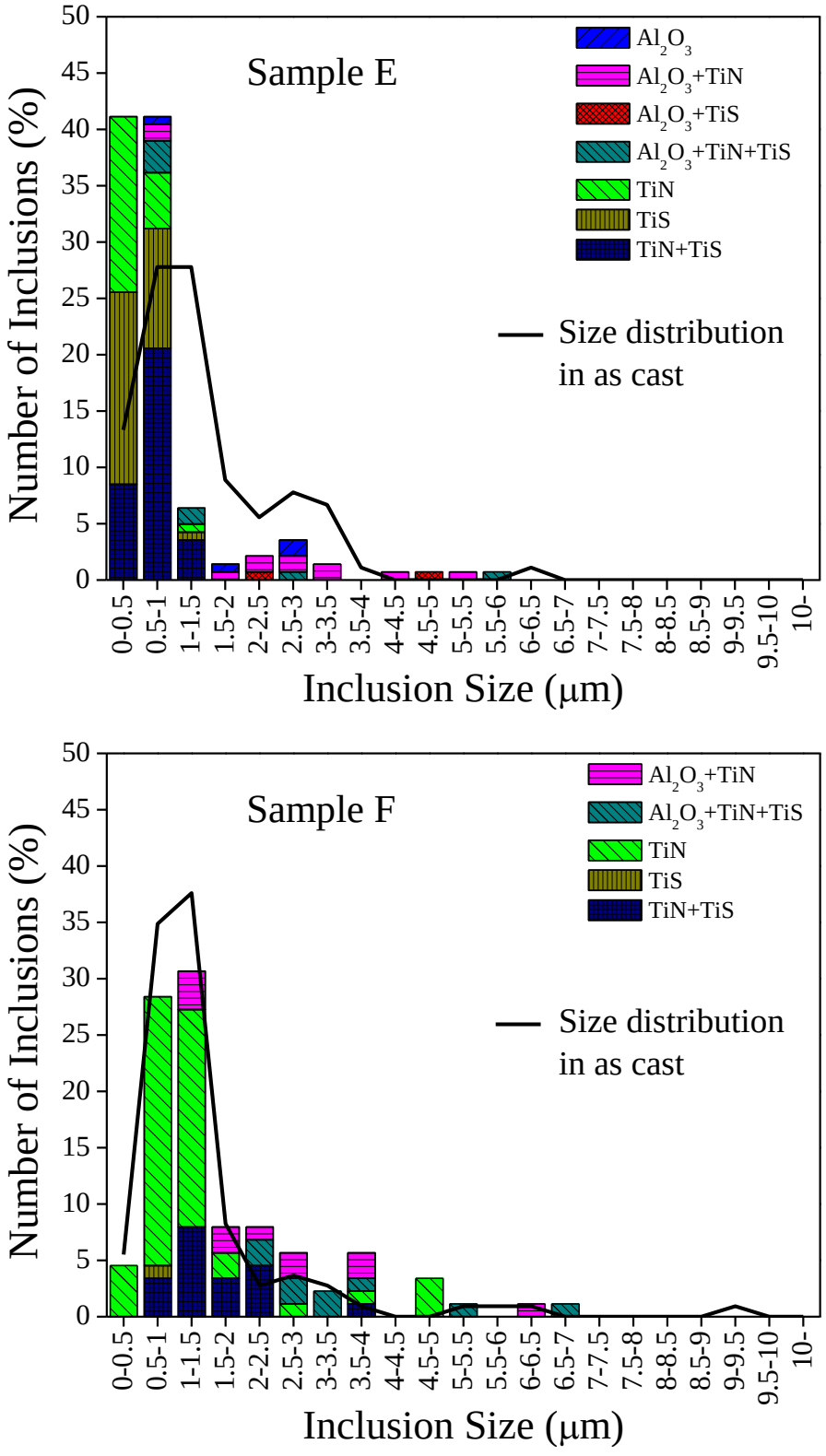

Figure 3-27. Size distribution of inclusions in the inner layer of the samples E and F before and after heating.

3.2.5.3 Shape change of inclusions

The definition of shape of inclusions in the inner layer has been described in Sec. 2.3.3.3. **Figures 3-28** and **3-29** show the morphology change of inclusions in the inner layer of the samples C, D, E and F.

In the case of sample C, fraction of polyhedral type of TiN and/or TiS inclusions and oxide+TiN and/or TiS inclusions decreased by 31% and 18%, respectively. Roundish type of TiN and/or TiS inclusions increased since the formed TiS inclusions were roundish type. Increase in roundish type of TiN and/or TiS inclusions was also observed in the sample E. Irregular type also increased by heating due to formation of TiN and TiS on the TiN. However, cluster type of inclusions, which consists of more than three phases, did not form by heating.

Shape change behavior in the samples D and F was very similar. In the samples D and F, the number of polyhedral type of TiN and/or TiS inclusions decreased. On the other hand, cluster type of TiN and/or TiS inclusions increased by heating because of formation of TiN and/or TiS on the pre-existing TiN and/or TiS inclusion. The fraction of number of polyhedral type oxide+TiN and/or TiS inclusions increased. In other words, number of oxide inclusion fully covered by TiN and/or TiS increased by heating.

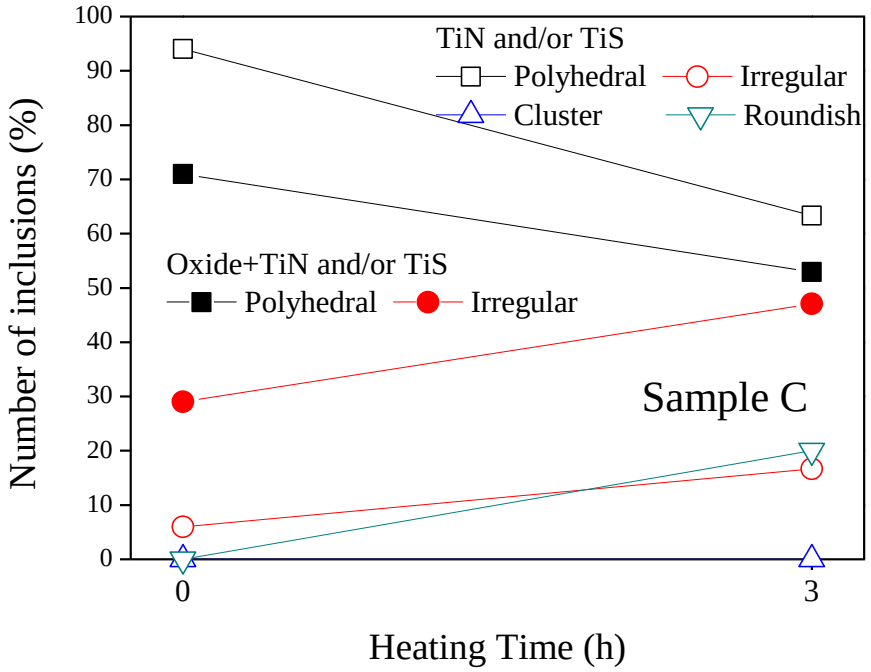

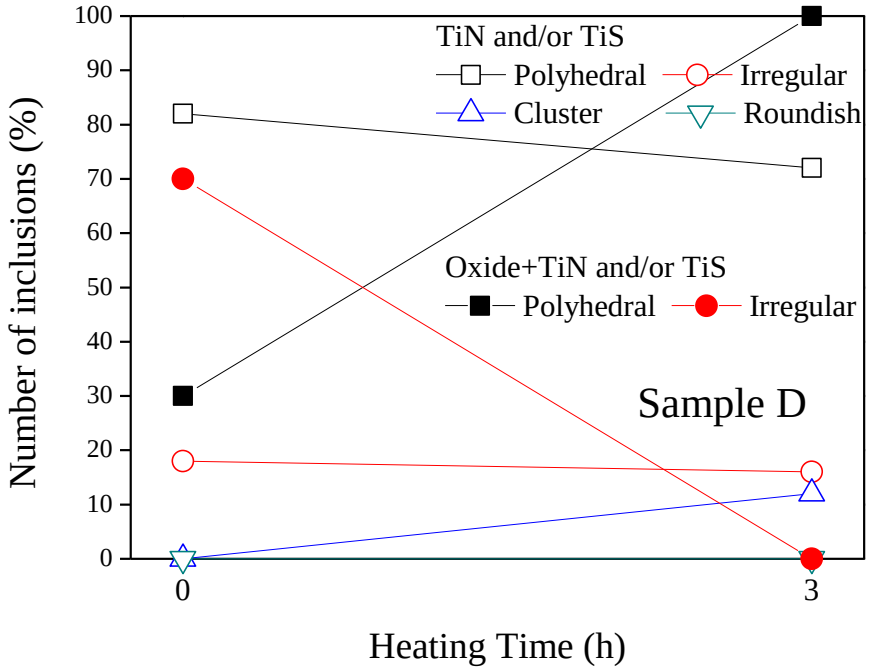

Figure 3-28. Morphology change of inclusions in the inner layer of the samples C and D by heating.

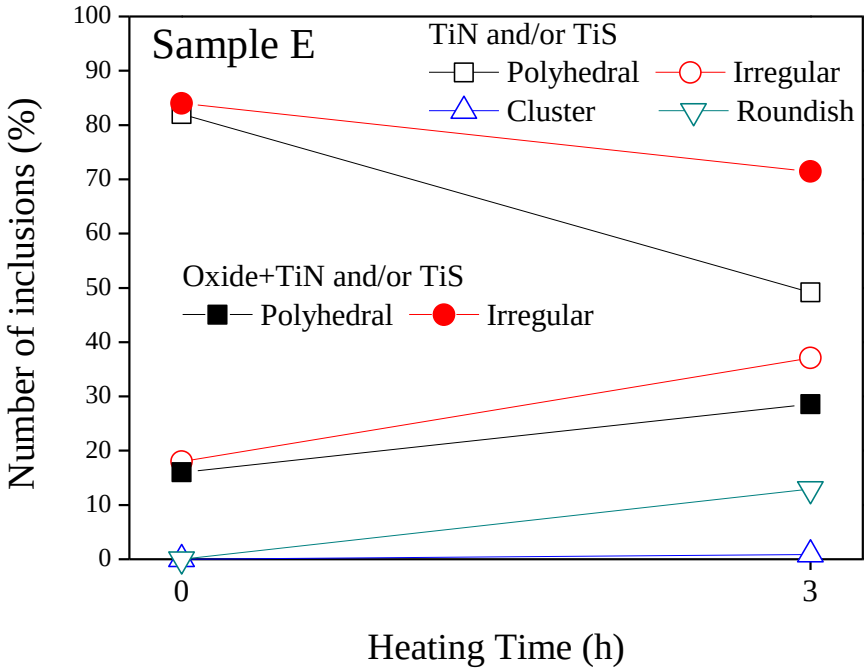

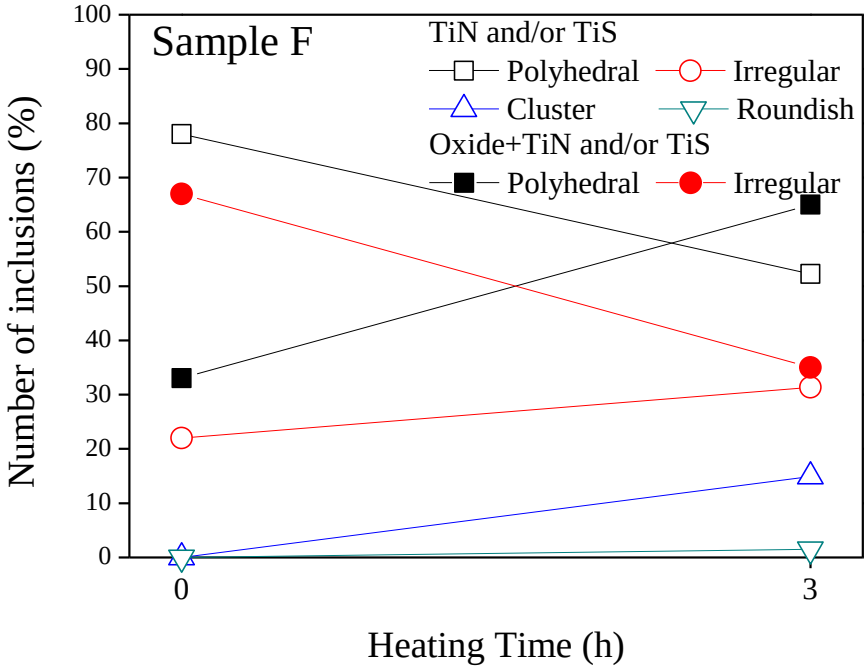

Figure 3-29. Morphology change of inclusions in the inner layer of the samples E and F by heating.

3.2.6 Effect of nitrogen on formation and evolution of inclusions

In the present study, samples C, D, E and F can be distinguished in to two groups with nitrogen content. The samples C and E, which contained 5 and 13 ppm of nitrogen respectively, were regarded as low nitrogen content. On the other hand, nitrogen content in the samples D and F was 58 and 55 ppm, respectively. These samples can be considered as high nitrogen content.

In addition, samples C and D composed of very similar soluble Al and Ti contents and samples E and F also consisted of similar range of soluble Al and Ti contents as shown in **Fig. 2-4** in Sec. 2.3. Therefore, through comparison samples between low and high nitrogen contents, effect of nitrogen content on formation and evolution of inclusions at 1473 K can be investigated.

3.2.6.1 TiS formation

As explained in Sec. 3.2.5.1, TiS based inclusions were more easily observed in the inner layer of samples C and E. Also, fraction of the number of TiS based inclusions increased in the inner layer of sample F.

Comparing between samples D and F, TiS formation in the inner layer of the sample F could be explained as follows. The significant difference between the inner layer of the sample D and that of the sample F is the existence of Al_2O_3 inclusions and metal compositions. Influence of the existence of Al_2O_3 inclusions was insignificant due to the number density of Al_2O_3 inclusion in the inner layer is very low in both samples. Therefore, the reason of TiS formation in the sample F would be the metal composition.

Assuming the interaction parameters are inversely proportional to temperature and using those reported at 1873 K as shown in **Table 2-6** in Sec. 2.3.2.1, interaction parameters at 1473 K can be estimated as shown in **Table 3-7**. By using interaction parameters at 1473 K, the activities of Ti, S and N in the samples C, D, E and F were calculated and were shown in **Table 3-8**.

Table 3-7. Estimated interaction parameters at 1473 K.

e_i^j (i ↓)	Ti	N	S	Al	O
Ti	0.033	-2.06	0.053	-2.59	-0.34
N	0.013	-0.15	-0.640	0	0.009
S	0.052	-0.34	-0.23	0.01	-0.058

Table 3-8. Calculated activities of Ti, S and N at 1473 K.

Sample name	h_{Ti}	h_S	h_N
C	0.0896	0.001626	0.0004388
D	0.0908	0.001147	0.005062
E	0.109	0.001886	0.001107
F	0.120	0.001592	0.004587

The activity of sulfur in the samples D and F was calculated to be 0.001147 and 0.001592, respectively. In addition, the activity of titanium in the samples D and F was 0.0908 and 0.120, respectively. Therefore, it is expected that TiS formation in the sample F is much favorable than that in the sample D.

However, only limited evolution of TiS based inclusions was observed in samples with larger nitrogen content with similar Al and Ti compositions. In the case of samples D and F, most of observed inclusions were still TiN based inclusions. This difference is caused by the preferential evolution and growth of TiN than TiS at larger N content.

The nitrogen and sulfur contents equilibrated with solute Ti in each sample were calculated by **Eqs. (3-5)** and **(3-6)** for solubility products of TiN and TiS.[1, 2)] By using these thermodynamic data and analyzed compositions, the supersaturation ratios of TiN and TiS, SR_{TiN} and SR_{TiS}, defined as **Eqs. (3-7)** and **(3-8)**, respectively, were calculated.

$$\mathrm{TiN(s)} = \mathrm{Ti(mass\%)_{in\,\gamma}} + \mathrm{N(mass\%)_{in\,\gamma}}$$

$$\log[\mathrm{mass\%Ti}]_{\mathrm{eq.\ in\,\gamma}}[\mathrm{mass\%N}]_{\mathrm{eq.\ in\,\gamma}} = -\frac{13{,}860}{T} + 3.75 \quad ^{1)} \tag{3-5}$$

$$\mathrm{TiS(s)} = \mathrm{Ti(mass\%)_{in\,\gamma}} + \mathrm{S(mass\%)_{in\,\gamma}}$$

$$\log[\mathrm{mass\%Ti}]_{\mathrm{eq.\ in\,\gamma}}[\mathrm{mass\%S}]_{\mathrm{eq.\ in\,\gamma}} = -\frac{13{,}975}{T} + 5.43 \quad ^{2)} \tag{3-6}$$

$$SR_{\mathrm{TiN}} = \frac{[\mathrm{mass\%Ti}][\mathrm{mass\%N}]}{[\mathrm{mass\%Ti}]_{\mathrm{eq.\ in\,\gamma}}[\mathrm{mass\%N}]_{\mathrm{eq.\ in\,\gamma}}} \tag{3-7}$$

$$SR_{\mathrm{TiS}} = \frac{[\mathrm{mass\%Ti}][\mathrm{mass\%S}]}{[\mathrm{mass\%Ti}]_{\mathrm{eq.\ in\,\gamma}}[\mathrm{mass\%S}]_{\mathrm{eq.\ in\,\gamma}}} \tag{3-8}$$

where $[\mathrm{mass\%Ti}]_{\mathrm{eq.\ in\,\gamma}}$, $[\mathrm{mass\%N}]_{\mathrm{eq.\ in\,\gamma}}$ and $[\mathrm{mass\%S}]_{\mathrm{eq.\ in\,\gamma}}$ are Ti, N and S contents equilibrated with solid TiN or TiS in γ iron.

The supersaturation ratios of TiN in samples C, D, E and F were 20, 246, 65 and 309, respectively. On the other hand, the supersaturation ratio of TiS in each sample was in the range from 1.2 to 2.5. Although the supersaturation ratios required for TiN and TiS precipitation at 1473 K have not been reported so far, TiN precipitation in samples D and F would be preferable than TiS precipitation during heating. Therefore, TiN based inclusions were still mainly observed after heating in samples D and F.

3.2.6.2 Size change of TiN phase

Figure 3-30 shows the difference between the average size of Al_2O_3+TiN inclusions and that of Al_2O_3 core in Al_2O_3+TiN inclusions, which is l_{TiN} in **Eq. (3-9)**.

$$l_{TiN} = (\text{size of } Al_2O_3\text{+TiN inclusion}) - (\text{size of } Al_2O_3 \text{ core of } Al_2O_3\text{+TiN inclusion}) \quad (3\text{-}9)$$

The change of TiN phase size in the Al_2O_3+TiN inclusion by heating can be determined. The tendency of size distribution of Al_2O_3 phase (Al_2O_3 single phase and Al_2O_3 phase in Al_2O_3+TiN) did not change in all samples except the sample E. At the smaller nitrogen content such as samples C and E, the difference between two sizes slightly increased or decreased by heating. On the contrary, in metals with larger nitrogen content such as samples D and F, the difference certainly increased by heating. Since the fraction of the number of Al_2O_3+TiN inclusion increased in all samples as previously mentioned in Sec. 3.2.4.1, TiN phase newly formed on the Al_2O_3 inclusion during heating. In addition, TiN phase of Al_2O_3+TiN inclusions formed during quenching also grew by heating.

The average size of TiN inclusions in inner layer of samples C, D, E and F before and after heating was shown in **Figures 3-24** and **3-25** in Sec. 3.2.5.2. Maximum size of TiN inclusions in samples D and F with larger nitrogen content was much larger than that in samples with smaller nitrogen content. From this result, it is considered that the growth of TiN inclusions occurred more easily in metal with larger nitrogen content than smaller nitrogen content during heating.

In the case of sample E, average size of TiN inclusions decreased by heating due to the decrease of the observed number of TiN single phase inclusions. The fraction of the number of TiN+TiS inclusions substantially increased from 0 to 33 % during heating by TiS formation on the surface of TiN inclusions.

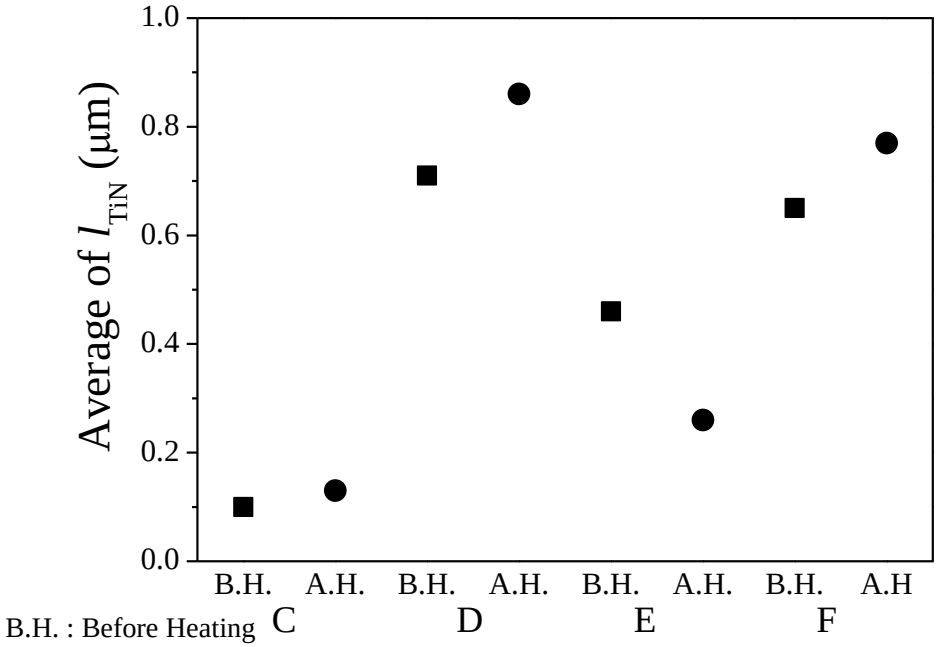

Figure 3-30. Average of l_{TiN} in all samples before and after heating.

3.3 Summary

In this Chapter, formation and change behaviors of various inclusions by heating at 1473 K were investigated. The change of inclusion characteristic such as composition, size and morphology was observed in each sample.

In the samples A and B, characteristic change of inclusions occurred considerably by heating due to the dissolution of pre-existing small Al_2O_3-TiO_x or MgO based inclusions.

In the samples C, D, E and F, TiN phase easily formed or grew and TiS phase also formed. These behaviors were considerably affected by nitrogen content. Besides, through measurement of change tendency of compositions of pre-existing transient oxide inclusions which formed at deoxidation process, stable oxide at each metal composition could be assumed.

References

[1] M. Hino and K. Ito ed.: THERMODYNAMIC DATA FOR STEELMAKING, Tohoku university press, Sendai, (2010), 236.

[2] X. Yang, D. Vanderschueren, J. Dilewijns, C. Standaert and Y. Houbaert: *ISIJ Int.*, **36**(1996), pp. 1286-1294.

Chapter 4. Influence of inclusions in Fe-Al-Ti-O-N alloy on the microstructure by heating at 1473 K

4.1 Introduction

In order to utilize inclusions, not only investigation of inclusions evolution in solid alloy but also clarification of the influence of inclusions on grain refining is quite important. The widely well-known advantages of inclusions to obtain fine grain are two points, i.e. prevention of austenite grain growth by pinning effect and assistance of finer ferrite microstructure formation, especially those of TiN based inclusions as introduced in Sec. 1.2.3. In this chapter, the effects of not only TiN but also oxide type of inclusions on the microstructure have been studied.

4.2 Analysis method

The embedded as cast and heated samples were polished by SiC papers and diamond suspensions up to 0.25 μm using polishing machine (Struers, TegraPol-11) which is the same as the preparing method for SEM sample as explained in Sec. 2.2.2.2, and etched by etching solution (Methanol+ 5%HNO_3) for several seconds depending on etching speed. Etching solution was washed off by using methanol. The obtained sample was shown in **Fig. 4-1**.

Microstructure of all samples was observed by a digital microscope (KEYENCE, VHX-1000) on which two types of lenses were installed (VH-Z500WSPA, Magnification: 500 – 5000 times, VH-Z20WS, Magnification: 20 – 200 times).

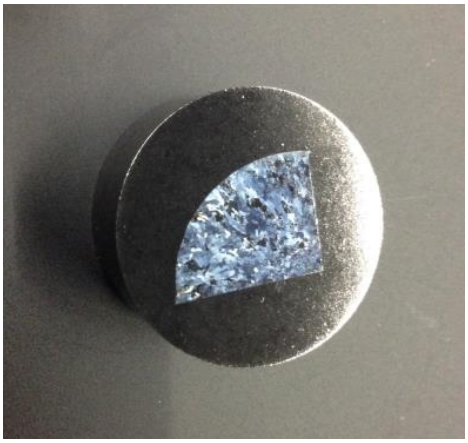

Figure 4-1. Picture of the etched sample D.

4.2.1 ASTM measurement

ASTM grain size number was calculated by using ASTM comparative chart method. The calculation method of ASTM grain size number has been reported by Brad Peirson. [1)] The ASTM grain size number can be calculated by using following equation.

$$N= 2^{n-1} \quad (4\text{-}1)$$

where N is the number of grains observed in an area of 1 in^2 (6.45 cm^2) on a photomicrograph taken at a magnification of 100 times, and n is the ASTM grain size number. The taken photomicrograph at a 100 times magnification was shown in **Fig. 4-2**. The area in each red square in the photomicrograph was 1 in^2. The number of grain in each square was measured. In the case of grain involved in several squares, it was regarded as 1/2 grain in each square. ASTM grain size number was determined by using average grain number of approximately 96 squares in each sample. From the calculated ASTM grain size number, average grain area and average grain diameter determined as shown in **Table 4-1**.[2)]

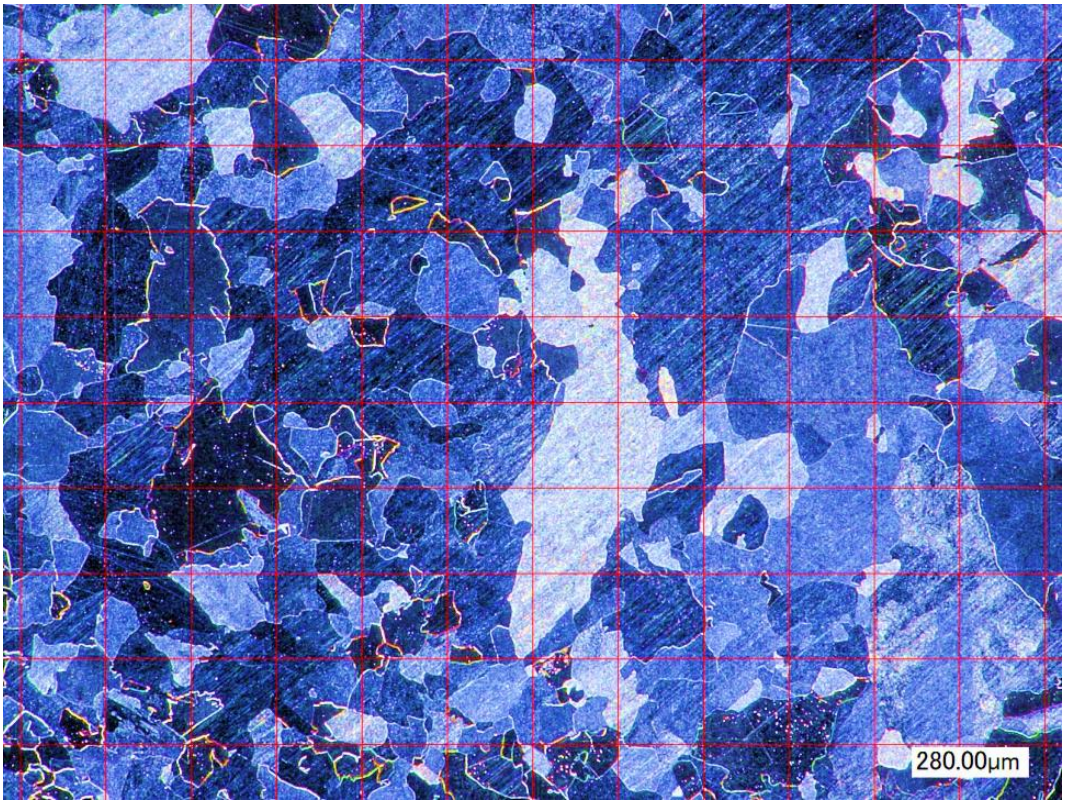

Figure 4-2. Photomicrograph of the etched sample D.

Table 4-1. Grain size relationships computed for uniform, randomly oriented, equiaxed grains.[2)]

Grain Size No.	$\bar{N}_A$ Grains/Unit Area		$\bar{A}$ Average Grain Area		$\bar{d}$ Average Diameter		$\bar{\ell}$ Mean Intercept		$\bar{N}_L$
G	No./in.^{2} at 100X	No./mm^2 at 1X	mm^2	µm^2	mm	µm	mm	µm	No./mm
00	0.25	3.88	0.2581	258064	0.5080	508.0	0.4525	452.5	2.21
0	0.50	7.75	0.1290	129032	0.3592	359.2	0.3200	320.0	3.12
0.5	0.71	10.96	0.0912	91239	0.3021	302.1	0.2691	269.1	3.72
1.0	1.00	15.50	0.0645	64516	0.2540	254.0	0.2263	226.3	4.42
1.5	1.41	21.92	0.0456	45620	0.2136	213.6	0.1903	190.3	5.26
2.0	2.00	31.00	0.0323	32258	0.1796	179.6	0.1600	160.0	6.25
2.5	2.83	43.84	0.0228	22810	0.1510	151.0	0.1345	134.5	7.43
3.0	4.00	62.00	0.0161	16129	0.1270	127.0	0.1131	113.1	8.84
3.5	5.66	87.68	0.0114	11405	0.1068	106.8	0.0951	95.1	10.51
4.0	8.00	124.00	0.00806	8065	0.0898	89.8	0.0800	80.0	12.50
4.5	11.31	175.36	0.00570	5703	0.0755	75.5	0.0673	67.3	14.87
5.0	16.00	248.00	0.00403	4032	0.0635	63.5	0.0566	56.6	17.68
5.5	22.63	350.73	0.00285	2851	0.0534	53.4	0.0476	47.6	21.02
6.0	32.00	496.00	0.00202	2016	0.0449	44.9	0.0400	40.0	25.00
6.5	45.25	701.45	0.00143	1426	0.0378	37.8	0.0336	33.6	29.73
7.0	64.00	992.00	0.00101	1008	0.0318	31.8	0.0283	28.3	35.36
7.5	90.51	1402.9	0.00071	713	0.0267	26.7	0.0238	23.8	42.04
8.0	128.00	1984.0	0.00050	504	0.0225	22.5	0.0200	20.0	50.00
8.5	181.02	2805.8	0.00036	356	0.0189	18.9	0.0168	16.8	59.46
9.0	256.00	3968.0	0.00025	252	0.0159	15.9	0.0141	14.1	70.71
9.5	362.04	5611.6	0.00018	178	0.0133	13.3	0.0119	11.9	84.09
10.0	512.00	7936.0	0.00013	126	0.0112	11.2	0.0100	10.0	100.0
10.5	724.08	11223.2	0.000089	89.1	0.0094	9.4	0.0084	8.4	118.9
11.0	1024.00	15872.0	0.000063	63.0	0.0079	7.9	0.0071	7.1	141.4
11.5	1448.15	22446.4	0.000045	44.6	0.0067	6.7	0.0060	5.9	168.2
12.0	2048.00	31744.1	0.000032	31.5	0.0056	5.6	0.0050	5.0	200.0
12.5	2896.31	44892.9	0.000022	22.3	0.0047	4.7	0.0042	4.2	237.8
13.0	4096.00	63488.1	0.000016	15.8	0.0040	4.0	0.0035	3.5	282.8
13.5	5792.62	89785.8	0.000011	11.1	0.0033	3.3	0.0030	3.0	336.4
14.0	8192.00	126976.3	0.000008	7.9	0.0028	2.8	0.0025	2.5	400.0

4.3 Results and discussion

4.3.1 Grain size in inner layer of as cast alloy

The calculated ASTM grain size number in the inner layer of all as cast samples was shown in **Table 4-2**. ASTM grain size number was in the range of from 1.9 to 2.5. In the case of sample B, ASTM grain size number was the smallest. On the other hand, the number was largest in the sample F.

Table 4-2. ASTM grain size number in inner layer of all samples.

	Average number of grains in an area of 1 in^2	ASTM grain size number
A	2.5	2.3
B	1.8	1.9
C	2.3	2.2
D	2.7	2.4
E	2.2	2.2
F	2.7	2.5

The number density of inclusions in the inner layer measured by using FE-SEM images was shown in **Table 4-3**. In each sample, areas from 25118 to 366435 μm^2 were observed for determination of the number density of inclusions such as TiN and/or TiS inclusions and Oxide+TiN and/or TiS inclusions.

The relationship between ASTM number and number density of inclusions in all as cast samples was shown in **Fig 4-3**. ASTM grain size number increased with increasing number of inclusions per unit area (10000 μm^2). This phenomenon has been reported in other investigators as shown in **Fig. 1-15** in Sec. 1.2.3. They used the mean distance between TiN particles instead of number density of inclusions.

Table 4-3. Number density of inclusions in the inner layer of all samples.

	Number of inclusions per 10000μm^2
A	5.02
B	1.9
C	4.7
D	15.3
E	4.1
F	6.80

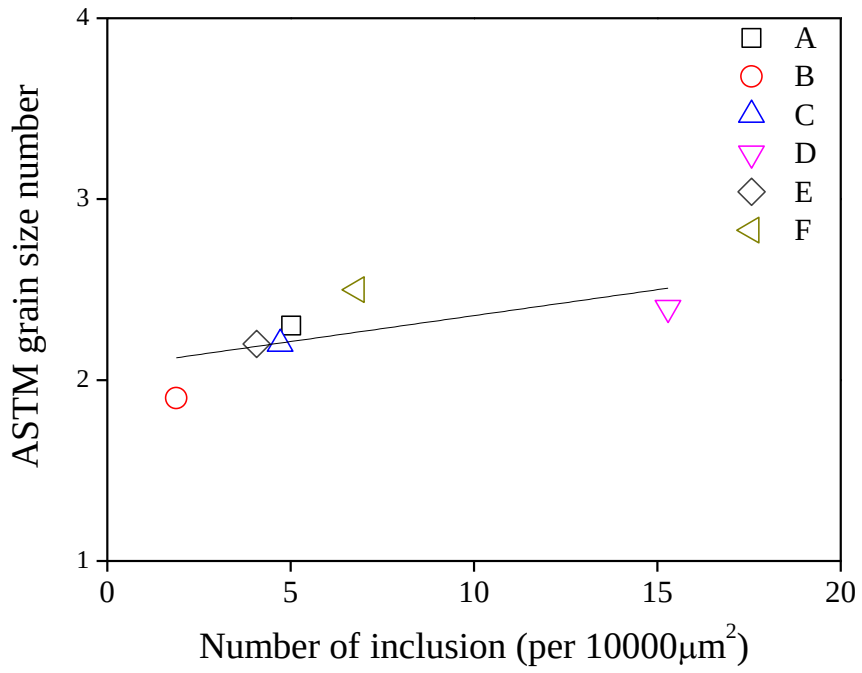

Figure 4-3. Relationship between ASTM grain size number and number density of all inclusions in the inner layer of all samples.

In all samples, TiS based inclusions such as TiS, TiN+TiS and oxide+TiS were observed. In order to clarify the effect of TiS on the grain refining, the relationship between number of TiS based inclusions and ASTM grain size number was shown in **Fig. 4-4**. The correlation between number of TiS based inclusions and ASTM grain size number was not observed. It even looks ASTM grain size number decreased with increasing the number of TiS inclusion. This result indicates that TiS based inclusions do not have any influence for obtaining fine grain.

Oxide+TiN and/or TiS inclusions were observed with the fraction from 7 to 68%. ASTM grain size number decreased with increasing number of oxide based inclusions as shown in **Fig. 4-5**. Since oxide inclusions were nearly completely covered by TiN or TiS, this tendency would be affected by TiS and TiN.

Figure 4-6 shows the relationship between ASTM grain size number and number of TiN based inclusions in the inner layer of all samples. ASTM grain size number increased by increasing of number of TiN based inclusion. From these results, it is concluded that number of TiN based inclusions becomes a decisive factor for grain refining.

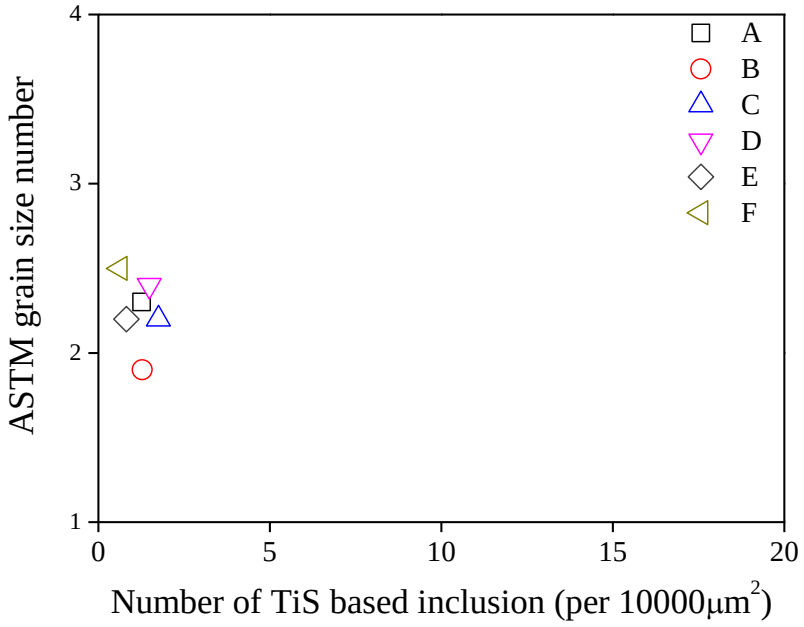

Figure 4-4. Relationship between ASTM grain size number and number density of TiS based inclusion in the inner layer of all samples.

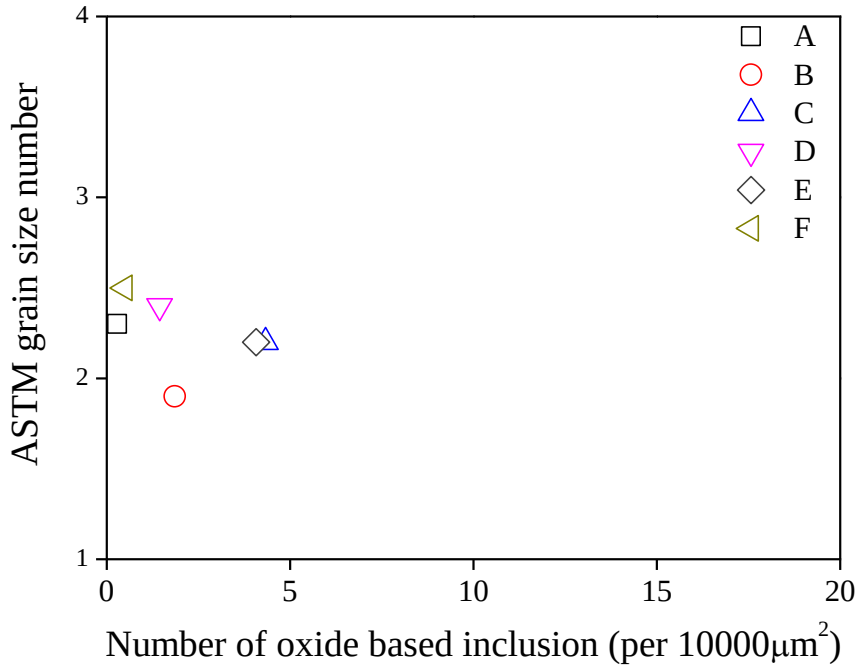

Figure 4-5. Relationship between ASTM grain size number and number density of oxide based inclusion in the inner layer of all samples.

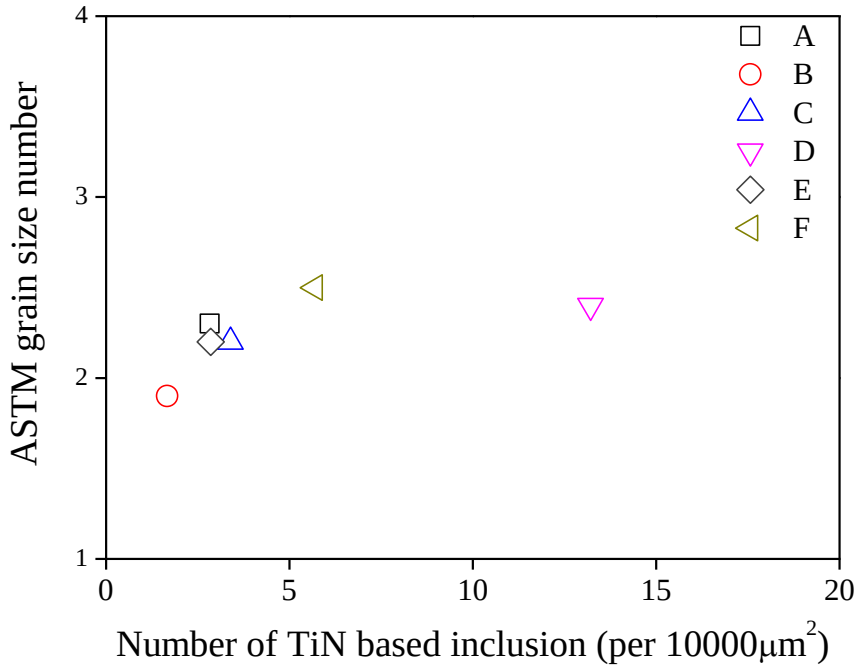

Figure 4-6. Relationship between ASTM grain size number and number density of TiN based inclusions in the inner layer of all samples.

4.3.2 Change of grain size in inner layer by heating

The photomicrographs in as cast and heated samples A, B, C, D, E and F were shown in **Figs. 4-7** and **4-8**.

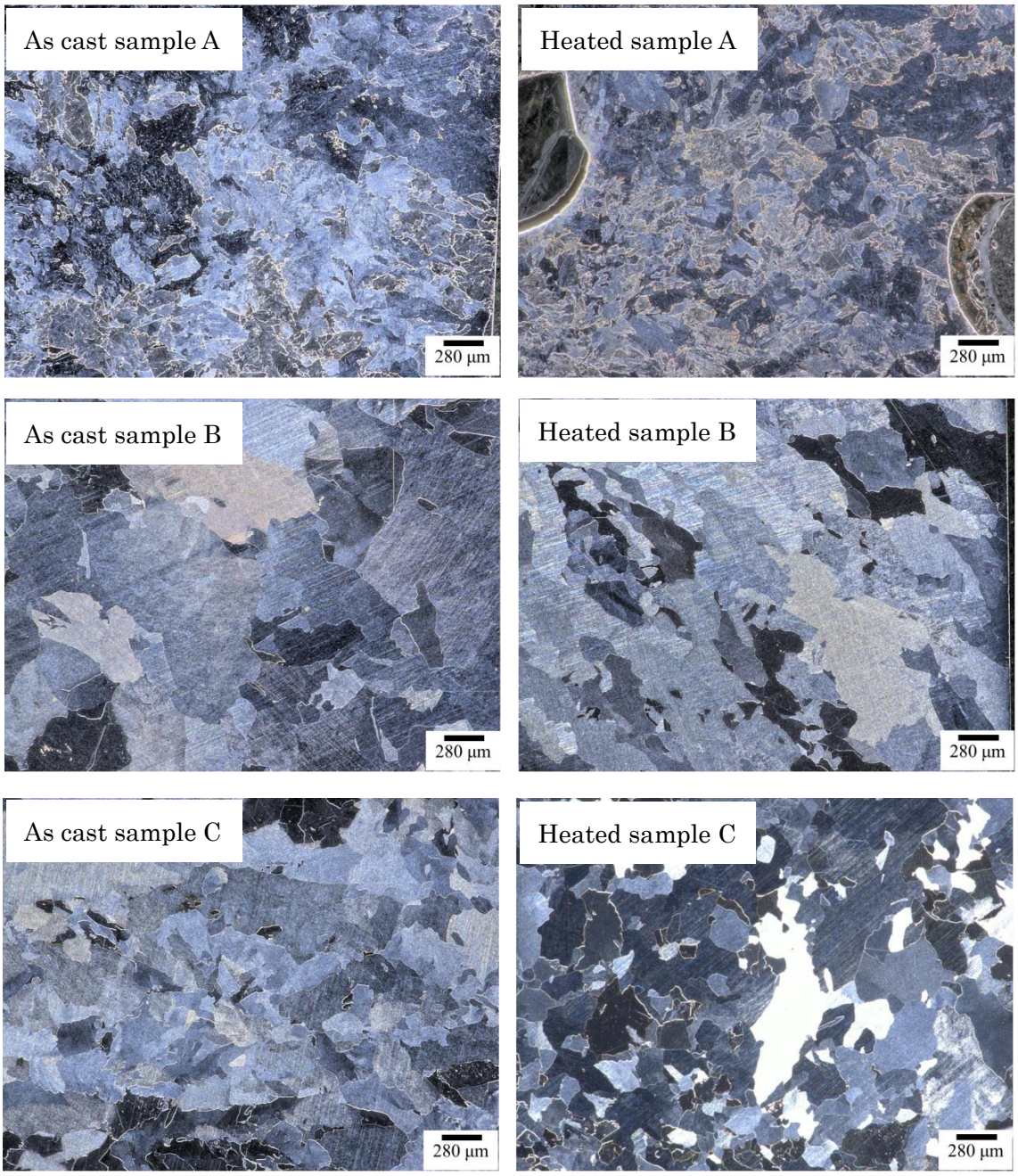

Figure 4-7. Photomicrographs in the inner layer of samples A, B and C by heating.

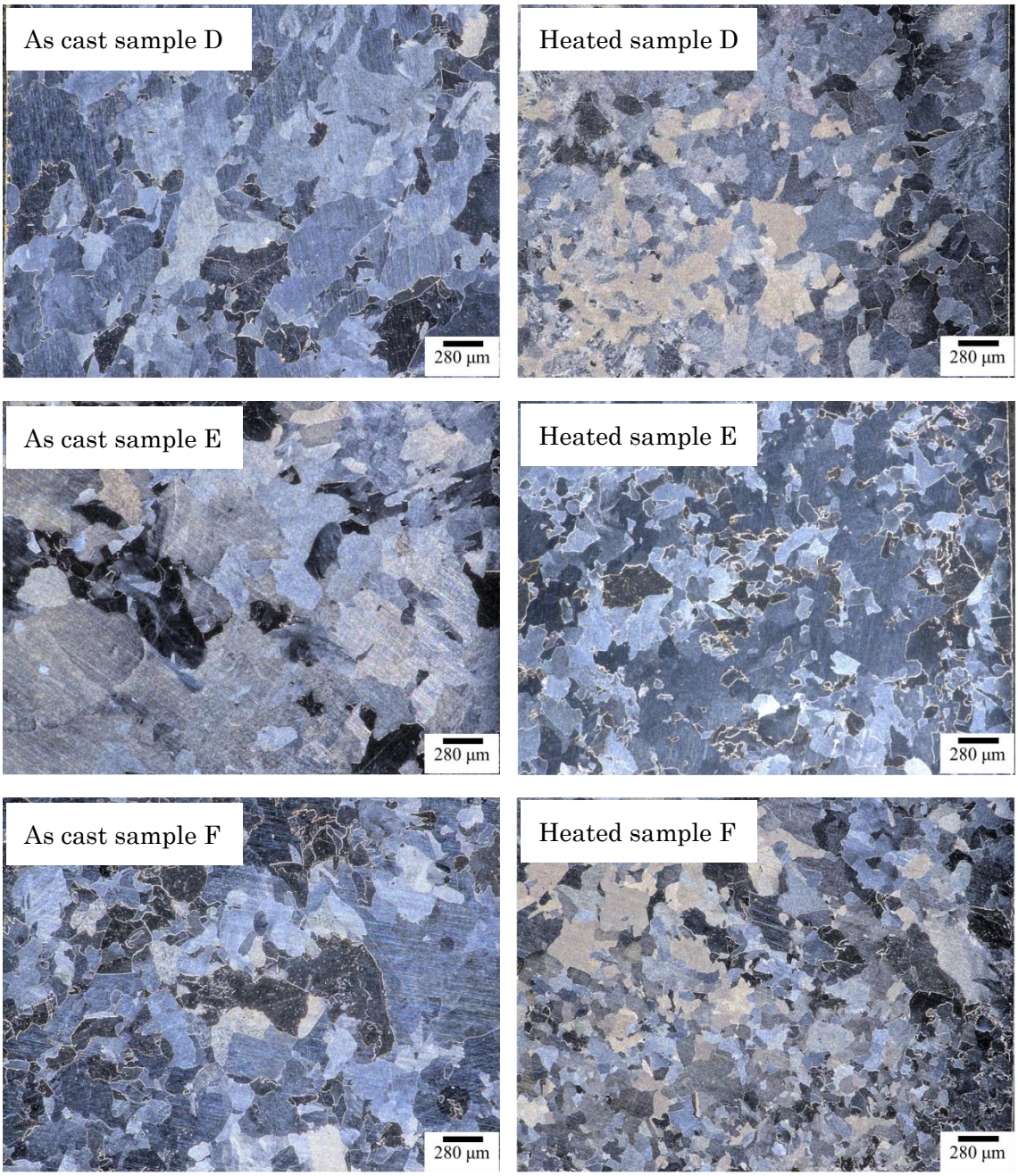

Figure 4-8. Photomicrographs in the inner layer of samples D, E and F by heating.

In the sample A, deformation microstructure was observed both in the as cast and heated samples. However, in all samples, grain refining was observed by heating for 3 hours. The calculated ASTM grain size number in the inner layer of all heated samples was shown in **Table 4-4**. The smallest number was observed in the sample B. On the other hand, the sample F has the largest number of

ASTM grain size. This tendency was also observed in as cast samples.

Table 4-4. ASTM grain size number in inner layer of heated samples.

	Average number of grains in an area of 1 in^2	ASTM grain size number
A	2.6	2.4
B	2.1	2.1
C	3.9	3.0
D	3.8	2.9
E	4.3	3.1
F	5.3	3.4

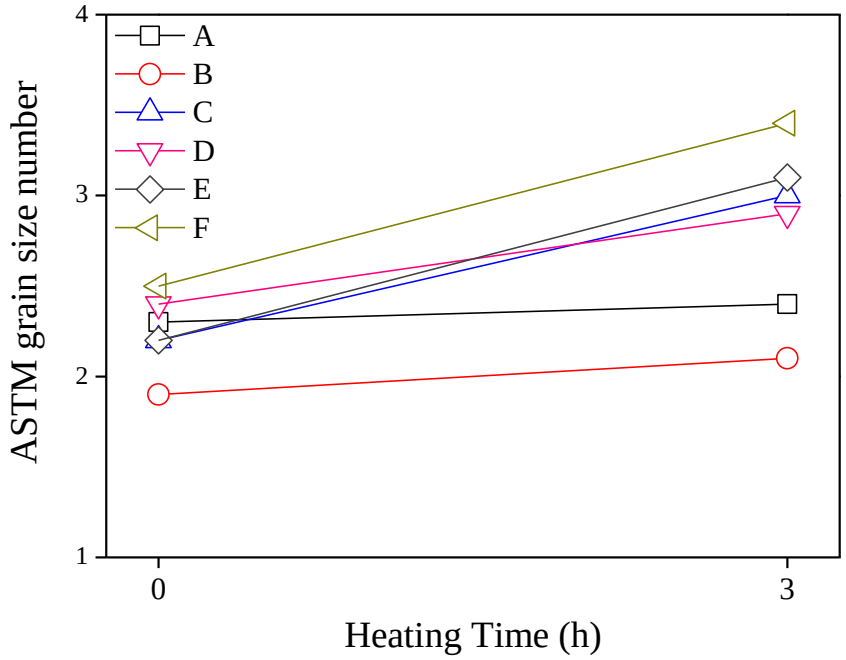

Figure 4-9. Change of ASTM grain size number in the inner layer of all samples by heating.

The change of ASTM grain size number with heating was shown in **Fig. 4-9**. The ASTM grain size numbers in all samples increased by 0.1 to 0.9 after heating. In other words, grain size decreased. In the samples E and F, the largest number increase was observed as 0.9.

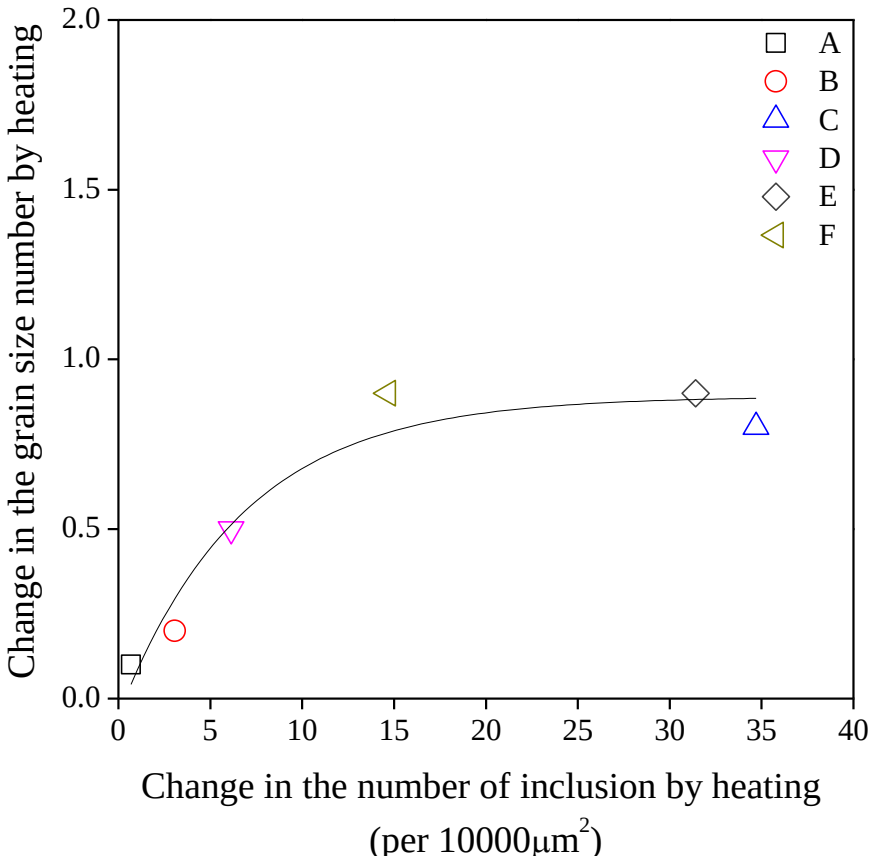

Figure 4-10. Relationship between changes of ASTM number and inclusion number in all samples by heating.

Figure 4-10 shows the relationship between changes of ASTM grain size number and inclusion number by heating. In the case of samples A, B, D and F, the change in the grain size number increased linearly by increasing the change in the number of inclusion. However, even though the change in the number of inclusions in the samples C and E further increased by 31 and 35, respectively, the change in the grain size number just increased by 0.8 and 0.9, which is in the same range as sample F. It would be explained by TiS formation by heating as follows.

Figure 4-11 shows the change of grain size number with regard to variation of the number of TiN based inclusions in a unit area. Change in the grain size number increased linearly with increasing the change in the number of TiN based inclusion in all samples.

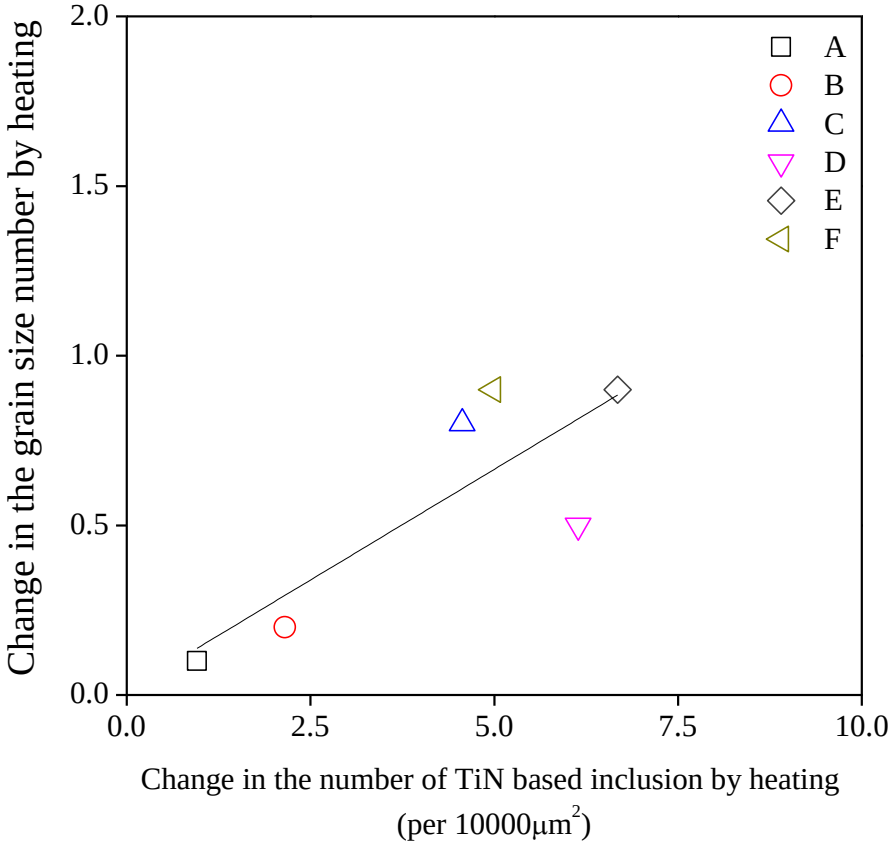

Figure 4-11. Relationship between changes of ASTM number and TiN based inclusion's number in all samples by heating.

Table 4-5 shows the change in the number of TiS particle and TiN based inclusion in a unit area (10000μm^2) of each sample. Number of TiS particles largely increased in the samples C and E by 7 and 14. TiS particles just increased total number of inclusions in samples C and E. From these results, it was indicated that TiN based inclusions significantly affected the increase of grain size number while the number of TiS inclusions just increased total number of inclusion. Therefore, increase of number of inclusion did not affect the increase of grain size number in the samples C and E.

Table 4-5. Change in the number of TiS particles in all samples by heating.

	Change in the number of TiS particle (per 10000μm^2)
A	-3
B	3
C	7
D	0
E	14
F	1

4.3.3 Pinning effect of oxide based inclusions in the outer layer by heating

In order to estimate the influence of oxide based inclusions on the grain refining, observation of outer layer is quite important, since oxide based inclusions were mainly observed in the outer layer of all samples.

Microstructure and inclusions in the outer layer were observed in the samples A, B and D since observation of grain boundary was impossible by using a microscope due to deformation microstructure in the outer layer of samples C, E and F. However, observed inclusions in the outer layer of samples C, E and F were almost Al_2O_3 and Al_2O_3+TiN inclusions which are the same as the sample D. Therefore, effect of Al_2O_3 and Al_2O_3+TiN inclusions on the microstructure could be inferred by the observation of sample D.

Morphology of microstructure such as grain size in the outer layer was similar to that in the inner layer. In addition, thickness of outer layer was thin and variable. Therefore, influence of inclusions on the microstructure could not be estimated by the change of grain size.

In present study, pinning effect of oxide based inclusions was estimated by measurement of the number of inclusions existing on the grain boundary. **Figure 4-12** shows the photomicrographs of the outer layer of the samples. The marked red circles mean the inclusions on the grain boundary.

Inclusions from 175 to 446 were observed in each sample as shown in **Table 4-6**. **Figure 4-13** shows the change of number of inclusions on the grain boundary by heating. In the case of samples A and B, number of inclusions on the grain boundary decreased by heating. In other words, oxide based inclusions in the outer layer of samples A and B have no pinning effect. In the case of sample D, number of inclusions in the grain boundary increased by heating. It seems that the weak pinning effect was exerted by heating.

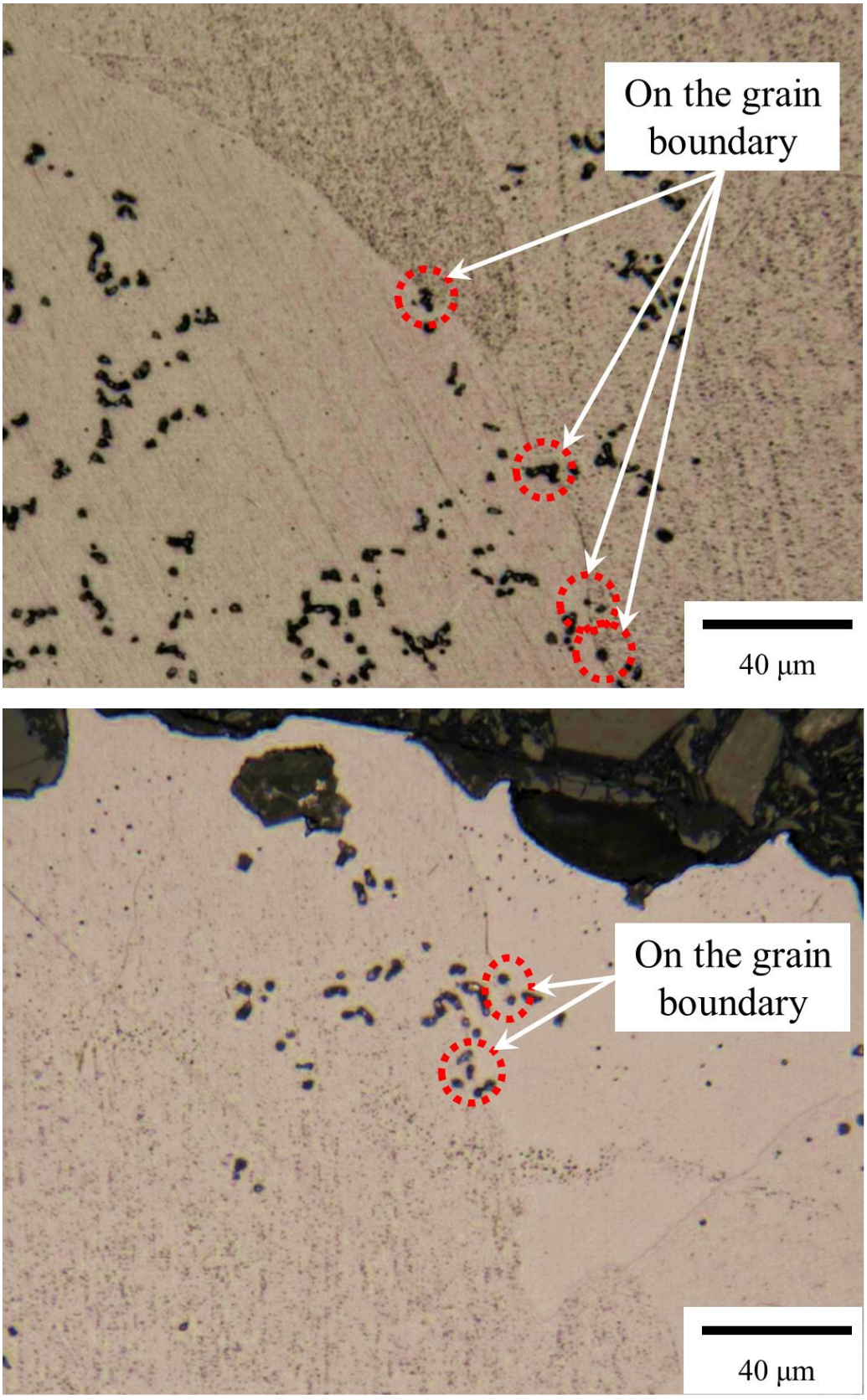

Figure 4-12. Photomicrographs of inclusions on the grain boundary in the outer layer.

Table 4-6. Change of number of inclusions on the grain boundary by heating.

		Total number of inclusion	Number of inclusion on the grain boundary	Fraction of number of inclusion on the grain boundary (%)
A	B.H.	181	26	14
	A.H.	183	10	5
B	B.H.	175	23	13
	A.H.	175	19	11
D	B.H.	179	14	8
	A.H.	446	53	12

B.H.: Before Heating, A.H.: After Heating

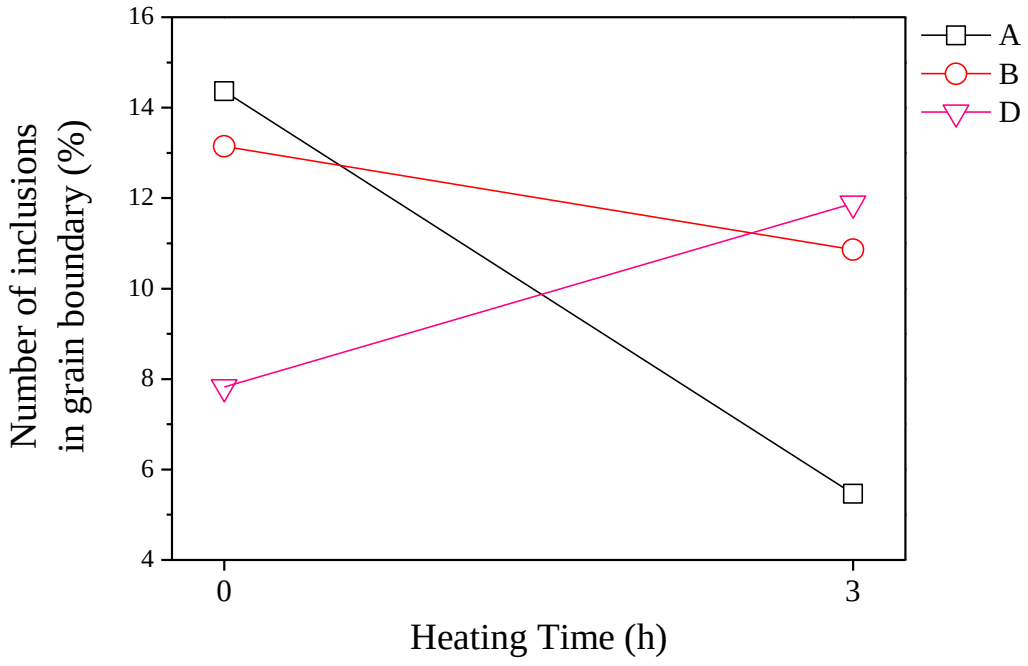

Figure 4-13. Change of number of inclusions in the grain boundary in samples A, B and D by heating.

4.4 Summary

In this chapter, effect of each type of inclusions on the grain refining has been studied. The grain size in the inner layer of as cast samples decreased with increasing the number of TiN based inclusions. Among several inclusion types in the inner layer, TiN based inclusions certainly reduced the grain size during solidification. On the other hand, any positive effects by the increase of number of TiS based and oxide based inclusions in the inner layer were not observed.

By heating, grain size decreased in the inner layer of all samples. This phenomenon was also related to the number of TiN based inclusions.

In the outer layer of samples A and B, pinning effect by oxide based inclusions was not observed. However, pinning effect of inclusions in the sample D was partially observed.

References

[1] ASTM E112 – 10, (2010)

[2] B. Peirson: “Laboratory Module 9, EGR 250 - Materials Science and Engineering Section 1”, School of Engineering Grand Valley State University, July 2005, http://claymore.engineer.gvsu.edu/~peirsonb/250_files/lab9_astm.pdf.

Chapter 5. Discussion of grain refining and stable oxide inclusion at 1473 K

5.1 Parameters for grain refining

In the Chapter 4, it has been verified that the number density of TiN based inclusions is a significant parameter for obtaining fine grain. Ti and N contents in the alloy are valuable factors for increasing number density of TiN during solidification and heating.

Figure 5-1 shows the grain number with solubility product of TiN in the all as cast samples. Overall, ASTM grain size number increased by increasing the product of Ti and N contents.

The black allows mean the increase of Ti content between two samples with similar nitrogen content. ASTM grain size number increased with increasing Ti. It would be due to the increase of opportunity for formation of TiN with increasing contents of Ti during solidification.

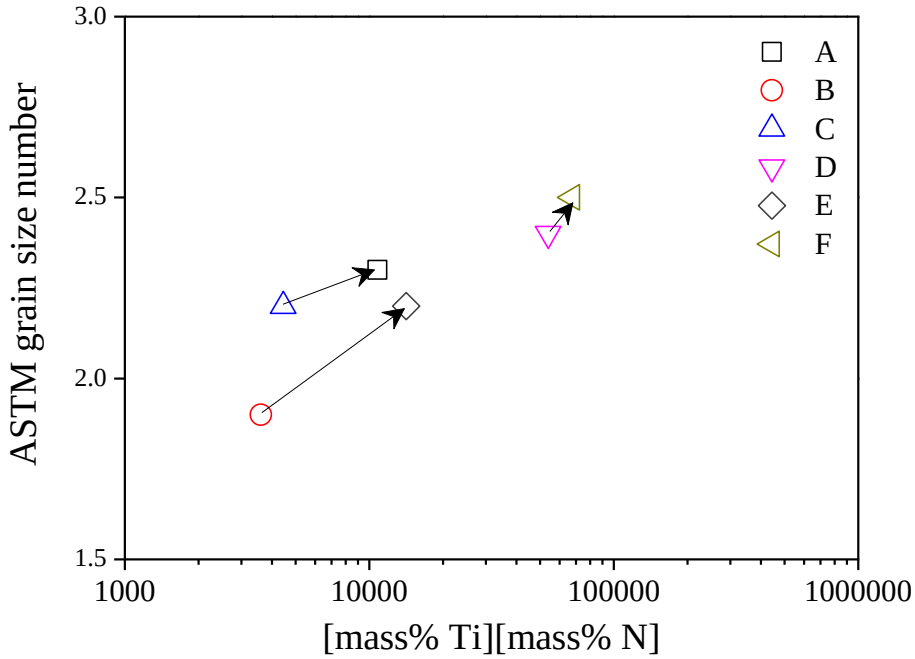

Figure 5-1. Relationship between ASTM grain size number and solubility product of TiN in the as cast of all samples.

Table 5-1. Number of TiN particles in the inner layer of all as cast samples.

	Fraction of TiN particles (%)
A	58
B	24
C	42
D	87
E	76
F	89

Table 5-1 shows the fraction of the number of TiN particles in the inner layer of all as cast samples. The fraction of the number of TiN particles increased by increasing Ti content with similar nitrogen content, i.e. from sample C to sample A: from 42 to 58 %, from sample B to sample E: from 24 to 76 % and from samples D to sample F: from 87 to 89 %. These results indicate that TiN particles were easily formed at the high titanium contents. As shown in **Figure 5-1** and **Table 5-1**, Ti and N contents would be main parameter for grain refining during solidification.

On the other hand, the change behavior of grain size with increasing Ti or N content in the heated samples was slightly different from that in the as cast samples. **Figure 5-2** shows the grain number with solubility product of TiN in the all heated samples. Overall, ASTM grain size number increased with increasing the product of Ti and N as well as the as-cast samples.

The black allows also mean the increase of Ti content between two samples with similar nitrogen content. The number of grain size fairly decreased with increasing the solubility product of TiN in samples C and A. From these results, it indicates that variation of grain size was influenced by not only Ti contents but also other parameters during heating.

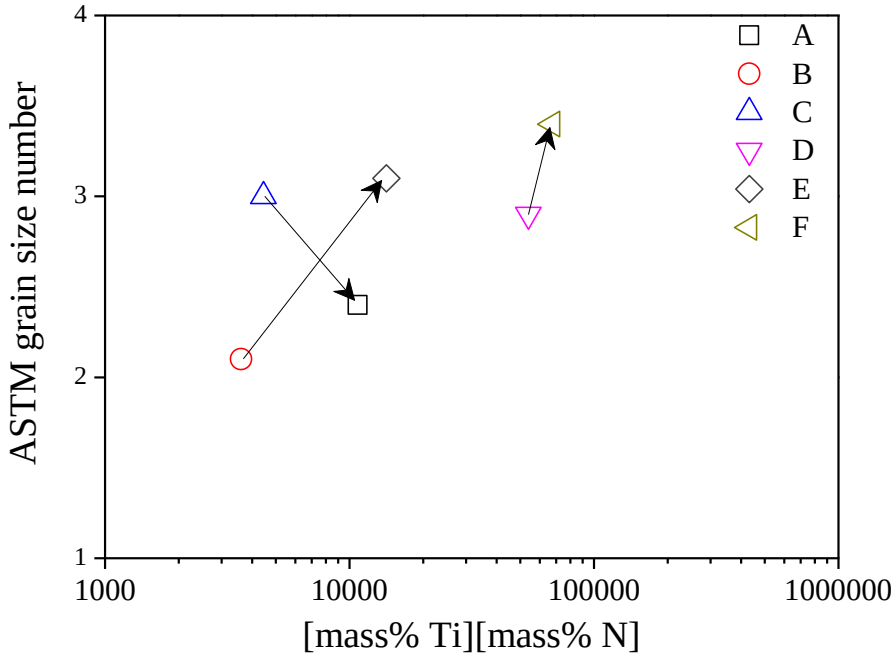

Figure 5-2. Relationship between ASTM grain size number and solubility product of TiN in the all heated samples.

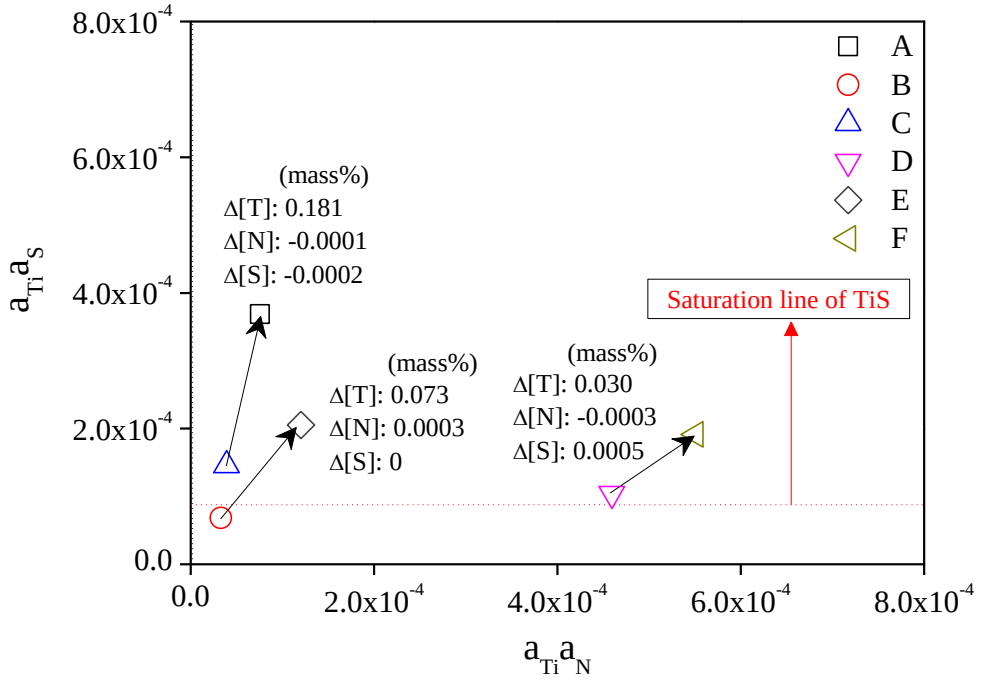

Figure 5-3. Relationship between activity products of TiN and TiS in the all heated samples.

Figure 5-3 shows the relationship between activity products of TiN and TiS. Red dot line means saturation of TiS at 1473 K. The increase of distance from saturation line means the increase of supersaturation ratio of TiS, in other words, formation of TiS easily occurs.

In the sample A, the product of Ti and S activities was the largest as 0.00037 among the six samples. Even though the product of Ti and N activities slightly increased with increasing Ti content from sample C to sample A, TiN nucleation would be obstructed by increasing of the degree of supersaturated TiS.

Black allows in **Fig. 5-3** could be represented as **Fig. 5-4**. **Figure 5-4** shows the relationship between the changes of the ASTM grain size number and the product Ti and S activities and Ti and N activities. The positive number in the change of the product of activities means the product increased by increasing Ti content with similar nitrogen content between two samples. In addition, the positive number in the change of ASTM grain size number means the grain size number increased by increasing Ti content with similar nitrogen content between two samples. In other words, grain size decreased with increasing Ti content. On the other hand, negative number in the change of ASTM grain size number means that grain size increased with increasing Ti content.

In the case of the change of product of Ti and N activities, change in the grain size number increased with increasing of the change of product of Ti and N activities. On the other hand, the change in the ASTM grain size number decreased with increasing the change in the product of activities of Ti and S.

In the case of the change from samples C to sample A, even though the product of activities of Ti and N increased, ASTM grain size number decreased since the product of activities of Ti and S increased more than that of Ti and N.

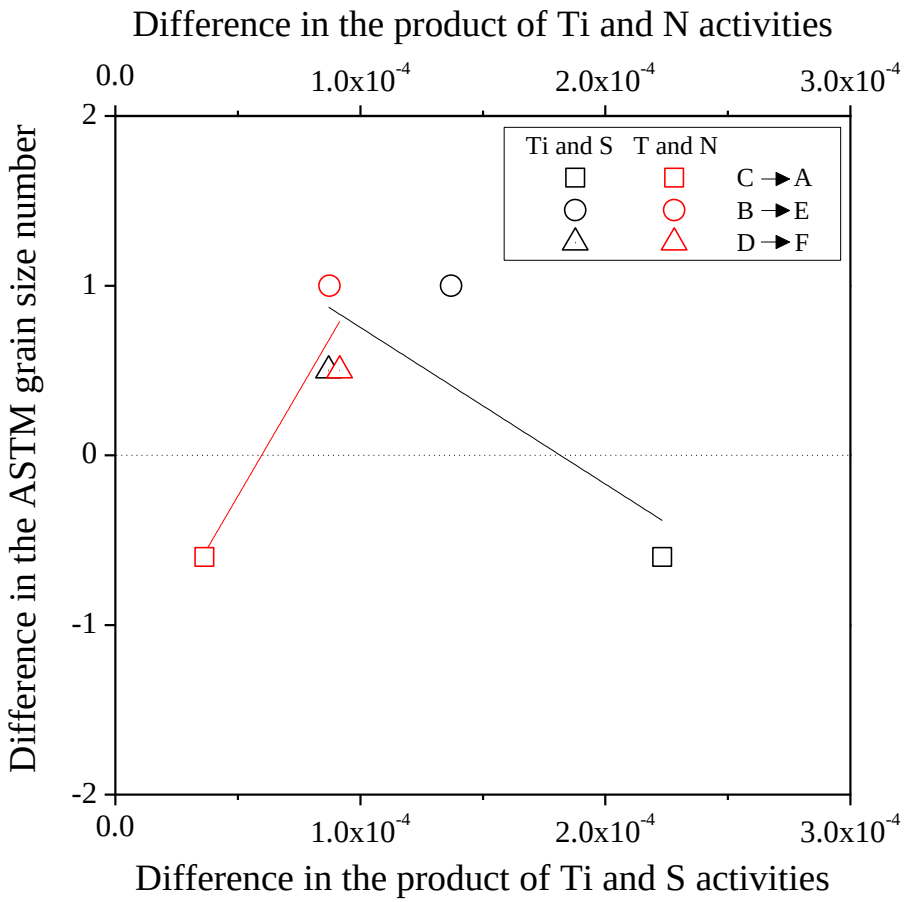

Figure 5-4. Relationship between the differences in the ASTM grain size number and the product of Ti and S activities or that of Ti and N activities by comparing in the heated samples with different Ti content and similar N content.

From all the results, it was concluded that the activities product of not only Ti and N but also Ti and S influenced on the grain size during heating.

The other considerable factor for grain refining was TiN particles size. **Figure 5-5** shows the relationship between the ASTM grain size number and the average size of TiN particles in all as cast and heated samples. The ASTM grain size number increased with increasing the average size of TiN particles. It seems that TiN size is also be one of the parameters for obtaining fine grain.

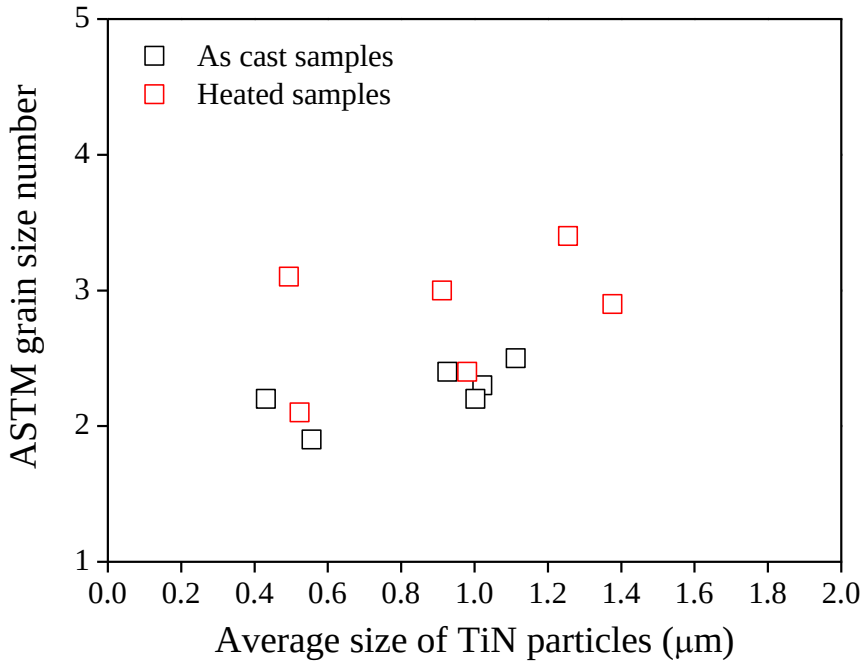

Figure 5-5. Relationship between the ASTM grain size number and the average size of TiN particles in as cast and heated samples.

As explained in Sec. 1.2.3, spinel inclusion ($MgAl_2O_4$) covered by TiN has an advantage for obtaining the fine grain during solidification. In the present study, not only Al_2O_3-MgO based but also Al_2O_3 based oxides fully covered by TiN or TiN+TiS phase were observed in the inner layer, i.e. polyhedral type of oxide+TiN or TiN+TiS inclusions. These types of inclusions were expected to have positive effect on the microstructure formation. Therefore, the influence of polyhedral type of oxide+TiN or TiN+TiS inclusions on the grain size was investigated.

Formation of TiS inclusions would be detrimental to grain refining as discussed previously. However, TiS phase partially formed on the polyhedral type of oxide+TiN phases. Therefore, effect of TiS phase would be insignificant.

Figure 5-6 shows the number of the polyhedral type of oxide+TiN or TiN+TiS inclusions with ASTM grain size number in the as cast samples. The influence of number of oxide+TiN or TiN+TiS

inclusions on the grain size was not observed in the as cast samples. **Figure 5-7** shows the change of ASTM grain size number with the change of the number of polyhedral type of oxide+TiN or TiN+TiS inclusion by heating. During heating, any change tendency of the grain size number was not observed by the increase or decrease of the number of polyhedral type of oxide+TiN or TiN+TiS inclusion. Even though the increase in number of TiN based inclusions leads to the grain refining as explained in Sec. 4.3.2, the effect of oxide+TiN or TiN+TiS inclusion on the reducing grain size was not observed in the **Figs. 5-6** and **5-7**. The reason would be the small number density of polyhedral type of oxide+TiN or TiN+TiS inclusion, 0.2 to 2.5 per 10000 μm^2.

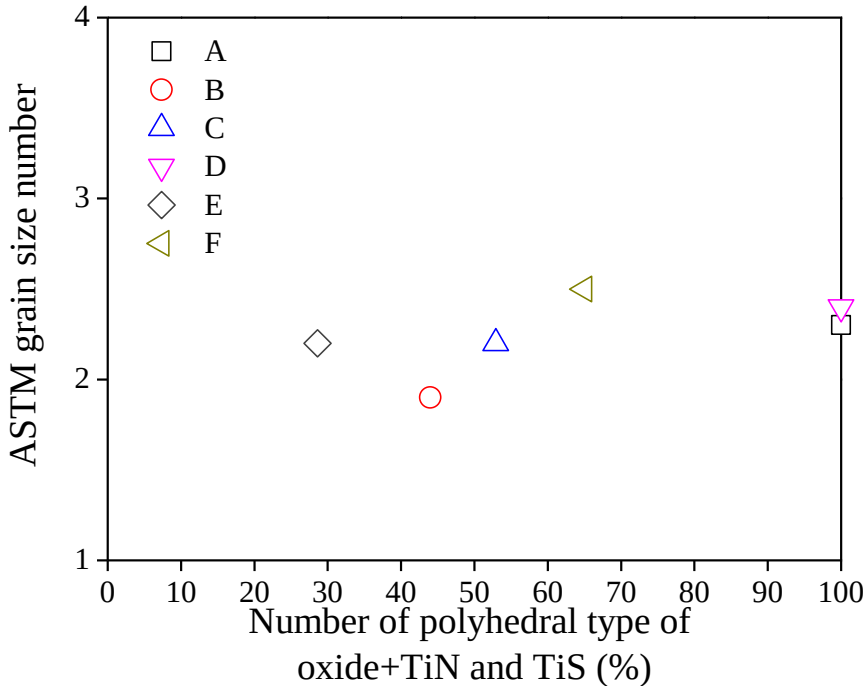

Figure 5-6. Relationship between the ASTM grain size number and the number of polyhedral type of oxide+TiN and TiS inclusion in as cast samples.

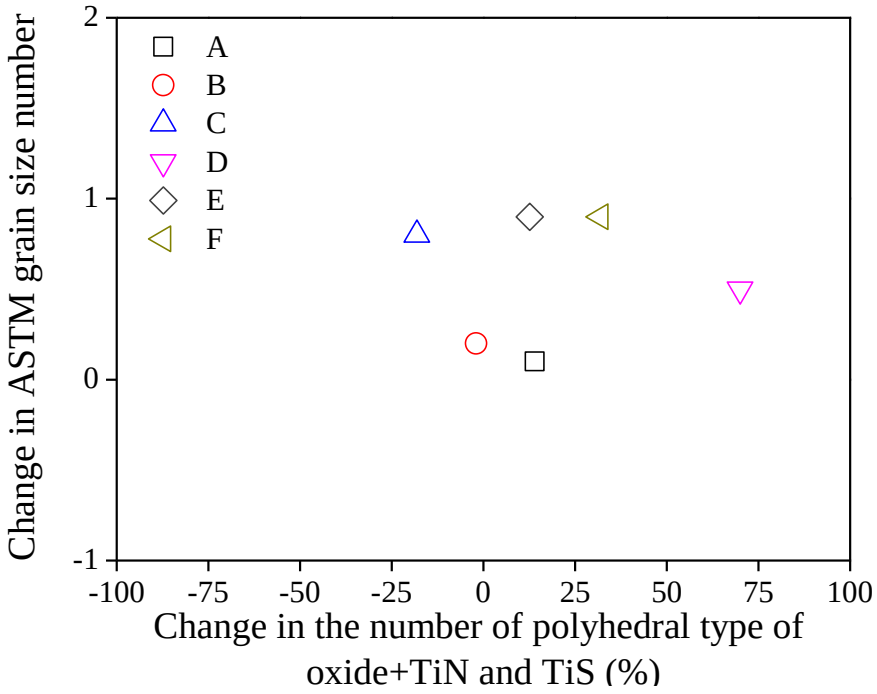

Figure 5-7. Relationship between changes in ASTM grain size number and the number of polyhedral type of oxide+TiN and TiS inclusion by heating.

5.2 Preference of TiN and TiS formation

TiN based inclusions including TiN particle are useful for grain refining. On the other hand, TiS based inclusions does not have any positive effect of the microstructure formation. Therefore, promotion of formation of TiN rather than TiS is valuable for grain refining.

In the all samples, TiN and TiS phases were usually formed during heating. Nitrogen and sulfur contents in the alloy would affect the formation of TiN and TiS. The total nitrogen and sulfur contents were shown in **Fig. 5-8**. The sulfur content was much larger than nitrogen content in the samples A, B, C and E. On the other hand, nitrogen content in the samples D and F was around 3 and 5 times larger than sulfur content in each sample.

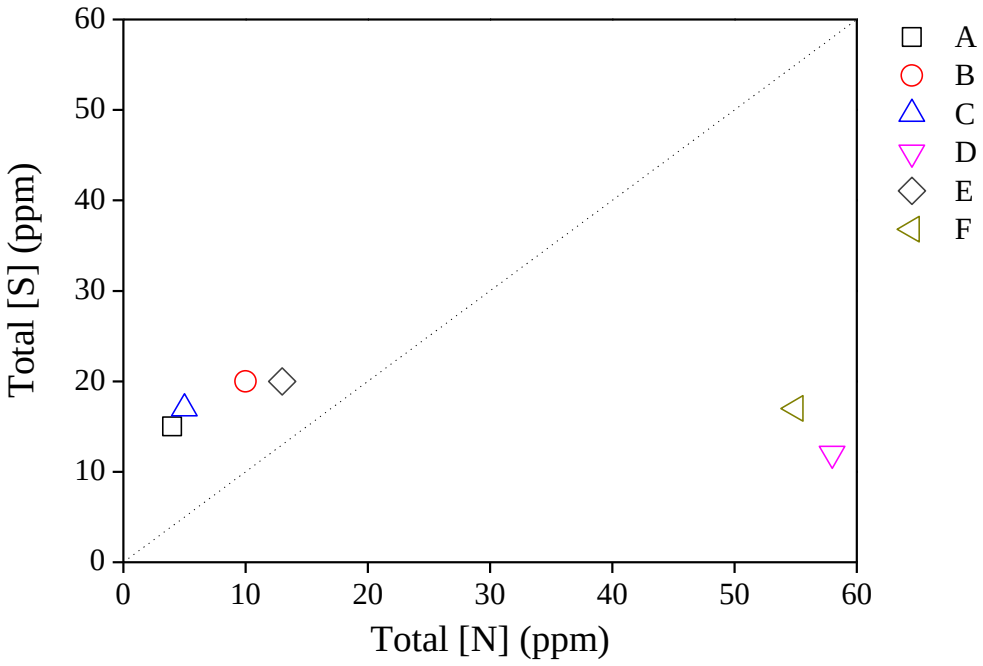

Figure 5-8. Total sulfur and nitrogen contents in all samples.

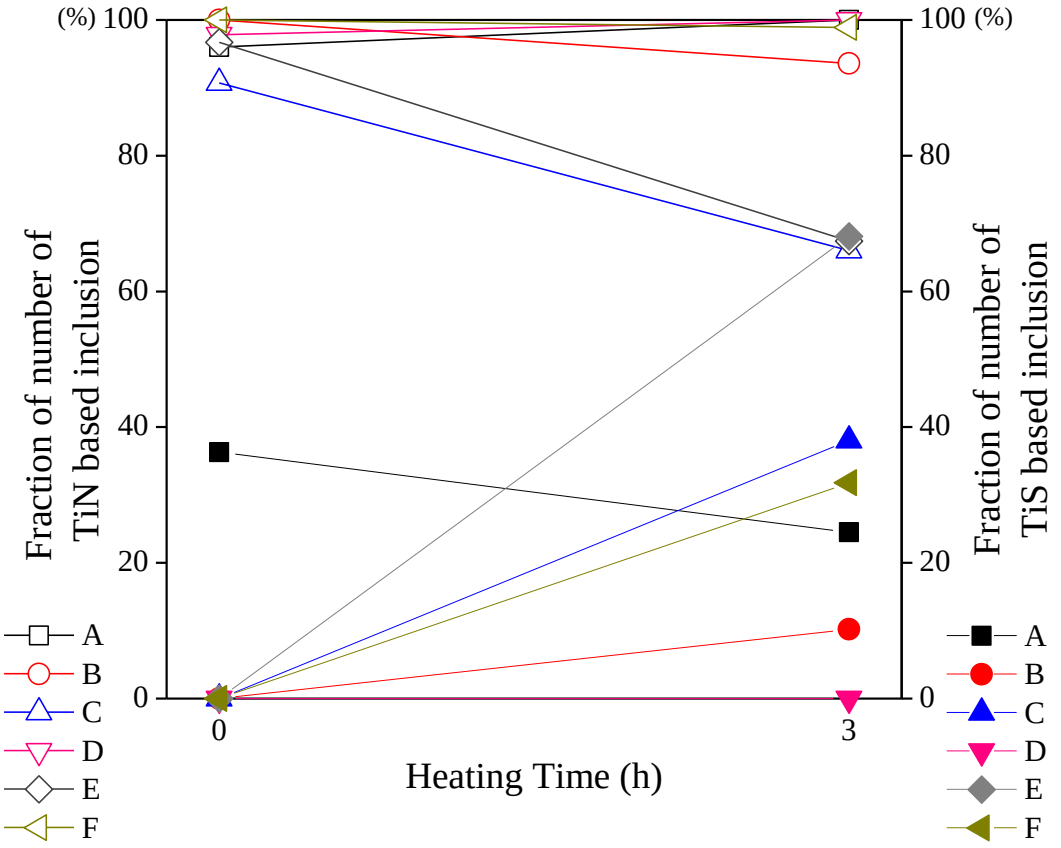

Figure 5-9. Change of the fraction of the number of TiN and TiS based inclusions by heating.

Figure 5-9 shows the change of the fraction of the number of TiN and TiS based inclusions by heating. In the samples B, C and E, TiS based inclusions increased by heating. Even in the sample F which consisted of high nitrogen content, 4.8 times of sulfur content, number of TiS based inclusions increased by heating. In the case of sample A in which TiS based inclusions existed, the number of TiS based inclusion decreased. In the case of sample D, TiS based inclusions did not formed by heating.

Comparing sample C with D or sample E with F, the samples contained similar Al and Ti contents and the difference was nitrogen content. In the both groups, it was indicated that the increase in N content resulted in the inhibition of TiS formation.

Therefore, in the case of sulfur content less than 20 ppm in the Al-killed Ti alloyed steel, around

50 ppm of nitrogen content is necessary to form TiN phase preferentially than TiS phase during heating at 1473 K.

5.3 Stable oxide in Fe-Al-Ti-O-N alloy

Inclusions finally evolved into stable state. Understanding of stable inclusion is quite important to control inclusions. Stable inclusions changed by the change of metal composition and temperature. Stable oxides in Fe-Al-Ti-O alloy at 1873 K have been studied by several investigators. However, stable oxide in the simple Fe-Al-Ti-O(-N) system at 1473 K have not been studied by experimental method.

In the Chapter 3, stable oxide phase at 1473 K could be predicted by observation of the characteristic change of oxide based inclusions by heating. The estimated stable oxide phase in each sample was shown in **Table 5-2**. Stable oxide phase in the samples A and B was estimated to be TiO_x and Al_2O_3, respectively, by observation of the change behavior of inclusion type. The chemical composition change of Al and Ti rich phases in the transient Al_2O_3+TiO_x inclusions indicated stable oxide phase in the samples C and E as Al_2O_3 and TiO_x, respectively. Though exact evidence for determination of stable oxide phase was not observed from the change behavior of inclusions, stable oxide phase in the samples D and F was predicted as Al_2O_3 and TiO_x by comparing with samples C and E at similar metal composition such as Al and Ti contents.

These stable oxides at 1473 K in each sample corresponded with those at 1873 K as shown in **Fig. 2-4** in Sec. 2.3. From this result, it was considered that the stable oxide in the Fe-Al-Ti-O(-N) alloy at both of solid and liquid states was almost the same and the influence of the decrease in temperature on the oxide stability was limited.

Table 5-2. Estimated stable oxide in all samples at 1473 K.

	Estimated stable oxide
A	TiO_x
B	Al_2O_3
C	Al_2O_3
D	Al_2O_3
E	TiO_x
F	TiO_x

5.4 Summary

In this Chapter, the parameters for grain refining have been studied. In the as cast samples, i.e. during solidification, Ti and N contents significantly affected on the grain size. On the other hand, the change of grain size was correlated with the relationship between product of Ti and N activities and that of Ti and S activities during heating.

The suitable nitrogen content to give preference for the formation of TiN, which has beneficial influence on the grain refining, rather than that of TiS was determined.

Comparing between computed stable oxide at 1873 K and estimated stable oxide at 1473 K, it was clarified that influence of temperature on the oxide stability was limited.

Chapter 6. Conclusions

In steelmaking process, various non-metallic inclusions are formed. These inclusions have been perceived as harmful and removed by using slag. However, removal of micro size of all inclusions or inclusions formed in solid steel is impossible. Therefore, utilization of inclusions is required and researches on this topic have been studied. The main objective of current study is to investigate the positive influence of inclusions on the steel properties. For this aim, effects of formed and evolved inclusions in the six different compositions of fundamental Fe-Al-Ti-O-N alloy system on the grain refining have been studied.

In Chapter 1, formation and change behaviors of inclusion in not only liquid state but also solid state of various grades of steel have been introduced, especially, Fe-Al-Ti-O alloy system. Furthermore, oxide metallurgy which is to utilize positive effects of the formed inclusions at various processes has been introduced. Most researches have reported the effects of Ti based inclusions on the austenite grain size. However, all researches have investigated the influence of inclusions not in the fundamental system but in the complex compositions of steel. Therefore, the current research has been initiated to clarify the effect of generable all inclusions including Ti based inclusions in Fe-Al-Ti-O-N alloy on the basis of clarification of formation and evolution procedure of inclusions in not only liquid state at steelmaking temperature as 1873 K but also solid state at general heat treatment temperature as 1473 K.

In Chapter 2, characteristics of the various types of inclusions formed in Fe-Al-Ti-O-N alloy at 1873 K have been studied. In order to obtain various types of inclusions, production method of alloy has been changed. The definite formation processes of all inclusions not only oxide inclusions but also nitride and sulfide inclusions have been discussed based on calculation of thermodynamic data and measurement of inclusion characteristics such as size, morphology and composition. It has been found that all oxide inclusions except small Al_2O_3-TiO_x inclusions form at deoxidation step and TiN, TiS and small Al_2O_3-TiO_x inclusions precipitate by solidification. The increase of number and size of

TiN particles has occurred with increasing nitrogen content.

In Chapter 3, in order to clarify the formation and evolution behaviors of inclusions in solid Fe-Al-Ti-O-N alloy, heating experiments have been carried out. By comparing Fe content of inclusions near surface of specimen and total oxygen content between as cast and heated samples, no existence of oxidation during heating have been proved. Furthermore, in order to protect alloy from oxidation, ampoule has been applied for some samples.

Based on the results obtained in Chapter 2, formation and change behaviors of inclusions by heating at 1473 K have been clarified in Chapter 3. The effects of not only bulk alloy composition but also partial morphology change of primarily existing inclusions on the formation and evolution of inclusions have been observed. The close correlation between nitrogen content and precipitations of TiS and TiN has been indicated. The size of TiN phase on the oxide phase has increased by the increase of nitrogen content. Besides, from the type and compositional changes of oxide inclusions, stable oxides in each Fe-Al-Ti-O-N alloy at 1473 K have been estimated.

In Chapter 4, effects of inclusions on grain size have been estimated by measurement of ASTM grain size number. Positive influence of Ti based inclusion, i.e. TiN, on the reducing grain size has been identified, as introduced in Chapter 1. On the other hand, significant effect of TiS or oxide based inclusions on the grain refining has not been observed.

In Chapter 5, parameters which have a beneficially influence for grain refining have been discussed. It has been found that the size of grain formed during solidification considerably depends on Ti and N contents. On the other hand, the change of grain size is correlated to the variations of products of Ti and N activities and Ti and S activities during heating.

By summarizing the results shown in Chapter 4 and Chapter 5, it is concluded that the control of number density of TiN based inclusions, size of TiN particles and product of Ti and S activities is significant to accelerate grain refining during heating at 1473 K. Some proposals for Al killed Ti alloying steel are given as follows. The effect of TiS inclusions on the microstructure had not been studied before current research. In current research, grain refining by TiS inclusions has not been

observed. Therefore, process should be designed to avoid TiS formation by controlling ratio of nitrogen and sulfur contents to give preference to TiN formation.

Acknowledgment

Life in Japan through the past three years was a great challenge to me. At this moment, all the things that used to be strange became familiar, and I feel warm. This feeling should be coming from all the favors I received from people. I would like to express my thanks to all those people.

First of all, I would like to give my deepest thanks to my supervisor Professor Fumitaka Tsukihashi for his consistent guidance and care. His impressive teaching led me to achieve academic growth and enjoyable life through the past three years.

I would also like to express my great thanks to Associate Professor Hiroyuki Matsuura for his kindness. The instructions he gave, and his specific suggestions were always the most precious key point for my work.

My great appreciation is given to the thesis evaluation committee members Prof. K. Terashima (Graduate School of Frontier Sciences, The University of Tokyo), Prof. H. Yoshizawa (Graduate School of Frontier Sciences, The University of Tokyo) and Prof. K. Morita (Graduate School of Engineering, The University of Tokyo), for their constrictive suggestion and comments to improve my work.

I want to thank the present and former members in Tsukihashi・Matsuura group: Prof. Oleg Ostrovski, Prof. Volodymyr Shatokha, Prof. Xiaojun Hu, Ms. Yuko Shoji, Dr. Yanfeng Wang, Dr. Chenxi Ji, Dr. Guohua Zhang, Ms. Sokur Yuliia and other students who shared happy memories.

I would like to thank the Ministry of Education, Science, Sports and Culture, Government of Japan and 21st century COE program “Applied Physics on Strong Correlation” of the University of Tokyo, for providing financial supports during my stay in Japan.

Finally, I want to give sincere gratitude to all my beloved family. Without their support and encouragement, I couldn’t be able to walk straight towards my dream.